Development of Cost-Effective Nano-Bainitic Steels

Doctoral Thesis

(Dissertation)

to be awarded the degree

Doctor of Engineering (Dr.-Ing.)

submitted by

Mohamad Akram Awad Abdelaziz

from Cairo, Egypt

approved by the Faculty of Natural and Materials Science,

Clausthal University of Technology,

Date of oral examination,

19.10.2022

Dean:	Prof. Dr.-Ing. Joachim Deubener
Chairperson of the Board of Examiners:	Prof. Dr. Rene Wilhelm
Supervising tutor:	Prof. Dr.-Ing. Heinz Palkowski
Reviewer:	Prof. Dr. Ernst Kozeschnik
Reviewer:	Prof. Dr. Goran Kugler

Abstract

The aim of this work is the development of low-cost, fast transforming nano-bainitic steel alloys for the purposes of lightweighting and fuel efficiency in the transportation industry. Three alloying strategies were investigated under the scope of this work. A high C (0.54-0.8 wt.%), low Mn strategy (0.3 wt.% Mn), a high C (0.67-0.95 wt.%), high Al-strategy (3 and 5 wt.%), and a low carbon (0.23 and 0.3 wt.), high Al (0.7 to 3 wt.%) contents. All the alloying strategies dispensed with the expensive substitutional elements Co, Cr and Ni. Fast transformation times ranging from 650 s to 4600 s were obtained for all the investigated conditions. The highest mechanical strengths were obtained by the low Mn alloying strategy, with tensile strengths ranging from 1900 - 2140 MPa at elongation values of about 10 %. Increasing the Al content within the second strategy lowers the transformation times compared to the alloys of the first strategy with similar C contents. However, because of their high Al-content, alloys of the second strategy required more C additions to maintain sufficiently low martensite start temperatures (Ms). This increase in C led to an overall increase in the transformation times within this strategy. On the other hand, increasing Al to 3 wt.% led to a drop in the maximum tensile strength from 2140 to 2000 MPa, while the elongation values remained constant at about 10 %, similar to those of the low Mn strategy. Further increasing Al to 5 wt.% yielded brief incubation periods and shorter transformation times (1000 – 1800 s) despite the high C contents utilized (0.67 – 0.94 wt.%). However, this came at the cost of a deterioration of the strength-ductility balance, with strength values ranging from 1330 – 1845 MPa and ductility of about 5 %.

Increasing the Al content within the third strategy from 0.7 to 2.8 wt.% (~ 0.3 wt.% C and ~ 2.9 wt.% Mn) lowers the transformation time from 3000 to 2000 s, respectively, at a cost of a reduction in tensile strength and elongation from 1330 to 1270 MPa and from 13.5 to 7.7%, respectively. Introducing δ-ferrite to the

microstructure of the 3 wt.% Al alloy (~ 0.23 wt.% C and ~ 4.2 wt.% Mn) increased elongation% up to 16% and reduced the tensile strength to 1105 MPa. Continuously cooling of alloys of this group at a rate of 0.3 Ks-1 yielded almost fully martensitic structures, with bainite partly forming only in the alloys with higher Al. A cooling rate of 0.03 Ks-1 increased the tensile strength by about 100 MPa at similar elongation values, while lowering the cooling rate down to 0.003 Ks-1 yielded similar properties as isothermal treatment because most of the transformation is concluded near the starting temperature.

For both the low and high C groups, the impact properties increased with the increase of Al to 2 – 3 wt.% followed by a drop as the Al was increased further. Conversely, the presence of δ-ferrite severely deteriorated the impact properties of the microstructures generated. Impact testing of select alloys from (-160 to 50 °C) revealed that changing the Al content has no significant effect on the impact transition temperature. Generating deformation induced ferrite (DIF) in the microstructure of the low carbon group alloys prior to the bainitic transformation had inconclusive effects on the final properties, improving the uniform elongation in some cases while deteriorating it in others. Finally, select alloys were subjected to bake hardening investigations to help expand a newly developed module in MatCalc software into the field of fine bainitic steels. Strain ageing experiments reveal high bake hardening strengths ranging from 130 – 240 MPa after brief ageing times of less than 20 min. The developed model was able to successfully predict the bake hardening behaviour of the alloys investigated.

Kurzfassung

Ziel dieser Arbeit ist die Entwicklung kostengünstiger, schnell umwandelnder nano-bainitischer Stahllegierungen für die Zwecke des Leichtbaus und der Kraftstoffeffizienz in der Transportindustrie. Im Rahmen dieser Arbeit wurden drei Legierungsstrategien untersucht. Eine Strategie mit hohem C- (0,54-0,8 Gew.-%) und niedrigem Mn-Gehalt (0,3 Gew.-% Mn), eine Strategie mit hohem C- (0,67-0,95 Gew.-%) und hohem Al-Gehalt (3 und 5 Gew.-%) sowie eine Strategie mit niedrigem Kohlenstoff- (0,23 und 0,3 Gew.-%) und hohem Al-Gehalt (0,7 bis 3 Gew.-%). Bei allen Legierungsstrategien wurde auf die teuren Substitutionselemente Co, Cr und Ni verzichtet. Für alle untersuchten Bedingungen wurden schnelle Umwandlungszeiten zwischen 650 s und 4600 s erzielt. Die höchsten mechanischen Festigkeiten wurden mit der Legierungsstrategie mit niedrigem Mn-Gehalt erzielt, wobei die Zugfestigkeiten zwischen 1900 und 2140 MPa bei Dehnungswerten von etwa 10 % lagen. Die Erhöhung des Al-Gehalts bei der zweiten Strategie senkt die Umwandlungszeiten im Vergleich zu den Legierungen der ersten Strategie mit ähnlichen C-Gehalten. Aufgrund ihres hohen Al-Gehalts benötigten die Legierungen der zweiten Strategie jedoch mehr C-Zusätze, um ausreichend niedrige Martensit-Starttemperaturen (Ms) zu erhalten. Diese Erhöhung des C-Gehalts führte zu einer allgemeinen Verlängerung der Umwandlungszeiten bei dieser Strategie. Andererseits führte eine Erhöhung des Al-Gehalts auf 3 Gew.-% zu einem Rückgang der maximalen Zugfestigkeit von 2140 auf 2000 MPa, während die Dehnungswerte bei etwa 10 % konstant blieben, ähnlich wie bei der Strategie mit niedrigem Mn-Gehalt. Eine weitere Erhöhung des Al-Anteils auf 5 Gew.-% führte trotz der hohen C-Gehalte (0,67 - 0,94 Gew.-%) zu kurzen Inkubationszeiten und kürzeren Umwandlungszeiten (1000 - 1800 s). Dies ging jedoch auf Kosten einer Verschlechterung des Festigkeits-Duktilitäts-Gleichgewichts, mit Festigkeitswerten von 1330 - 1845 MPa und einer Duktilität von etwa 5 %.

Die Erhöhung des Al-Gehalts innerhalb der dritten Strategie von 0,7 auf 2,8 Gew.-% (~ 0,3 Gew.-% C und ~ 2,9 Gew.-% Mn) verkürzt die Umwandlungszeit von 3000 auf 2000 s, allerdings auf Kosten einer Verringerung der Zugfestigkeit und der Dehnung von 1330 auf 1270 MPa bzw. von 13,5 auf 7,7 %. Die Einführung von δ-Ferrit in das Gefüge der 3-Gew.-%-Al-Legierung (~ 0,23 Gew.-% C und ~ 4,2 Gew.-% Mn) erhöhte die Dehnung um bis zu 16 % und reduzierte die Zugfestigkeit auf 1105 MPa. Die kontinuierliche Abkühlung von Legierungen dieser Gruppe mit einer Rate von 0,3 Ks-1 führte zu fast vollständig martensitischen Strukturen, wobei sich nur in den Legierungen mit höherem Al-Anteil teilweise Bainit bildete. Eine Abkühlungsrate von 0,03 Ks-1 erhöhte die Zugfestigkeit um etwa 100 MPa bei ähnlichen Dehnungswerten, während eine Verringerung der Abkühlungsrate auf 0,003 Ks-1 ähnliche Eigenschaften wie eine isotherme Behandlung ergab, da der größte Teil der Umwandlung in der Nähe der Anfangstemperatur abgeschlossen ist.

Sowohl bei der Gruppe mit niedrigem als auch bei der Gruppe mit hohem C-Gehalt stiegen die Kerbschlagzähigkeitseigenschaften mit der Erhöhung des Al-Gehalts auf 2 bis 3 Gew.-% an, gefolgt von einem Rückgang bei weiterem Anstieg des Al-Gehalts. Umgekehrt verschlechterte das Vorhandensein von δ-Ferrit die Kerbschlagzähigkeit der erzeugten Gefüge erheblich. Kerbschlagbiegeversuche an ausgewählten Legierungen im Temperaturbereich von -160 bis 50 °C zeigten, dass eine Änderung des Al-Gehalts keine signifikante Auswirkung auf die Kerbschlagübergangstemperatur hat. Die Erzeugung von verformungsinduziertem Ferrit (DIF) im Gefüge der Legierungen mit niedrigem Kohlenstoffgehalt vor der bainitischen Umwandlung hatte keine schlüssigen Auswirkungen auf die endgültigen Eigenschaften, wobei sich die gleichmäßige Dehnung in einigen Fällen verbesserte, während sie sich in anderen Fällen verschlechterte. Schließlich wurden ausgewählte Legierungen einer Bake-Hardening-Untersuchung unterzogen, um ein neu entwickeltes Modul der MatCalc-Software auf den Bereich der feinbainitischen Stähle auszuweiten. Die Alterungsversuche zeigen hohe Bake Hardening

Festigkeiten von 130 - 240 MPa nach kurzen Alterungszeiten von weniger als 20 min. Das entwickelte Modell war in der Lage, das Bake-Hardening-Verhalten der untersuchten Legierungen erfolgreich vorherzusagen.

Table of contents

List of symbols and abbreviations

Advanced High Strength Steels	AHSS
Dual Phase	DP
Complex Phase	CP
TRansformation Induced Plasticity	TRIP
TWinning Induced Plasticity	TWIP
Quenching and Partitioning	Q&P
Bainitic Ferrite	α_b
Retained Austenite	γ_r
Elongation Percent	EL%
Nano-Bainite	nB
Austenite Carbon Content	Cγ
Atom-Probe Tomography	APT
X-Ray Diffraction	XRD
Martensite/Austenite Islands	M/A
Martensite Start Temperature	Ms
Bake Hardening	BH
Computer Coupling of Phase Diagrams and Thermochemistry	CALPHAD
Linear Variable Differential Transducer	LVDT
Light Optical Microscopy	LOM
Scanning Electron Microscopy	SEM
Deformation Induced Ferrite	DIF
Energy Dispersive X-Ray Analysis	EDX
Transmission Electron Microscopy	TEM
Rolling Direction	RD
Deformation Induced Ferrite Transformation	DIFT
Thermo-mechanical	TM
Room Temperature	R.T.
Bake hardening at 170 °C for 20 min	BH_{20}

1. Introduction

Fuel efficiency and a reduction of the carbon footprint are the main drivers for developments in all the sectors of the automotive industry. When considering automotive materials, the main goal for research effort is lightweighting via either density reduction or improvements in strength to enable downgauging. The resulting increase in utilization of lightweight materials (such as aluminium or magnesium alloys, or polymer matrix composites) in vehicles at the expense of the formerly used steels forced the steel industry to invest in the development of more competitive alternatives. Research into restoring steel as a viable option for lightweight, fuel-efficient vehicles birthed Advanced High Strength Steels (AHSS), which are a class of steels offering significantly higher mechanical properties than conventional carbon steels. The increase in strength at similar/higher elongation values enabled smaller gauge components to be made from those new alloys, resulting in appreciable weight reduction. The first generation of AHSS included Dual Phase (DP), Complex Phase (CP) and TRansformation Induced Plasticity (TRIP) steels with tensile strengths in excess of 600 MPa and good formability. The second generation of AHSS was introduced with the development of TWinning Induced Plasticity (TWIP) steels, which could attain tensile strengths of around 1 GPa at total elongations of 50 – 60 % [1–3].

Currently a different trend governs the latest third generation of AHSS, where the classification depends on an alloy's ability to obtain the same elongation properties of an existing AHSS grade while offering a higher tensile strength value. Main candidates for this generation are medium Mn steels, Quenching and Partitioning (Q&P) steels, and carbide free bainitic steels [1].

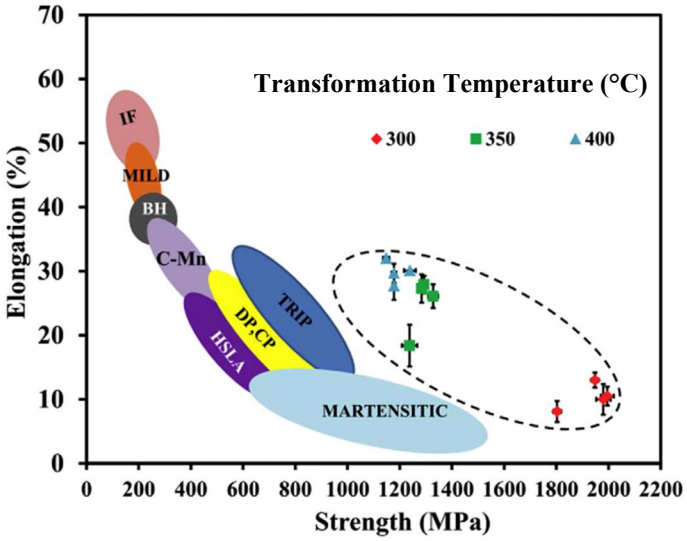

Figure 1-1: Elongation vs strength curves for various steels compared to nB. Reprinted by permission from: Elsevier, Materials & Design [4].

Carbide free bainitic steels have a microstructure of bainitic ferrite (α_b) and retained austenite (γ_r). The absence of cementite enables them to achieve extraordinarily high strengths at high elongation to rupture values (EL%), expanding the region on the strength vs elongation diagram as shown in **Figure 1-1**. The presence of carbides in conventional bainitic microstructures hinder their utilization, as cementite is a void nucleation phase that is detrimental to ductility [5]. **Figure 1-1** also includes the strength vs elongation results for bainitic alloys transformed at 300, 350 and 400 °C from a study by Varshney et al. achieving strengths of up to 2 GPa [4]. Moreover, other literature sources pin the possibly attainable strength to a value of up to 2.5 GPa [4–7]. One of the merits of carbide free bainitic steels is the ability to obtain nano-scaled microstructures by applying conventional heat treatment cycles. Nanocrystalline metals are commonly produced via severe plastic deformation, hindering their commercial utility, and making the production of large

nanocrystalline components a difficult task. On the other hand, nano-bainitic steels (nB) are produced via heat treatments that do not require rapid cooling, hence enabling the production of larger sized components than is possible with nano-crystalline metals or even with conventional martensitic steels [8,9].

While nB is a nano-structured sub class of carbide free bainite, both names are sometimes used interchangeably to refer to nB; other names found in literature for these steels are fine bainite and low temperature bainite. For the sake of simplicity, the term "nB" will be used in this document to refer to the intended microstructure, which consists of nano-sized α_b lamellae and γ_r of varying grain sizes and morphologies.

This work aims to develop new alloying strategies and apply a number of processing routes to produce nB with high strength while avoiding the common shortcomings of nB that have been hindering its commercial utilization. This document is organized into six chapters. Chapter 2 provides the theoretical background on the topics of bainite, carbide free and nano bainite, along with a review of the most important literature sources on the topic of nB. Chapter 3 details the objectives of the research presented in this thesis, outlining the workflow implemented to attain these objectives. Chapter 4 discusses the experimental work undertaken to achieve the aforementioned objectives. Chapter 5 covers the results obtained from the experiments performed and their analysis. Finally, Chapter 6 provides the conclusions attained from the current work while also providing suggestions for expanding the research into other routes that could be of interest.

2. Literature review

2.1. Bainite

Bainite is a cubic, body centred (BCC) ferrite phase that nucleates displacively at low temperatures where reconstructive transformation into α and pearlite is not thermodynamically feasible. Its structure could be described as ferritic subunits separated by residual phase regions, which could be γ_r, martensite, or cementite. These subunits are not completely separated by the residual phases and share a common crystallographic orientation and are separated by low misorientation grain boundaries forming aggregates. Bainitic aggregates are commonly referred to as sheaves. The 3-dimensional morphology of a bainitic sheaf, shown in **Figure 2-1**, resembles a wedge-shaped plate, with its thicker end originating at the γ grain boundary where the bainite nucleates. While the width of the sheaf decreases the further it grows from its nucleation site, the width and dimensions of the individual subunits remain the same regardless of their position along the length of the sheaf, suggesting that these subunits grow to a limiting size. The bainite subunits have their long dimension along the close packed direction of the BCC ferrite, which is approximately parallel to a close packed direction of their parent γ [10–13].

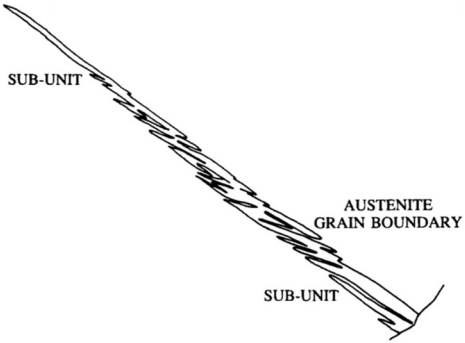

Figure 2-1: A schematic representation of a bainitic sheaf showing the sub-units Reprinted by permission from: Springer Nature, Metallurgical transactions, A, Physical metallurgy and materials science [10].

Bainite forms by a shear mechanism, accommodated by plastic deformation of the parent γ. While the nucleation mechanism for bainite is displacive, it is however, not diffusionless. Contrary to earlier literature sources, α_b forms initially with the same C content as the parent γ which then partitions into the surrounding γ [10]. A key point to note in the bainitic reaction is that it proceeds under conditions of paraequilibrium, where only the interstitial atoms can diffuse freely while the substitutional ones remain homogenous throughout the whole microstructure. The nucleation of new subunits at the tips of old subunits is also more favourable, since the γ near the tip is the least enriched with partitioned C when compared to γ adjacent to the broad surface of the subunit. The subunit size is limited because of the plastic relaxation of the transformation strains and the presence of dislocations at the interface, partitioning C is encouraged to migrate to those dislocations forming Cottrell atmospheres hindering further growth after the accumulation of a certain amount of C at the interface. This is evidenced by the fact that the subunit size increases with the decrease of the C percentage of the alloy, as the Cottrell atmospheres formed would serve to inhibit further subunit growth [10,11,14,15].

After nucleating at parent γ grain boundaries, bainite sheaves continue growing inwards into the γ grain centre. Subunits nucleate at the tips of other subunits. A bainitic sheaf is confined within its parent γ grain. Impingement and γ twin boundaries stop the growth of bainite sheaves. Bainitic sheaves grow in both the length and width direction at proportional rates, however, the longitudinal and lateral growth of bainite sheaves is independent of each other. Therefore, if the longitudinal growth of a bainitic sheaf stops while there is further room for sideways growth, thicker sheaves will be produced [10].

The microstructure of bainite, as well as its morphology, change with the transformation temperature. At lower temperatures, the morphology of bainitic subunits can take up a plate like form, on the other hand, their width is not affected by the γ grain size or the bainitic sheaf size. In addition to that, the distribution of cementite precipitates changes as the transformation temperature drops, producing two distinct microstructures, upper and lower bainite. At higher temperatures where the time required for C to partition into γ is less than the time required for carbide precipitation, α_b does not contain any carbide precipitates. γ is then enriched with C, when its concentration exceeds the extrapolated γ/γ + cementite phase boundary, cementite precipitates from γ, reducing the C concentration of γ and stimulating further ferrite transformation forming upper bainite. This cementite precipitating between bainitic subunits is responsible for the low ductility properties of bainitic microstructures. On the other hand, at lower temperatures where the time required for C partitioning is comparable to that required for cementite precipitation, carbides precipitate in both the α and the γ and lower bainite is formed. The presence of carbide precipitates in the α_b results in lower C in the γ and consequently less cementite between the bainitic subunits. This serves to explain why the lower bainite has better elongation properties than upper bainite of the same alloy [10].

2.2. Carbide-free bainite

As mentioned, the presence of coarse carbides is detrimental to the microstructure and its commercial utilization. Microstructures consisting of only α_b and γ_r are capable of tensile strengths above 1 GPa at 20 EL%. Adding amounts in excess of 1 wt.% of Si and/or Al is necessary to suppress the precipitation of the unwanted cementite phase [16]. The absence of a precipitating carbide phase means that the excess C atoms in the transforming α_b would partition into the surrounding γ enriching and stabilizing it. A considerable advantage of carbide free bainite is their low cost, due to their reliance on a low degree of alloying and low temperature austempering treatments [1,8]. The suppression of carbide precipitation enable the use of bainitic steels in a wide range of applications such as automotive, gear, bearing and railway industries [17].

2.2.1. The incomplete reaction phenomenon

Bainitic reactions have been reported to not reach completion in a number of alloys, even in conventional alloy steels. High hardenability steels were found to experience an initial transformation to bainite that ceases after reaching a certain bainite volume percentage. The maximum attainable bainite fraction depends on the isothermal transformation temperature, increasing with its decrease. In addition to that, it was found that in steels with high nominal C content, the residual phases between the α subunits contain γ_r due to their rapid enrichment with large amounts of C. Usually, for the bainitic reaction to proceed, carbides must precipitate from the enriched γ, lowering its C content and enabling further transformation into α. Carbon partitioning and carbide precipitation can therefore be considered as two competing mechanisms that control how far the bainitic reaction proceeds. In alloys where carbide precipitation is fast, the C partitioning into γ is unable to compensate the C lost to precipitation and thus the γ is not stabilized and the reaction proceeds. On the

other hand, when the precipitation lags behind the formation of α_b, the γ is enriched with C and stabilized and the reaction ceases. It is the extent of this lag that controls the incomplete reaction phenomenon [10,11,18].

In order to properly assess the stability of the γ phase at such low temperatures where γ is not in thermodynamic equilibrium, an extrapolation of the α-γ phase boundary can be made. This extrapolated phase boundary line would represent a condition where γ and α of the same chemical composition are in equilibrium. Such a line is known as the T_0 line, defining for each C percentage a "T_0" temperature below which a displacive transformation from γ to α (here α_b) can occur [11]. In actual practice however, a modification to the T_0 line is required. Due to the displacive nature of the transformation, the stored energy of α needs to be taken into account when representing the phase equilibrium, hence the T'_0 curve is used, accounting for the stored energy of α [5].

2.3. Nano-bainitic steels

Carbide free nB steels offer an interesting combination of high mechanical properties and tailorability achievable through simple, inexpensive, low temperature isothermal treatments [16,19–21]. An optimum nB microstructure consists of nano-sized bainitic α lamellae surrounded by thin layers of γ_r, which is only obtainable at low austempering temperatures close to the Ms [4,22–24]. The possibility of inexpensive, low temperature heat treatment cycles and the capability of nB steels to achieve impressive combinations of strength and ductility are factors that make nB a good candidate for replacing conventional AHSS. On the other hand, long transformation times and expensive alloying strategies still hinder their utilization in industry [13,19,20].

2.3.1. Phases

nB steels often exhibit complex microstructures that include a number of phases, each one contributing positively or negatively to their unique properties. While an ideal nB microstructure should only contain α_b and film γ_r. However, it is common for other phases like blocky γ, martensite, and even some fine carbide precipitates to be found in nB microstructures [25]. The strength component of nB steels is provided by the α_b platelets. Unlike other steel alloys, these α platelets with thicknesses in the range of 20 – 40 nm rely on their fineness for strength, and thus are not directly affected by the C content, though the C content indirectly alters the strength by altering the maximum attainable amount of α_b and affecting the thickness of bainitic subunits [5,6].

Bainitic alloys generally, and nB microstructures specifically are reported to have high dislocation densities in both the α and γ phases. A 0.07 wt.% C, 0.23 wt.% Ti steel alloy contains allotriomorphic α with a dislocation density of 0.5×10^{14} m^{-2} when isothermally transformed at 800 °C. On the other hand, when isothermally transformed at 650 °C, contains upper α_b with a dislocation density of 4×10^{14} m^{-2}. The increase in dislocation density after bainitic transformation is attributed to the displacive nature of the reaction and the associated plastic accommodation of resulting shear strains [10]. Garcia-Mateo et al. studied the contribution of bainite thickness and dislocation density to the overall strength of nB alloys. While the microstructure of nB steels is known to have very high dislocation densities, the contribution of bainite thickness to microstructural strength was found to be 2 - 3 times more than that of the dislocation density. The strength contribution of bainite thickness was calculated as 1.1 and 1.6 GPa for the two alloys studied, while the contribution of the dislocation density was calculated to be around 500 MPa [7].

Even after its partitioning into γ, α_b is found to be supersaturated with C, commonly segregating at dislocation sites [7,10,11]. Caballero et al. reported the presence of a

limited amount of small carbide precipitates inside the α_b. The observed particles had a length of 175 nm and a width of 20 nm [5]. In another study, Caballero et al. also reported the precipitation of carbides inside α_b, mentioning the presence of fine η-carbides and cementite detected in α_b by atom-probe tomography (APT) and synchrotron high energy X-ray diffraction (XRD) measurements [26].

While the strength component of the microstructure derives from the fine, nano-sized α subunits, the contribution of the γ_r to the mechanical properties of nB steels is, however, morphology dependent. A typical nB microstructure has γ_r in two different morphologies, large γ_r islands (blocky γ_r), and film γ that is located between the α_b subunits [4,5,16,27]. Upon loading, blocky γ_r is more susceptible to strain induced transformation into martensite (TRIP) at lower strains owing to its lower stability and lower C content at the centre [28]. While this phenomenon improves ductility at low rates of deformation, it is detrimental to the impact properties of the steel produced, which is attributed of the constant formation of a brittle martensitic phase at the advancing crack tip via the TRIP effect [27].

Literature mentions that a fraction of 0.2 - 0.4 γ_r is a prerequisite for the TRIP effect to occur [27]. However, this transformation can be suppressed through the stabilization of γ_r by the presence of a surrounding hard phase, or by refining the grain size. Consequently, the film γ produced during the bainitic transformation at low temperature is more stable and less prone to the TRIP effect at low strains [4,13]. On the other hand, Dong et al. report that both high stability and low stability γ_r are detrimental to ductility, and propose an optimum level of C enrichment providing γ that would enable the TRIP phenomenon at sufficiently high strain levels to aid the deformation process [29]. The ability of γ to transform to martensite via the TRIP phenomenon at appropriate strain levels grants the γ grains the ability to increase the strain hardening of the microstructure, improving the total elongation. Henceforth,

the total elongation and strain hardening properties of a nB steel are highly dependent on the morphology and stability of the γ_r in the microstructure [7].

An important factor affecting the bainite thickness, and consequently overall mechanical properties, is the γ strength. Due to the plastic relaxation required for the displacive transformation to take place, stronger γ translates to finer bainite platelets. On the other hand, the transformation temperature has no direct effect on the bainite thickness, and the strengthening effect from transforming at lower temperature is the indirect result of two factors. First of which is the increase in γ strength as the temperature is lowered. While the second is the increase in the driving force for the bainite formation and the resulting larger amount of α_b formed, consequently refining it [7,12].

As previously mentioned, γ grains adjacent to bainite platelets are more enriched in C. The same also holds true for smaller γ grains when compared to larger ones due to the larger diffusion distance required for the enrichment of larger γ grains. A consequence of this is that the C distribution in γ is not homogenous, and attempts at measuring the austenite C content (Cγ) via methods such as XRD would lead to an overestimation of the actual Cγ [10].

While martensite is an undesirable phase in a nB microstructure, the difficulty in maintaining the stability of large γ grains often means that fractions of them transform into martensite during cooling. The change in stability with C diffusion distance in a large γ_r grain often means that martensite grains don't exist independently, they are often found as part of larger γ grains, where the unstable sections transform to martensite and those properly enriched are stabilized at room temperature as γ_r. These regions are sometimes referred to as martensite/γ (M/A) islands. In a study on the brittle fracture of bainitic steels, Asako et al. report that the M/A islands, resulting from the low stability of large γ grains discussed earlier, negatively influence the fracture toughness of the aforementioned steels. Micro-

cracks are initiated at the M/A grains and then propagate through the boundaries between M/A and α leading to brittle fracture. On the other hand, micro-cracks initiated in film γ do not catastrophically propagate, and only cause void formation leading to ductile fracture [30,31]. Yang et al. further report that the presence of ductile γ_r films between α_b laths serve to blunt the tip of an advancing crack, hence improving the overall toughness of the steel [32].

2.3.2. Alloying strategies

nB steel alloys rely on extensive alloying to enable the formation of its complex microstructure. Proper alloy design depends on understanding the requirements for a successful nB microstructure. Forming a nano-scaled bainitic structure requires heat treatment at low temperatures, for which a low martensite start temperature (Ms) is required. In addition to that, sufficient hardenability is needed to avoid the formation of any undesirable α and pearlite during cooling. On the other hand, Amel-Farzad et. al report an optimum austempering value of 200 °C for a 1.15 wt.% C, 2.15 wt.% Si, 1.58 wt.% Co, 0.89 wt.% Al, 0.58 wt.% Cr, 0.25 wt.% Mo nB alloy, below which the properties of the nB generated are lowered [33]. A persistent problem with nB microstructures is that the low temperatures used dictate slow kinetics, consequently, the transformation times are long [13,16,24,32]. A drawback that can be tackled via a number of processing and alloying routes discussed in later sections of this thesis.

The need for a low Ms implies a high C content as a requirement [7,13,19,21,27,32]. On the other hand, the use of medium C [24,34], and even low C steels [35] has been reported in literature. In addition to the weldability and formability difficulties that arise from a high C percentage, the increased C fraction has other drawbacks in nB alloys. A high C fraction translates into a higher amount of carbon rich γ_r, consequently increasing both its volume fraction and grain size. This lowers the maximum attainable fraction of α_b, as well as increasing the amount of blocky γ in

the microstructure, both of which are disadvantageous for the mechanical properties [4,23,24,27,28,30,35]. Carbon also retards the kinetics of the bainite transformation, hence one of the approaches to reducing transformation times is via the reduction of the C fraction in the starting alloy. Other alloying solutions or additional processing routes would be then required to attain low Ms at lower C contents [16,24,35].

Silicon is an essential addition to nB alloys, for its role in hindering cementite precipitation. Si is known to be insoluble in cementite, necessitating its diffusion away from a γ region to enable the formation of a carbide nucleus. As previously mentioned in **Section 2.1**, the bainitic transformation occurs under conditions of paraequilibrium, and thus the carbide precipitation is delayed to timeframes much longer than the completion of the bainitic transformation [10]. Si percentages as high as 2 % are not uncommon in nB alloys [4,13,14,16,27,32].

Manganese is a common element for hardenability. In addition to that, Mn lowers the Ms of a steel alloy. On the other hand, Mn slows down the bainitic transformation kinetics as well as lowering the C concentration at T_0, consequently reducing the maximum attainable bainite fraction. Reducing the amount of Mn is a well reported method to reduce transformation times and increase the fraction of bainite formed. Additions of Cr and/or Co are then employed to compensate for the hardenability drop, with Co also having the additional effect of accelerating the bainite transformation kinetics [13,16,19,24,32,35].

Co is known to be an α stabilizer. It has been reported as an effective means of accelerating the bainite reaction. Amounts up to 2 wt.% in a nB alloy have been found to reduce the bainitic transformation time via increasing the free energy change from γ to α [5,6]. On the other hand, Co is an expensive element that is - from an economical point of view - best avoided.

Aluminium is an interesting alloying option with regards to nB steels. It is reported to accelerate the bainitic transformation kinetics, while delaying carbide precipitation [16]. However, care should be taken when adding Al, as it has the negative effects of raising the Ms along with the creation of a γ-loop, consequently making the strategy of reducing the C content along with adding Al to reduce transformation times a difficult one [13,14,16,19,24,32,35–37]. On the other hand, Al is known to not provide any solid solution strengthening for steel, and thus any strengthening in Al containing nB steels would be a result of an increase in the driving force for the transformation and the consequent refining of the microstructure [38].

A number of elements are commonly added to improve the hardenability of nB steels. The formation of any high temperature γ decomposition products such as α or pearlite is detrimental to the mechanical properties of nB microstructures. While Ni can be used to suppress the Ms, Yang and Bhadeshia report that it diminishes the temperature region between Bs and Ms temperatures [39]. Boron is another element to be added in amounts less than 0.0005 wt.% to increase hardenability. The advantage of using B is that it offers an economical alternative to other commonly used hardenability elements [40]. The segregation of B to the γ grain boundaries reduces the grain boundary energy consequently inhibiting the formation of high temperature γ decomposition products, thus promoting the generation of displacively transformed phases [41]. A more common element added to improve the hardenability of nB steels is Cr [16]. It has been reported to shift the T_0 curve to lower C contents [21]. Another good hardenability addition is Mo, as it imparts large increases in hardenability without affecting the bainite transformation kinetics. Additionally, it counters temper embrittlement due to MnS segregation at the grain boundaries [16].

A number of concepts need to be applied for an optimized nB microstructure, each aiming to tackle one of the difficulties faced when designing such alloys. The incomplete reaction phenomenon always limits the maximum attainable fraction of α_b, this can be circumvented by modifying the relative stabilities of γ and α. Adding alloying elements that stabilize α (Al and Co) or lowering the amount of alloying elements that stabilize γ (Mn and C) should shift the T_0 curve towards higher C percentages. This would allow more bainite to form before the reaction ceases, as well as reduce the amount of unstable blocky γ in the microstructure [5,6]. Another advantage of this strategy is the accompanying acceleration in transformation time. As the kinetics of the transformation is dependent on the relative stabilities of α and γ at the transformation temperature which governs the driving force for the transformation [6].

2.4. Acceleration of nB

One of the major drawbacks of nB microstructures is their long transformation times. As shown in **Table 2-1**, austempering times of several days are not unheard of in the early literature dealing with nB, and recent literature still discusses transformation times of several hours. Long heat treatment durations hinder the practicality of mass-production of nB steel grades reducing their attractiveness for the steel industry. Consequently, the acceleration of nB transformation kinetics is the main focus for research in this field, with all other aims taking a back seat to this one. Approaches for accelerating the transformation time are discussed in this section.

Table 2-1: Overview of nB alloy development in the last 15 years.

Source	C (wt.%)	Si (wt.%)	Mn (wt.%)	Mo (wt.%)	Al (wt.%)	Cr (wt.%)	Co (wt.%)	Ni (wt.%)	V (wt.%)	W (wt.%)	UTS (MPa)	Hardness (HV)	Impact (J)	EL (%)	CS (MPa)	RA	Austempering time (s)	Condition
[7]	0.79	1.56	1.98	0.24	1.01	1.01	1.51	-	-	-	2300	-	-	7	-	0.12	345600	Isothermal
	0.8	1.59	2.01	0.24	-	1	1.51	-	-	-	2200	-	-	5	-	0.18	345600	Isothermal
	0.8	1.59	2.01	0.24	-	1	1.51	-	-	-	2100	-	-	19	-	0.21	57600	Isothermal
	0.79	1.56	1.98	0.24	1.01	1.01	1.51	-	-	-	1900	-	-	9	-	0.21	57600	Isothermal
	0.8	1.59	2.01	0.24	-	1	1.51	-	-	-	1800	-	-	30	-	0.38	21600	Isothermal
	0.79	1.56	1.98	0.24	1.01	1.01	1.51	-	-	-	1700	-	-	27	-	0.25	21600	Isothermal
[35]	0.26	1.65	3.44	0.24	0.9	1.14	0.495	1.85	-	-	-	-	-	-	2100	0.2	19440	Isothermal
	0.26	1.65	3.44	0.24	0.9	1.14	0.495	1.85	-	-	-	-	-	-	2200	0.145	21600	Two-Step
[42]	0.34	1.47	1.2	0.24	0.54	0.95	1.04	0.91	0.1	0.99	1450	-	-	15	-	0.24	600	Isothermal
[21]	0.8	1.5	2	0.25	1	1	1.5	-	-	-	1950	-	13	-	-	0.046	259200	Isothermal
	0.8	1.5	2	0.25	1	1	1.5	-	-	-	1850	-	23	-	-	0.085	57600	Isothermal
	0.8	1.5	2	0.25	1	1	1.5	-	-	-	1650	-	35	-	-	0.09	21600	Isothermal
[32]	0.83	1.56	1.37	-	1.44	0.81	-	-	-	0.87	2375	-	7.8	6.7	-	0.125	86400	Isothermal
	0.83	1.56	1.37	-	1.44	0.81	-	-	-	0.87	2139	-	22.2	6.8	-	0.169	43200	Isothermal
	0.83	1.56	1.37	-	1.44	0.81	-	-	-	0.87	2080	-	20.6	7.8	-	0.18	14400	Isothermal

Source	C (wt.%)	Si (wt.%)	Mn (wt.%)	Mo (wt.%)	Al (wt.%)	Cr (wt.%)	Co (wt.%)	Ni (wt.%)	V (wt.%)	W (wt.%)	UTS (MPa)	Hardness (HV)	Impact (J)	EL (%)	CS (MPa)	RA	Austempering time (s)	Condition
[24]	0.42	1.5	2.31	0.25	0.8	1.41	1.46	-	-	-	-	588	-	-	2667	0.168	38880	Inter-critical ferrite
	0.42	1.5	2.31	0.25	0.8	1.41	1.46	-	-	-	-	505	-	-	2280	0.154	21240	Inter-critical ferrite
	0.42	1.5	2.31	0.25	0.8	1.41	1.46	-	-	-	-	596	-	-	2700	0.144	32760	Inter-critical ferrite
	0.42	1.5	2.31	0.25	0.8	1.41	1.46	-	-	-	-	585	-	-	2654	0.142	41040	Inter-critical ferrite
	0.42	1.5	2.31	0.25	0.8	1.41	1.46	-	-	-	2080	561	-	8	2556	0.175	33480	Inter-critical ferrite
	0.42	1.5	2.31	0.25	0.8	1.41	1.46	-	-	-	1918	502	-	20	2300	0.2	25920	Inter-critical ferrite
	0.42	1.5	2.31	0.25	0.8	1.41	1.46	-	-	-	1538	571	-	4	2624	0.163	31680	Inter-critical ferrite
	0.42	1.5	2.31	0.25	0.8	1.41	1.46	-	-	-	1448	520	-	5	2390	0.179	20520	Inter-critical ferrite
[19]	0.91	1.65	2.07	0.25	0.78	1.26	1.56	-	-	-	2127	650	-	4	-	0.34	72000	Ausforming
	0.91	1.65	2.07	0.25	0.78	1.26	1.56	-	-	-	2040	601	-	6.1	-	0.32	1209600	Isothermal
	0.91	1.65	2.07	0.25	0.78	1.26	1.56	-	-	-	2010	664	-	1.3	-	0.36	72000	Ausforming
	0.91	1.65	2.07	0.25	0.78	1.26	1.56	-	-	-	1890	589	-	14.4	-	0.37	72000	Ausforming
	0.91	1.65	2.07	0.25	0.78	1.26	1.56	-	-	-	1802	591	-	5.5	-	0.32	72000	Ausforming

Source	C (wt.%)	Si (wt.%)	Mn (wt.%)	Mo (wt.%)	Al (wt.%)	Cr (wt.%)	Co (wt.%)	Ni (wt.%)	V (wt.%)	W (wt.%)	UTS (MPa)	Hardness (HV)	Impact (J)	EL (%)	CS (MPa)	RA	Austempering time (s)	Condition
[19]	0.91	1.65	2.07	0.25	0.78	1.26	1.56	-	-	-	2127	650	-	4	-	0.34	72000	Ausforming
	0.91	1.65	2.07	0.25	0.78	1.26	1.56	-	-	-	2040	601	-	6.1	-	0.32	1209600	Isothermal
	0.91	1.65	2.07	0.25	0.78	1.26	1.56	-	-	-	2010	664	-	1.3	-	0.36	72000	Ausforming
	0.91	1.65	2.07	0.25	0.78	1.26	1.56	-	-	-	1890	589	-	14.4	-	0.37	72000	Ausforming
	0.91	1.65	2.07	0.25	0.78	1.26	1.56	-	-	-	1802	591	-	5.5	-	0.32	72000	Ausforming
[28]	0.94	1.4	0.9	0.34	1.07	1.18	1.68	2.4	0.1	-	-	400	12	-	-	0.31	21600	Ausforming
	0.94	1.4	0.9	0.34	1.07	1.18	1.68	2.4	0.1	-	-	430	11	-	-	0.27	21600	Isothermal
	0.94	1.4	0.9	0.34	1.07	1.18	1.68	2.4	0.1	-	-	425	10.5	-	-	0.27	14400	Ausforming
	0.94	1.4	0.9	0.34	1.07	1.18	1.68	2.4	0.1	-	-	490	5	-	-	0.23	14400	Isothermal
[13]	0.9	1.5	0.97	0.27	0.87	1.15	1.8	2.54	0.99	-	-	500	-	-	-	0.42	3600	Ausforming
	0.9	1.5	0.97	0.27	0.87	1.15	1.8	2.54	0.99	-	-	-	-	-	-	0.41	7200	Ausforming
	0.9	1.5	0.97	0.27	0.87	1.15	1.8	2.54	0.99	-	-	-	-	-	-	0.38	14400	Ausforming
	0.9	1.5	0.97	0.27	0.87	1.15	1.8	2.54	0.99	-	-	450	-	-	-	0.36	21600	Isothermal
[27]	0.79	2.16	2.02	-	-	1.36	-	-	-	-	-	-	-	49	2000	0.46	864000	Isothermal
	0.79	2.16	2.02	-	-	1.36	-	-	-	-	-	-	-	30	2700	0.32	172800	Isothermal
[34]	0.54	1.7	1.89	0.24	-	-	-	1.63	-	-	-	720	-	-	-	0.21	50400	Ausforming
	0.54	1.7	1.89	0.24	-	-	-	1.63	-	-	-	650	-	-	-	0.18	50400	Ausforming

[19]

Source	C (wt.%)	Si (wt.%)	Mn (wt.%)	Mo (wt.%)	Al (wt.%)	Cr (wt.%)	Co (wt.%)	Ni (wt.%)	V (wt.%)	W (wt.%)	UTS (MPa)	Hardness (HV)	Impact (J)	EL (%)	CS (MPa)	RA	Austempering time (s)	Condition
[34]	0.54	1.7	1.89	0.24	-	-	-	1.63	-	-	-	610	-	-	-	0.12	50400	Isothermal
	0.54	1.7	1.89	0.24	-	-	-	1.63	-	-	-	575	-	-	-	0.15	34920	Isothermal
	0.54	1.7	1.89	0.24	-	-	-	1.63	-	-	-	690	-	-	-	0.12	45000	Ausforming
	0.78	1.51	2	0.27	1.12	1.01	1.41	-	-	-	2300	544		13		0.29	252000	Isothermal
	0.78	1.51	2	0.27	1.12	1.01	1.41	-	-	-	2100	491		17		0.37	54000	Isothermal
[43]	0.78	1.51	2	0.27	1.12	1.01	1.41	-	-	-	2000	452		22		0.41	36000	Isothermal
	0.75	1.94	1.73	0.26	1.72	0.93	-	-	-	-	1982	597	-	14	-	0.36	86400	Isothermal
	0.75	1.94	1.73	0.26	1.72	0.93	-	-	-	-	1914	585	-	15.6	-	0.37	43200	Isothermal
[36]	0.58	1.76	2.21	0.33	-	0.54	0.45	0.76	-	-	1900	-		10.7	-	0.16	864000	Isothermal
	0.78	1.83	1.68	0.26	-	0.95	1.68	-	-	-	1889	651	-	4	-	0.26	86400	Isothermal
	0.75	1.94	1.73	0.26	1.72	0.93	-	-	-	-	1863	559	-	14.8	-	0.35	14400	Isothermal
	0.78	1.83	1.68	0.26	-	0.95	1.68	-	-	-	1848	619	-	9.1	-	0.31	43200	Isothermal
	0.78	1.83	1.68	0.26	-	0.95	1.68	-	-	-	1797	585	-	9.3	-	0.37	14400	Isothermal
	0.48	1.6	2.1	-	1	0.93	-	-	-	-	1740	-	-	11	-	-	3600	Isothermal
	0.48	1.6	2.1	-	1	0.93	-	-	-	-	1680	-	-	13	-	-	5400	Two-Step
[44]	0.48	1.6	2.1	-	1	0.93	-	-	-	-	1650	-	-	15	-	-	9000	Two-Step
	0.48	1.6	2.1	-	1	0.93	-	-	-	-	1600	-	-	14	-	-	14400	Isothermal
	0.48	1.6	2.1	-	1	0.93	-	-	-	-	1550	-	-	15.5	-	-	21600	Two-Step

Source	C (wt.%)	Si (wt.%)	Mn (wt.%)	Mo (wt.%)	Al (wt.%)	Cr (wt.%)	Co (wt.%)	Ni (wt.%)	V (wt.%)	W (wt.%)	UTS (MPa)	Hardness (HV)	Impact (J)	EL (%)	CS (MPa)	RA	Austempering time (s)	Condition
[44]	0.26	1.42	1.7	0.24	-	1.1	-	1.1	0.1	-	1445	450	46	14.1	-	0.12	-	Two-Step
	0.26	1.42	1.7	0.24	-	1.1	-	1.1	0.1	-	1428	434	21	15.1	-	0.15	14400	Isothermal
[45]	0.26	1.42	1.7	0.24	-	1.1	-	1.1	0.1	-	1422	451	49	12.1	-	0.1	-	Two-Step
	0.26	1.42	1.7	0.24	-	1.1	-	1.1	0.1	-	1417	472	50	11.9	-	0.08	-	Three-Step
	0.7	2.59	0.63	-	-	0.59	-	-	-	-	2000	-	-	9.2	-	0.45	7200	Isothermal
	0.7	2.59	0.63	-	-	0.59	-	-	-	-	1885	-	-	31.5	-	0.32	7200	Isothermal
[41]	0.7	2.59	0.63	-	-	0.59	-	-	-	-	1671	-	-	17.4	-	0.42	7200	Isothermal
	0.7	2.59	0.63	-	-	0.59	-	-	-	-	1655	-	-	21.1	-	0.41	7200	Isothermal
	0.7	2.59	0.63	-	-	0.59	-	-	-	-	1580	-	-	31	-	0.22	1800	Isothermal
	0.25	0.42	2.04	0.22	0.024	1.63	-	1.5	-	-	1552	480	-	9.7	-	-	1800	Isothermal
[46]	0.25	0.42	2.06	0.21	0.026	1.55	-	-	-	-	1209	420	-	10.6	-	-	1800	Isothermal
[47]	0.24	0.42	2.08	0.2	0.023	-	-	1.5	-	-	998	400	-	11.3	-	-	1800	Isothermal
	0.22	0.41	2	0.19	0.023	-	-	-	-	-	791	390	-	16.5	-	-	1800	Isothermal
[31]	0.7	2.59	0.63	-	-	0.59	-	-	-	-	1530	-	-	29.5	-	0.31	7200	Isothermal
	0.7	2.59	0.63	-	-	0.59	-	-	-	-	1430	-	-	14.7	-	0.15	7200	Isothermal
[48]	0.27	1.3	1.55	0.15	-	0.5	-	-	0.03	-	1175	-	-	14.7	-	0.12	0	Continuous Cooling
[37]	0.22	1.79	1.98	0.229	-	1	-	-	-	-	1185	-	-	11.7	-	0.05	1800	Isothermal
	0.22	1.79	1.98	0.229	-	1	-	-	-	-	1145	-	-	6.9	-	-	-	Continuous Cooling

Source	C (wt.%)	Si (wt.%)	Mn (wt.%)	Mo (wt.%)	Al (wt.%)	Cr (wt.%)	Co (wt.%)	Ni (wt.%)	V (wt.%)	W (wt.%)	UTS (MPa)	Hardness (HV)	Impact (J)	EL (%)	CS (MPa)	RA	Austempering time (s)	Condition
[37]	0.22	1.84	2.04	0.23	0.5	1.02	-	-	-	-	1119	-	-	14.9	-	0.08	1800	Isothermal
	0.22	1.79	1.98	0.229	-	1	-	-	-	-	1083	-	-	18.3	-	0.1	1800	Isothermal
	0.22	1.84	2.04	0.23	0.5	1.02	-	-	-	-	969	-	-	19.7	-	0.11	1800	Isothermal
	0.22	1.84	2.04	0.23	0.5	1.02	-	-	-	-	907	-	-	9.6	-	-	-	Continuous Cooling
[49]	0.83	1.4	0.65	0.17	-	1.62	-	0.31	-	-	-	-	-	-	-	0.14	108000	Isothermal
	0.83	1.4	0.65	0.17	-	1.62	-	0.31	-	-	-	-	-	-	-	0.087	-	Two-Step
	0.83	1.4	0.65	0.17	-	1.62	-	0.31	-	-	-	-	-	-	-	0.12	-	Two-Step
	0.83	1.4	0.65	0.17	-	1.62	-	0.31	-	-	-	-	-	-	-	0.11	-	Two-Step
[50]	0.7	2.47	1.46	-	0.87	-	-	-	-	-	1620	500	23.8	16.3	-	0.29	12000	Isothermal
	0.7	2.47	1.46	-	0.87	-	-	-	-	-	1700	508	32.2	19.2	-	0.38	7200	Ausforming
	0.7	2.47	1.46	-	0.87	-	-	-	-	-	1650	514	21.8	17.9	-	0.42	6400	Ausforming
	0.7	2.47	1.46	-	0.87	-	-	-	-	-	1850	585	17.1	23.3	-	0.34	3800	Ausforming
[51]	0.7	2.47	1.46	-	0.87	-	-	-	-	-	1447	496	13.1	24.3	-	0.26	4064	Isothermal
	0.7	2.47	1.46	-	0.87	-	-	-	-	-	1522	530	22.7	21.2	-	0.22	5011	Prior Martensite
[52]	0.7	2.47	1.46	-	0.87	-	-	-	-	-	1620	-	-	16.3	-	0.29	11000	Isothermal
	0.7	2.47	1.46	-	0.87	-	-	-	-	-	2000	-	-	24.3	-	0.32	3600	Prior Martensite – Ausforming
[53]	0.85	1.3	1.92	0.29	0.44	-	2.05	-	-	-	1807	-	-	7.2	-	0.18	72000	Isothermal

Source	C (wt.%)	Si (wt.%)	Mn (wt.%)	Mo (wt.%)	Al (wt.%)	Cr (wt.%)	Co (wt.%)	Ni (wt.%)	V (wt.%)	W (wt.%)	UTS (MPa)	Hardness (HV)	Impact (J)	EL (%)	CS (MPa)	RA	Austempering time (s)	Condition
[53]	0.85	1.3	1.92	0.29	0.44	-	2.05	-	-	-	1676	-	-	14	-	0.29	108000	Isothermal
	0.85	1.3	1.92	0.29	0.44	-	2.05	-	-	-	1285	-	-	25	-	0.49	144000	Isothermal
[54]	0.7	2.47	1.18	-	0.87	-	-	-	-	-	1985	673	-	3.4	-	0.23	172800	Isothermal
	0.7	2.47	1.18	-	0.87	-	-	-	-	-	2053	645	-	3.9	-	0.25	129600	Isothermal
	0.7	2.47	1.18	-	0.87	-	-	-	-	-	1846	593	-	10.9	-	0.28	86400	Isothermal
[55]	0.43	1.9	2.83	-	0.57	-	-	-	-	-	1755	563	-	18.1	-	0.23	3600	Ausforming
	0.43	1.9	2.83	-	0.57	-	-	-	-	-	1521	532	-	14.7	-	0.078	5400	Isothermal
[56]	0.51	1.72	0.83	0.25	1.48	0.98	0.56	0.6	-	-	1600	560	42	6	-	0.12	7200	Isothermal
	0.51	1.72	0.83	0.25	1.48	0.98	0.56	0.6	-	-	1850	630	31	6.8	-	0.18	7200	Prior Martensite
	0.51	1.72	0.83	0.25	1.48	0.98	0.56	0.6	-	-	1800	620	32	7	-	0.17	7200	Prior Martensite
	0.51	1.72	0.83	0.25	1.48	0.98	0.56	0.6	-	-	1700	600	34	5.5	-	0.21	7200	Prior Martensite
	0.51	1.72	0.83	0.25	1.48	0.98	0.56	0.6	-	-	1700	580	33	2.5	-	0.18	7200	Prior Martensite
[57]	0.42	2.2	1.7	-	-	0.5	-	-	-	-	1505	-	-	21.2	-	-	7200	Isothermal
	0.42	2.2	1.7	-	-	0.5	-	-	-	-	1515	-	-	31.2	-	-	7200	Prior Martensite
[58]	0.23	1.48	1.52	0.35	-	1.2	-	0.85	-	-	1563	-	24	17.8	-	-	-	Continuous Cooling
	0.18	1.2	1.36	0.49	-	1.4	-	-	-	-	1652	-	18	14.3	-	-	-	Continuous Cooling
[59]	0.26	1.41	0.96	0.25	-	1.1	-	3.1	0.1	-	1435	467	49	15.4	-	0.14	14400	Isothermal
	0.26	1.41	0.96	0.25	-	1.1	-	3.1	0.1	-	1455	451	55	13.6	-	0.09	81000	Two-Step
	0.26	1.41	0.96	0.25	-	1.1	-	3.1	0.1	-	1428	449	61	11.4	-	0.08	275400	Three-Step

2.4.1. Alloying

The alloy composition can be tailored to optimize the properties of a nB microstructure. While the requirements for good mechanical properties are often contradictory. High strength, low Ms nB alloys require very long transformation times making them unfeasible for industrial implementation. On the other hand, a nB alloy designed for short transformation times would have a high Ms and consequently lower strength. However, compromises can be made to reach an optimal combination of mechanical properties and austempering times. The most common alloying strategies employed to stabilize the α and accelerate the bainitic transformation are the addition of Co and Al. Caballero and Bhadeshia added 1.54 wt.% Co and 1.6 wt.% Co + 0.99 wt. % Al to accelerate a high C nB alloy. The combined addition of both Co and Al was reported to be more effective in accelerating the transformation than the effect of only adding Co [5]. On the other hand, it is also well reported that the acceleratory effect of reducing Mn is higher than that of adding Co [16]. There have been attempts in recent literature to replace Co with Al for economic reasons previously mentioned in **Section 2.3.2**. Tian et al. report that adding amounts of as little as 0.5 wt.% Al is sufficient to accelerate the bainitic transformation [37]. Yoozbashi et al. reported bainitic transformation times of 6 h at 300 °C and 72 h at 200 °C for a high C steel alloyed with 0.7 – 1 wt.% Al, resulting in tensile strengths up to 2000 MPa [21]. Yang et al. were able to reduce the transformation time to 4 h at 260 °C and 24 h at 220 °C for a 0.83 wt.% C alloy by adding 1.44 wt.% Al, reaching a maximum tensile strength of 2375 MPa [32]. In addition to that, reducing the C content is also well reported as a method of accelerating the transformation kinetics, however; as mentioned in **Section 2.3.2**, C is needed to sufficiently lower the Ms temperature to enable the formation of a nano-sized structure [28].

2.4.2. Ausforming

It has been established in literature that large grain sizes are detrimental to the mechanical properties of nB [28,60], hence, grain refinement remains an important objective when developing these qualities. Ausforming has been the most popular method researched in recent literature to accelerate the bainitic transformation and for refining both the prior γ and α_b grains. Besides the refinement effect the plastic deformation would have on the γ grains, the resulting increase in strength of the γ hinders the growth of the α_b, consequently leading to smaller bainite lamellae [19,28,34]. In a study by Hu et al. on the effect of ausforming temperature on the bainitic transformation it was found that ausforming at 300 °C promotes the formation of short, fine bainite sheaves whose further growth was retarded by the grain boundaries of a finer-grained parent γ. With higher transformation temperatures however, the dynamic recovery interferes with the abovementioned mechanism, hence reducing the effect of ausforming on the sheave size as the ausforming temperature increases [25].

A number of studies report that ausforming can also accelerate the bainite transformation via increasing the number of nucleation sites. In addition to a reduction in the incubation time, the acceleration becomes more significant as the transformation temperature is reduced [13,23,28,34]. On the other hand, ausforming is said to only accelerate the initial stages of the transformation while retarding the final stage. Hu et al. mentions a more complex relationship between ausforming and bainite transformation kinetics. It was found that ausforming enhances nucleation while retarding growth. In addition to that, they report that the bainitic transformation is accelerated by low-strain, low temperature ausforming, while being retarded by high temperature ausforming. At ausforming temperatures of 450-500 °C Hu et al. report for an 0.4 wt.% C, 2.0 wt.% Si, 2.8 wt.% Mn, 0.04 wt.% Al nB alloy, that the resulting dislocation recovery combined with the deformation

generated sub-grain boundaries lead to an overall decrease in the amount of bainite formed when compared to the non ausformed conditions. Hence claiming 450 °C as a critical temperature above which ausforming would be disadvantageous to bainite formation [25]. It should also be noted that there is a critical strain value beyond which the γ strength becomes too high to plastically accommodate the formation of α_b, hence the transformation is adversely affected [13,23,25,28,34]. Ausforming up to 25 % strain has been reported to accelerate the bainite transformation kinetics, with this acceleration becoming more significant as the ausforming temperature is decreased [34].

Another advantage of ausforming is that it mechanically stabilizes the γ, lowering the Ms temperature thus enabling the generation of nB from steels with lower C contents. Hence improving the formability and weldability of these alloys. A consequence of such stabilization, however, is an increase in the volume fraction of γ_r. The γ grains subjected to work hardening during this process experience an increase in strength that not only stabilizes them at lower temperatures, but also hinders the final stages of the bainitic transformation, resulting in a lower fraction of bainite formed [13,23,24,34,61]. This is consistent with the observation that high temperature ausforming has little to no effect on the transformation kinetics, as it would have minimal effect on the γ strength [25]. Kabirmohammadi et al. report that the fraction of γ_r increases with increasing the strain [13], while Zhao et al. report that the bainite fraction can be increased for the same strain percentage by lowering the transformation temperature, hence increasing the driving force for bainite formation [34].

Ausforming has also been reported to reduce the number of bainite variants forming in the parent γ grain, which in turn reduces the size of the blocky γ in the microstructure [62]. The presence of bainite sheaves with varying orientations is, on the other hand, one of the main reasons behind α_b's good impact properties. Golchin

et al. reported that ausformed samples displayed diminished impact properties when subjected to longer transformation times, owing to a strong variant selection promoted by ausforming [28]. Gong et al. also reported the presence of strong bainite variant selection in ausformed steel samples, which was explained by the introduction of nucleation sites at the active slip planes upon deformation [23]. These findings were further stated by Kabirmohammadi et al. [13].

2.4.3. Partial quenching

Prior generation of a small fraction of martensite followed by austempering is expected to accelerate the bainitic transformation via the introduction of dislocations in the γ grains, thus promoting the nucleation of α_b [22,63,64]. In a study by Gong et al., the generation of 6 % martensite prior to austempering accelerated the rate of bainite transformation through the reduction of the incubation time while the kinetics of the transformation remained unchanged [22]. It was reported that the accelerating effect of martensite introduction was less significant than that of ausforming, because the dislocations introduced by the martensite are localised at the martensite-γ boundaries, while ausforming produces a homogenous distribution of dislocations throughout the structure [22].

2.4.4. Intercritical annealing

A technique used to stabilise γ at lower C percentages is intercritical annealing, the generation of intercritical α, which enriches the surrounding γ via C partitioning [4]. This process has been reported to yield two contradicting effects on the bainite transformation kinetics. The generation of intercritical α reduces the maximum possible fraction of bainite formed, hence accelerating the transformation, while the γ enrichment has the opposite effect [60]. Soliman and Palkowski report that the presence of intercritical α in the vicinity of γ_r islands serves to stabilize the latter, consequently reducing the adverse effect that the γ_r islands have on the mechanical

properties and improving the alloy's ductility [60]. It has been reported however, that the introduction of intercritical α into the microstructure diminishes the tensile properties of the steel produced while improving the compressive strength and fracture strain, hence this approach has not been explored further in recent nB literature [24,65].

2.4.5. Two-step austempering

Multi-step austempering is a heat treatment option that has recently been gaining a lot of attention. It was first introduced by Soliman et al. proposing a 50 % transformation at 305 °C to enrich the γ grains with C, followed by further transformation at 260 °C. This lower temperature lies above the Ms of the newly enriched γ grains, resulting in a finer generation of bainite, unattainable via one-step transformation. It was found that the amount of γ_r was reduced and having higher stability. The compressive strength of the two-step transformed condition was higher than that of the isothermally transformed one [35]. After its introduction in 2010 this processing route did not gain much attention in literature until 2018, where a number of research publications started reporting further on the topic. Recent literature supports the earlier findings of finer bainite size and higher mechanical properties for the two step austempered conditions, while shortening the transformation time [44,66]. Chu et al. combined the partial quenching with a two-step treatment, generating an initial amount of martensite then further austempering at two temperatures with the lower temperature first. The main aim was to reduce the incubation period and accelerate the transformation kinetics, the alloy, however, was intended for use in bearings and thus only its hardness was reported [49]. Generally, the two-step approach is very promising to extend the nB concept into low C steel grades with high Ms values.

2.5. Bake hardening

Bake hardening (BH) is a popular technique employed by the automotive industry to downgauge outer body parts which require high formability to produce. Hence, steels capable of increasing their strength after being formed into the final shape would be well suited for such an application. The initial concept behind BH-steels was based on steels with low dislocation density and controlled interstitial atom content. These steels would be formed into the final structure, increasing their dislocation density, followed by paint baking. During the baking process, where the steel is heated for around 20 min at 170 °C, commonly referred to as BH_{20}, the interstitial atoms diffuse to the dislocations and therewith blocking their movement resulting in an increase in the yield strength [67,68].

The BH process includes two stages: In the first one, free C or interstitial atoms in the microstructure diffuse to dislocations forming Cottrell atmospheres. While during the second, C clusters in the Cottrell atmospheres start to nucleate carbides. The formation of C clusters or fine carbide particles at dislocation sites cause dislocation pinning which increases the yield strength of the BH steel [69–72]. On the other hand, prolonged baking leads to a drop in strength due to over-aging. The phenomenon of over-aging has been attributed in literature to precipitate growth, whereas upon reaching a critical size, their strengthening effectiveness drops [70,71,73].

BH is conventionally performed on ultra-low C steels or interstitial free steels owing to their controlled low amounts of interstitial C in the microstructure. However, other AHSS grades - such as DP steels and nB steels - have shown promising BH properties. These grades of steel possess large amounts of both free C and dislocations that are produced during their heat treatment, hence making them ideal for BH [16,74].

While nB steels seem to be very promising candidates for BH treatments, the available literature discussing its BH properties and response is rather limited, with only the publication by Soliman and Palkowski studying the BH_{20} characteristics of a number of nB alloys. They reported a significant BH effect after a 2 % pre-strain, while the conditions without pre-straining did not result in noticeable BH values [16].

2.6. Drawbacks of currently available alloys

Long transformation times deem nB alloys impractical for commercialization [25,61]. **Figure 2-2 (a)** presents an overview of the most important nB alloys reported in the literature. It can be noticed that while the trend from 2010-2019 is for the transformation time to decrease, this acceleration usually comes at the cost of lowering the tensile strength.

As previously mentioned in **Section 2.4.1**, the addition of Co was among the first attempts to accelerate nB transformation times. However, as evident from **Figure 2-2 (b)**, Co is an expensive element that rendered the aforementioned alloying strategy unfeasible. Attempts have been made to completely replace the accelerating effects of Co with additions of Al and/or reduction in Mn, which retards the transformation by increasing the γ stability [21]. Yoozbashi et al. developed a Co free, high C steel (0.65 – 0.85 wt.% C) nB alloy with 0.7 – 1 wt.% Al additions, the transformation times for these alloys at 300, 250 and 200 °C were 6, 16 and 72 h, respectively, with tensile strengths of up to 2000 MPa [21]. Another Co free nB alloy was developed by Yang et al. with 0.83 wt.% C and 1.44 wt.% Al. Transformation time was found to be 4, 12 and 24 h at 260, 240 and 220 °C, respectively with an UTS reaching up to 2375 MPa [32]. Tian et al. report that a 0.5 wt.% Al promotes the bainitic transformation during both isothermal treatments and continuous cooling [37]. More recent attempts at accelerating the transformation kinetics rely on process

modifications such as ausforming [13,28,34], prior generation of a small martensite fraction [22,63], and intercritical annealing followed by austempering [4,60].

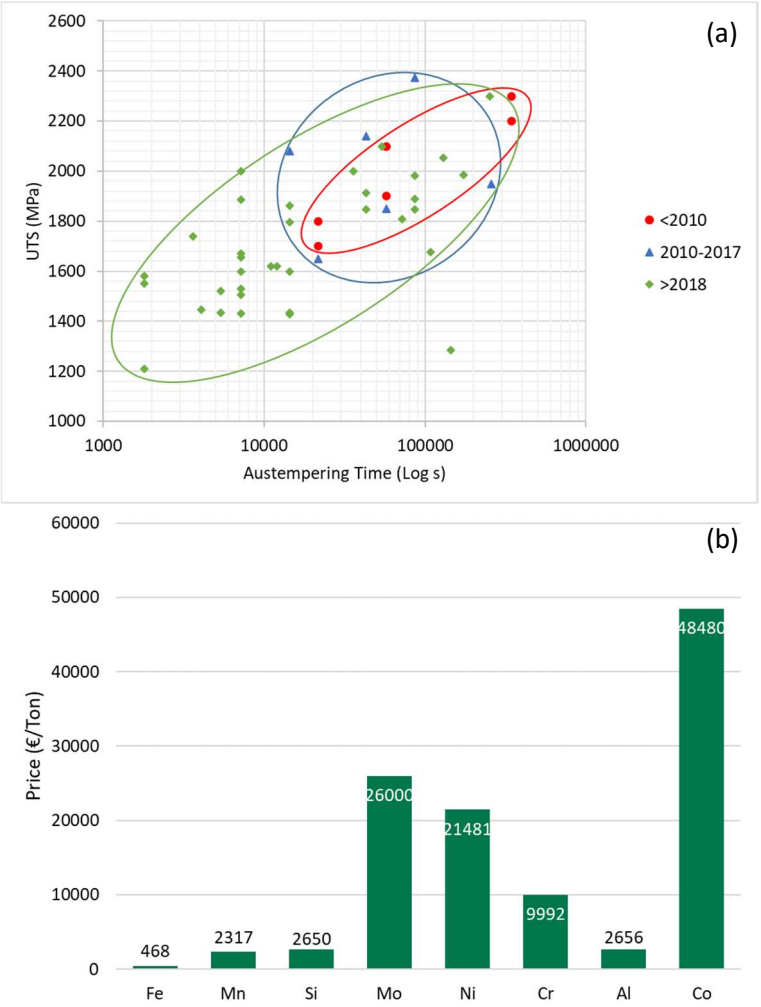

Figure 2-2: (a) Change in tensile strength vs austempering time for nB alloys over the past 15 years as based on the data from Table 2-1, (b) price per ton for the most significant nB alloying elements as based on data from [75,76].

3. Research objectives

As detailed in **Section 2.6**, long transformation times render nB steel grades near impossible to produce on an industrial scale. In addition to that, the costs associated with its current alloying strategies would limit its utilization to niche applications. Earlier research into nB steels focused more on the understanding the microstructure and the underlying thermodynamic and kinetic processes controlling it. On the other hand, recent research endeavours have been more concerned with accelerating the transformation time, mostly via the employment of different processing techniques.

The main aim of this research is to redesign the approach towards nB steel alloying. Three aspects instead of two are taken into consideration throughout this research:

1- High mechanical properties.
2- Fast transformation times.
3- Low cost.

To that aim, new alloying concepts will be introduced, and while the underlying knowledge is well known and reported in the current literature, the proposed concepts will serve to fill the need of affordable nB alloy variants, a gap that is missing in the current literature.

A main pillar upon which this strategy is based is the exclusion of expensive alloying elements. Cobalt is the element most commonly used to accelerate bainitic transformation, owing to its effect as an α stabilizer. However, Co is the most expensive alloying element added to the steel grades in question (see **Figure 2-2 (b)**), hence, alternatives are essential. In addition to Co, a number of (less) expensive hardenability elements such as Ni and Cr are added to nB steels to enable the generation of bainitic microstructures at slower cooling rates, a feature that is important for the production of parts with large cross sections.

Two alloy groups are selected for this research, a high C (A-) group catered towards application requiring high strength in large cross section parts, and a low C (B-) group catered towards applications where weldability is important. To accelerate the transformation time, the affordable α stabilizer Al is to be employed. However, the use of Al carries with it a number of drawbacks, namely, lower hardenability and increased Ms. To obtain sufficiently high mechanical properties on par with those reported in literature, a Ms of around 300 °C would be needed to enable low temperature austempering resulting in bainitic lamellae with thicknesses in the range of 40-70 nm. To counteract the drop in Ms caused by alloying with Al, high amounts of C are to be added to group A, as well as high amounts of Mn to group B. While both C and Mn are known to stabilize the γ phase, hindering the bainitic transformation kinetics, the alloys are designed to ascertain the optimum Al addition to sufficiently accelerate the transformation without compromising the final properties of the alloy. In addition to that, to counteract the negative effects that a high content of Al has on the alloy's hardenability, a combination of C, Mn, Mo as well as microalloying with B was employed to the alloys in question depending on their Al content.

The use of a high Al content as an acceleration strategy has the added benefit of reducing the overall density of the alloy in question, further reinforcing one of the main aims for developing AHSS generally, which is lightweighting. An overlap exists between this approach and that of low-density steels, which rely on high Al contents to reduce the steel's density, with density reductions of 1.3 % for every 1 wt.% Al added reported in literature [77] (p 1731),[78,79]. Bainitic microstructures are however not reported for these types of steels. One of the phases common to high Al steels is δ-ferrite, which is commonly reported as detrimental to the properties of low-density steels. On the other hand, investigating its expected effects on improving the ductility of a high strength microstructure such as nB will be interesting, since

for a number of applications improved ductility would precede high strength in importance.

The development of an alloying concept will also be complemented with a number of processing strategies to further improve the mechanical properties. Continuous cooling will be used to produce the (B-) group variants. The low C content is expected to lead to lower strength γ with a higher Ms, both factors will lead to comparatively lower mechanical properties. Continuous cooling will assist in further refining the bainitic lamellar thickness and increasing the tensile strength of the (B-) group alloys.

While the tensile strength is the most commonly reported property assessing mechanical performance, it is the yield strength that governs the performance of load bearing parts. BH could be used to improve the yield strength of nB alloys with only minimal loss of ductility. To that end, extensive strain aging experiments will be performed to characterize the BH response of select alloys, its governing factors, and the yield strength increases achievable through BH.

4. Experimental work

4.1. Casting and alloy design

Three different approaches to nB alloy design were employed. The approaches are based on a basic concept that draws from the research's objective of reducing both costs and transformation time. Details of the different alloying strategies employed are provided later in this section. Casting was performed using a vacuum furnace into blocks with dimensions as detailed in **Table 4-1**.

Table 4-1: Dimensions of the cast block for each of the alloys investigated in this work.

Alloy	Dimensions (mm^3)
A11	31x31x150
A12	31x31x150
A13	31x31x150, second casting: 145x60x175
A21	31x31x150
A22	31x31x150
A23	31x31x150
A31	31x31x150
A32	31x31x150
A33	31x31x150
B1	145x60x175
B2	145x60x175
B3	145x60x175
B4	145x60x175
A4	145x60x175
B51	31x31x150
B52	31x31x150
B53	31x31x150

4.1.1. Thermodynamic simulation

Thermodynamic simulation was performed via Thermo-Calc software using the TCFE9 database for steel alloys. Thermo-Calc employs the CALPHAD (Computer Coupling of Phase Diagrams and Thermochemistry, previously known as Calculation of Phase Diagrams.) technique to assist in alloy design. The CALPHAD

method relies on calculating the value of the Gibbs free energy to provide a description of the phase diagram and the stable phases [80]. As previously mentioned, the presence of Al in the microstructure stabilizes the α phase and limits the γ to what is called the "γ-loop", which might cause the inability of certain alloys to be fully austenitized and the retention of δ-ferrite at lower temperatures. Hence, ThermoCalc was used to aid in designing alloys that are fully austenitizeable as well as calculate the phase equilibria for the alloys cast as shown in **Figure 4-1**, while the theoretical full austenitization temperatures are listed in **Table 4-2**.

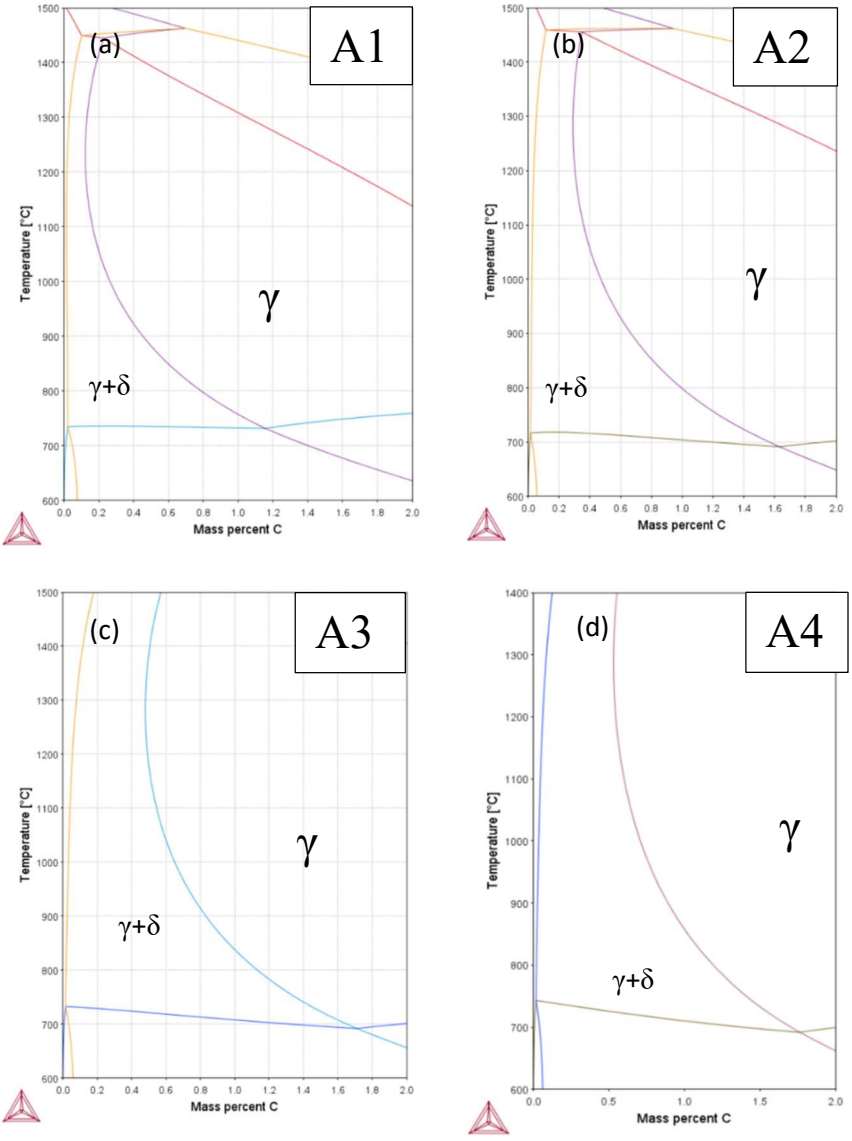

Figure 4-1 A ThermoCalc simulated phase diagrams for (a) A1 alloy system, (b) A2 alloy system, (c) A3 alloy system, (d) A4 alloy.

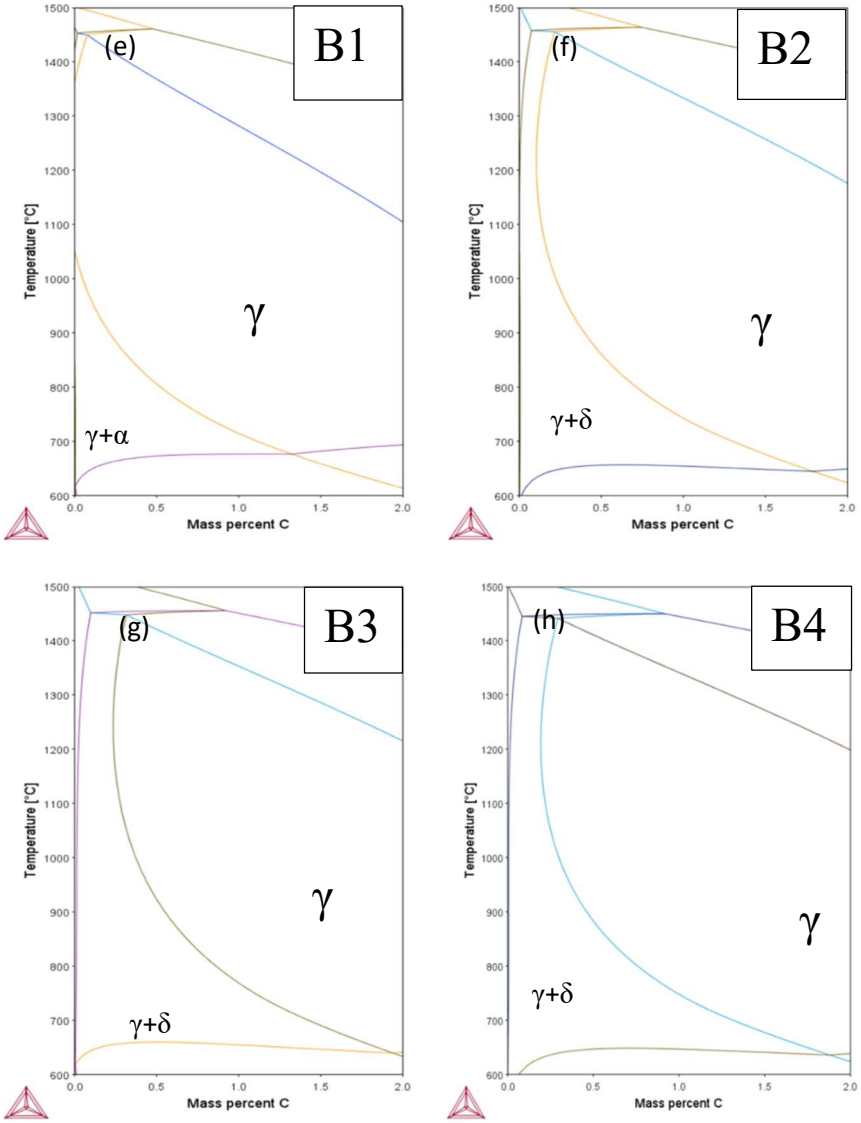

Figure 4-1 B ThermoCalc simulated phase diagrams for (e) B1 alloy, (f) B2 alloy, (g) B3 alloy, (h) B4 alloy.

Table 4-2: ThermoCalc simulated a3 temperatures for the investigated alloys.

Alloy	Simulated a_3 temperatures (°C)
A11	860
A12	816
A13	781
A21	884
A22	850
A23	820
A31	981
A32	926
A33	880
A4	825
B1	835
B2	914
B3	1004
B4	1032
B51	941
B52	970
B53	1010

4.1.2. Low manganese approach

The (A1-) group (**Table 4-3**) relies on the well reported method of reducing Mn to accelerate the bainitic transformation [16,81]. An amount of 0.3 wt.% Mn coupled with around 1 wt.% Al were designed to accelerate the transformation kinetics. Al also serves the purpose of suppressing the cementite formation, however, due to the relatively small amount of Al added, around 1.4 wt.% Si was also added to suppress the cementite formation. Mo was used to improve hardenability and counter temper embrittlement, and C was varied to study its effect on the properties of the nB formed. Alloy A13 was recast for further investigation, the recast block was labelled as A13-2.

Table 4-3: Chemical composition of group A1 alloys.

Alloy/ wt.%	C	Mn	Si	Al	Mo	Fe
A11	0.54	0.29	1.41	0.92	0.55	Bal.
A12	0.67	0.29	1.39	0.95	0.55	Bal.
A13	0.80	0.29	1.35	0.97	0.56	Bal.
A13-2	0.75	0.31	1.36	1.04	0.45	Bal.

4.1.3. High aluminium approach

As previously mentioned in **Section 2.3.2**, Al can be effectively used to accelerate the bainitic transformation. However, amounts of only up to 2 wt.% have been reported in the literature. Groups A2 and A3 (**Table 4-4**) aim to push the current boundary of 2 wt.% Al and investigate the effect of 3 and 5 wt.% on the transformation kinetics and properties of the nB formed. The Mn amount was increased to 1 wt.% to counteract the negative effects of Al on the hardenability. While Si was reduced to around 0.3 wt.% since its cementite suppression effect would be redundant in the presence of large amounts of Al. Mo was added for the same reasons previously mentioned, and the (A3-) group was micro-alloyed with B to further improve its hardenability, as 5 wt.% Al could be detrimental to the alloys ability of being quenched into austempering temperatures without incidents of reconstructive phases forming.

Table 4-4: Chemical composition of the high (Al-), (A2-), (A3-) and (A4-) group alloys.

Alloy/ wt.%	C	Mn	Si	Al	Mo	B	Fe
A21	0.766	0.982	0.273	3.08	0.451	-	Bal.
A22	0.838	0.982	0.287	3.09	0.458	-	Bal.
A23	0.954	0.988	0.281	3.02	0.450	-	Bal.
A31	0.672	0.984	0.264	5.03	0.442	0.0008	Bal.
A32	0.717	0.992	0.267	4.97	0.443	0.0012	Bal.
A33	0.935	0.977	0.256	4.75	0.479	0.0013	Bal.
A4	1.20	0.36	0.277	5.11	0.469	0.0008	Bal.

4.1.4. Medium carbon approach

The (B-) group aims to introduce the strategy of bainite acceleration via the addition of Al to medium C grades, the lower C of this group enables the generation of nB alloys with good weldability. Due to hardenability limitations, most of the research into nB is being performed on high C alloys, with only a handful of papers expanding the concept into medium C steels [35,44,66,82]. Continuous cooling experiments were foreseen for this group. The compositions of the (B-) group are listed in **Table 4-5**.

Table 4-5: Chemical composition of (B-) group alloys.

Alloy/ wt.%	C	Mn	Si	Al	Mo	Fe
B1	0.32	2.78	1.82	0.726	0.235	Bal.
B2	0.30	2.95	0.545	2.06	0.233	Bal.
B3	0.31	2.74	0.314	2.84	0.243	Bal.
B4	0.23	4.17	0.314	3.03	0.240	Bal.

A series of alloys were cast with varying Si content to investigate its effect on the strength of nB alloys. Three alloys, dubbed the (B5-) group, were cast for that aim, their compositions are listed in **Table 4-6**.

Table 4-6: Chemical composition of (B5-) group alloys.

Alloy/ wt.%	C	Mn	Si	Al	Mo	Fe
B51	0.267	2.94	1.04	2.02	0.24	Bal.
B52	0.298	2.97	1.6	1.99	0.24	Bal.
B53	0.259	2.97	2.06	1.95	0.24	Bal.

4.2. Material processing

The cast blocks were homogenized at 1100 °C for 48 h in Ar atmosphere, the oven was then switched off and the blocks left inside to cool down within 12 h. The homogenized blocks were heated to 1100 °C in a muffle furnace in Ar atmosphere, hot rolled using a 12" 2-high rolling machine at a speed of 10 rpm into the appropriate thickness required for the preparation of the different test specimens required for this investigation. The rolled plates were reheated for 1 h at 1100 °C after each rolling pass, and after the final pass was oven cooled in argon atmosphere.

The rolling schedules followed are shown in **Tables 4-7** and **4-8**.

Table 4-8: Rolling schedule for the 31x31x150 mm3 blocks.

Stages	Thickness (mm)	Reduction (%)
Initial	45	
1	40	11
2	30	25
3	20	33
4	14.5	28
5	10.5	28
6	8	24

Table 4-7: Rolling schedule for the 145x60x175 mm3 blocks.

Stages	Thickness (mm)	Reduction (%)
Initial	58	
1	50	14
2	38	24
3	26	32
4	19	27
5	15	21
6	12	20

The rolled plates were then machined into the various standard test specimens detailed in the following sections. Specimens for microscopic investigation were cut from the as cast, homogenized blocks as well as the rolled plates.

While most of the mechanical testing specimens were heat treated in the dilatometer described in **Section 4.4**, a select number of conditions were heat treated in salt baths, namely when upwards of 40 specimens of the same alloy needed to be heat

treated at the same condition as in the case of the BH investigations. Specimens heat treated using this method were first coated with 3 layers of Condaforge 607 graphite coating to minimize surface decarburization, followed by austenitizing in an oven at the temperature required. The austempering was performed in a salt bath using Durferrit AS140 heat treatment salt.

4.3. Dilatometry

Dilatometry is a technique used to measure dimensional changes caused by changes in temperature, whether by thermal expansion or phase change. The Bähr Dil 805A at the Institute for Metallurgy uses the push rod method to measure dimensional changes. Two pushrods coupled at the core section (transducer shown in Figure 4-2) are used in this system, one connected to the sample while the other acts as a reference. This coupling allows real time calibration of the dimension change measurements during testing to provide a high level of accuracy [83].

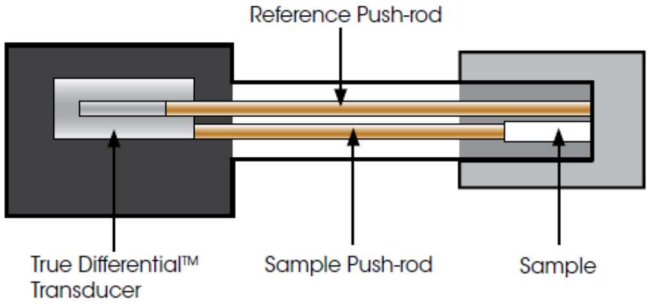

Figure 4-2: Schematic diagram of the measurement system employed in the Bähr Dil 805A dilatometer [83].

Temperature measurements are recorded via Pt/Pt-10% Rh thermocouples spot welded to the test specimens. The push rods used for temperatures below 1100 °C are quartz rods, while alumina rods are employed for higher temperatures. Dimension change measurements are detected by a linear variable differential transducer (LVDT), a sensor that converts linear motion into an electrical signal; this is achieved via the movement of a magnetically permeable core inside a coil

assembly as shown in **Figure 4-3**. Only the primary coil has a current flowing through it, and as the axial position of the core is changed, the induced current in the two secondary coils changes, the core's displacement is measured via measuring the resultant potential difference of the two secondary coils [60,84]. Dilatometric testing was performed using a Bähr Dil 805A dilatometer on φ5x10 mm cylindrical specimens machined from the rolled plates.

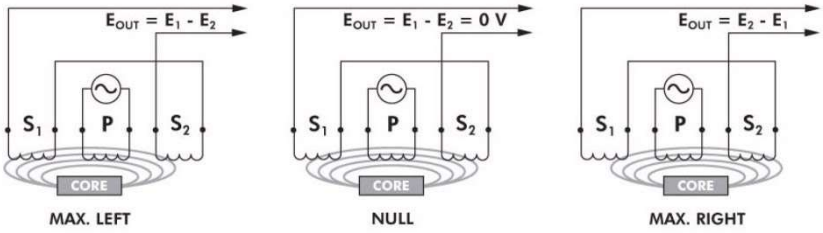

Figure 4-3: Schematic diagram of an LVDT system [84].

4.3.1. Thermal cycles

To design a suitable heat treatment cycles, the martensite start was investigated for all the alloys. Specimens were heated at a rate of 10 $K.s^{-1}$ until full austenitization (**Table 4-9**), held at that temperature for 15 min and followed by quenching at a rate of 100 $K.s^{-1}$ to 50 °C. The martensite start thermal cycles are shown in **Figure 4-4 (a)**.

Table 4-9: Selected austenitization temperatures for the alloys investigated in this work.

Alloy/ Alloy Group	Austenitization Temperature (°C)
A1	950
A2	950
A31	1150
A32	1200
A33	1250
A4	950
B1	1050
B2	1050
B3	1170
B4	1200
B51	1150
B52	1150
B53	1200

It was not possible to fully austenitize the alloys A31 and B4 up to a temperature of 1300 °C. Therefore, it was not possible to obtain a δ-ferrite free microstructure for A31 and B4. This discrepancy between theoretically simulated and dilatometric experimental results has been related to the inadequacy of the current CALPHAD models in dealing with high aluminium steels. A more detailed analysis of the differences between the simulated and experimental values is provided in the results section. As a consequence, however, a δ-ferrite amount of about 10 vol.% was generated in the microstructure of both A31 and B4 yielding a final microstructure of δ-ferrite, αb and γr.

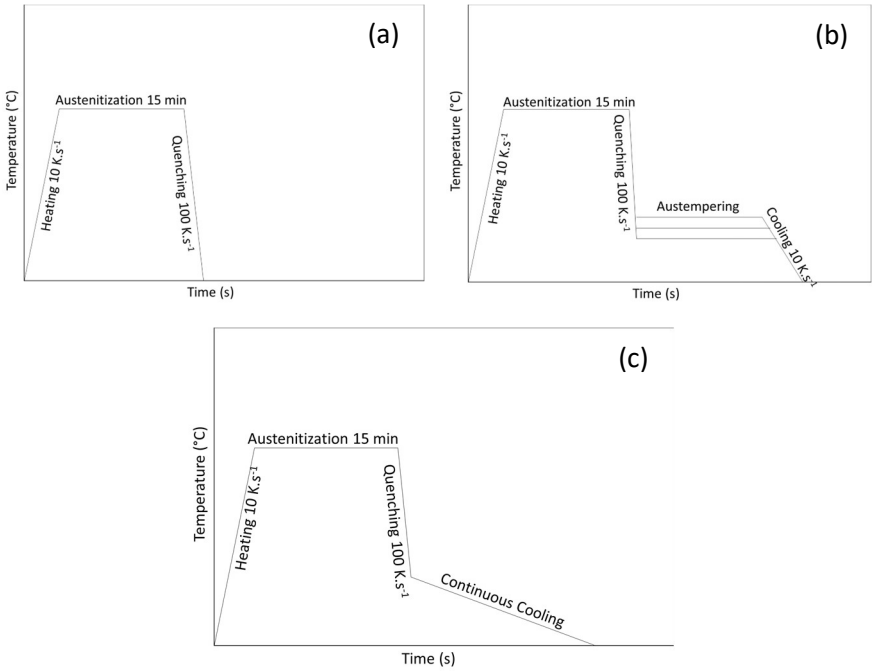

Figure 4-4: Thermal cycles employed during (a) Ms experiments, (b) isothermal bainite formation experiments, (c) continuous cooling experiments.

Following the determination of Ms, all the alloys investigated were isothermally transformed at appropriate temperatures determined according to their respective Ms (discussed later in **Section 5.3**). In addition to isothermal transformation, group B alloy specimens were also transformed via continuous cooling from temperatures above their Ms at cooling rates of different orders of magnitude to estimate the required cooling rate for the transformation to reach completion. Details of the thermal cycles used to generate the nB microstructures are also provided in **Figure 4-4 (b)** and **(c)**.

4.3.2. Determination of phase fractions and transformation times

Dilatometry is a powerful tool that does not only detect the temperatures at which phase transformations occur but can also be used to identify the transformation times and calculate the phase fractions produced during these transformations. The most effective way to determine bainitic transformation times is via interrupting the isothermal treatment at regular intervals followed by XRD testing to detect the fraction of γ_r. While this technique is the most accurate, it is laborious in terms of material consumption, time and expenses, and thus not widely used [6]. Another variation of this technique can be applied by using metallographic analysis instead of XRD to determine the bainite fraction. While this method saves the costs of expensive XRD testing, it is however, still material and time intensive. In addition to that, due to the fine nature of the microstructure, metallographic measurement of phase fractions might not be very accurate [85].

The ASTM A 1033-04 standard recommends using the dilatometric length change vs time plots to determine the transformation time. While this method is commonly used in nB literature [16,60,86], and has been reported by Koo et al. to be in agreement with results from neutron diffraction [87], it is highly reliant on the human factor and thus its results may vary [88].

Another method of assessing dilatometric transformation times is through obtaining the first derivative of the dilation vs time curves and plotting the dilation rate vs time. A representative example of transformation rate vs time curve of the B1 alloy austempered at 310 °C is given in **Figure 4-5**. The transformation rate increases rapidly to a maximum, followed by a steep drop to a value close to zero. Afterwards, the change in rate tapers off slowly and over a long period of time until it reaches zero. The transformation ends when the dilation rate reaches zero, or when the curve becomes horizontal. However, it is inefficient to aim for 100 % completion of a reaction, since, as marked in **Figure 4-5**, 4000 s are required to finish 98 % of the

transformation, while the remaining 2 % require another 4000 s. Hence, transformation times for the alloys studied were selected with efficiency in mind, and to avoid the precipitation of cementite resulting from extended austempering, according to the previously described method. Similar recommendations can be found in literature, where Xu et al. recommend aiming for an optimum value of 95 % transformation. On the other hand, they also state that 'most' of the reaction would be complete within two times the time of maximum transformation rate. However, as shown in **Figure 4-5**, this point is too early in the reaction to be selected as the transformation finish time in the current study [88].

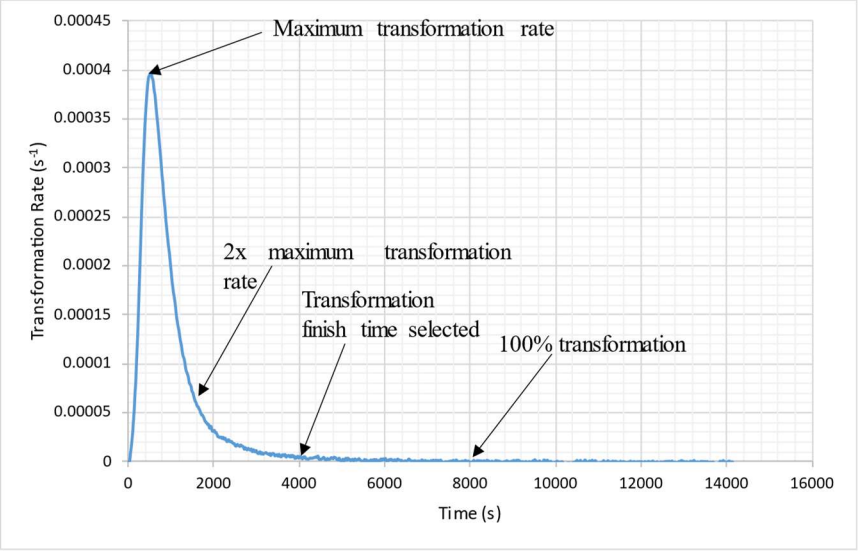

Figure 4-5: Transformation rate vs time curve for the B1 alloy austempered at 310 °C.

4.4. Microscopy

4.4.1. Microscopy

Light optical microscopy (LOM) was performed after every processing stage in the investigation. While optical microscopes are incapable of providing enough

information about the fine-scale microstructure of nB alloys, LOM was a useful quick method to detect unwanted phases as well as the preparation quality for the following scanning electron microscopy (SEM) investigations.

Specimens were ground in gradual steps from 80 to 1200 grit size followed by polishing using a polycrystalline diamond suspension with 6 µm, 3 µm and 1 µm. For the final stage of preparation, the specimens were polished with a silica suspension with 0.04 µm particle size. Specimens were then cleaned with alcohol in an ultrasonic bath and dried after each stage of preparation. A 3 % Nital solution was used for etching for most conditions, while Le Perra reagent was used to investigate deformation induced ferrite grains (DIF). LOM specimens were analysed using an Olympus BX60M optical microscope. To reveal the prior austenite grain size (PAGs) quenched martensitic specimens were tempered at 550 °C for 48 h, which causes a segregation of P and S into the prior austenite grain boundaries to facilitate revealing the grain boundaries after etching. The high C alloys (Group A) were etched with saturated aqueous picric acid solution according to the procedure described in [89], while the lower C alloys (Group B) responded better to the Bechet-Beaujard reagent [90].

Specimens planned for SEM were prepared via the same grinding and polishing procedure as previously detailed in 4.4.1, followed by deep Nital etching. Specimens were then coated with gold for imaging or graphite for energy dispersive X-ray (EDX) analysis and analysed using a Camscan SEM. For the bainite thickness measurements, ten pictures were taken per specimen at a magnification of 15000X and the image analysis software ImageJ was used to measure the lamellar thickness via the line intercept method. A total of ten measurements were taken per picture and, therewith, 100 measurements per specimen. Additionally, selected conditions were sent externally to undergo transmission electron microscopy (TEM) investigations at the GFE facility at the RWTH Aachen university.

The metallography laboratory at IMET was upgraded at the beginning of 2021, adding a Zeiss AX10 LOM and Zeiss EVO 15 SEM to its equipment. A number of supplementary metallographic investigations that were performed towards the end of this research in 2021 employed the use of the newly acquired equipment.

4.4.2. Synchrotron X-ray diffraction (XRD)

XRD experiments were performed using the synchrotron XRD at the Deutsches Elektronen-Synchrotron (DESY), Hamburg, Germany. The basic concept of operation behind a synchrotron is that charged particles produce an electromagnetic radiation while accelerating. The accelerated electrons are maintained in "storage rings", where they remain in motion in a circular path at a speed close to the speed of light. A constantly moving charged particle does not generate radiation, and the particles rotating inside a storage ring do not produce sufficient intensity for the experiments required. Therefore, undulators are used to amplify the intensity of the radiation beam. Undulators are series of alternating magnetic poles that cause the electron beam to vibrate in a sinusoidal pattern as it rotates inside the storage ring, generating a transverse acceleration as a result of the vibration results in more emitted radiation and consequently, higher beam intensity [91]. A significant advantage of synchrotron XRD compared to conventional XRD measurements is the capability of synchrotron radiation is of penetrating the entire thickness of a specimen, hence the measurements obtained are more representative of the overall structure. XRD measurements were conducted using an 0.7 mm x 0.7 mm beam with 87.1 keV and a wavelength of 0.14235 Å. The diffraction pattern was recorded using a Perkin Elmer 1622 flat panel detector with a pixel matrix of 2048 x 2048 and a pixel size of 0.2 mm. Additionally, XRD investigations for group B specimens as well as a number of supplementary investigations were conducted using a Panalytical Emperean DY1654 X-ray diffractometer at the Institute of Non-Metallic Materials at the Clausthal University for Technology.

γ_r percentages were calculated from the integrated intensities of the (111), (200), (220) and (311) γ diffraction peaks and the (110), (200), (211), (220) α diffraction peaks according to the method described by Cullity using Eq. 1 as follows [92]:

$$V_\gamma = \frac{I_\gamma / R_\gamma}{I_\gamma / R_\gamma + I_\alpha / R_\alpha} \quad \text{Eq. 1}$$

where I_α and I_γ are the integrated intensities of α and γ, and R_α and R_γ are the theoretical relative intensities. Details of the calculation procedure can be found in [93].

The Dyson and Holmes equation (Eq. 2) can be used to calculate Cγ through measuring the deviation of the γ lattice parameter "a_γ" from its original value, taking into consideration the effect of the added content of substitutional alloying elements in weight percent "w_x" on a_γ [94].

$$C_\gamma = (a_\gamma - 0.3578 - 0.000095\mathrm{w_{Mn}} - 0.00056\mathrm{w_{Al}} - 0.00031\mathrm{w_{Mo}})/0.0033 \quad \text{Eq. 2}$$

High precision measurements are always necessary when attempting to determine the composition of a phase by means of its lattice parameter; hence, a high precision in θ measurement is essential. However, XRD results are produced in terms of sin θ, which does not linearly vary with the value of θ as sin θ is increased from 0 – 1. **Figure 4-6** illustrates how the value of θ varies with changing sin θ, where it is apparent that as sin θ approaches 1, small deviations in its value result in larger deviations in the value of θ, therefore, a correction function is required for more accurate results [92].

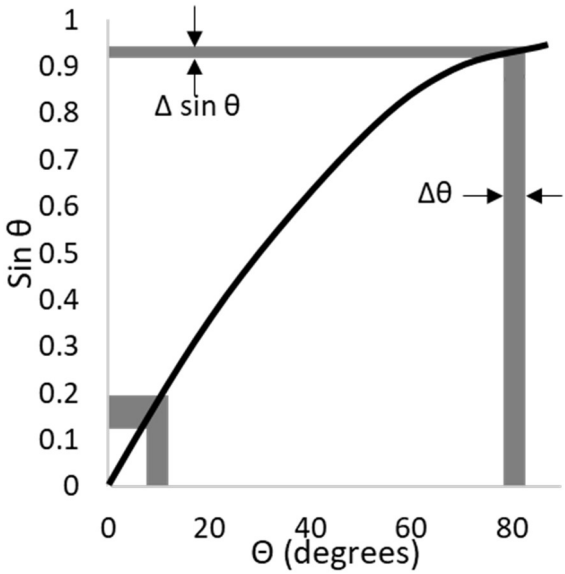

Figure 4-6: Effect of the variation in θ over the accuracy of sin θ as θ is changed from 0 - 90 ° [92].

Several correction functions are created to account for the errors occurring during XRD measurements. For the purpose of this research, the Nelson-Riley (N-R) equation (Eq. 3) was used being accurate at low values of θ used during Synchrotron XRD measurements.

$$\frac{\Delta a}{a_0} = K\left(\frac{co\ ^2\theta}{sin\theta} + \frac{cos^2\theta}{\theta}\right) \text{ Eq. 3}$$

where a_0 is the 'correct' value of the lattice parameter without errors, and K is a constant, hence the value of the lattice parameter can be found by plotting the lattice parameter values obtained vs the N-R function. By extrapolating the linear function, the value of a_0 can be found at the intercept with the y-axis [92].

4.5. Mechanical testing

4.5.1. Tensile test

ASTM E8 subsize tensile specimens with a gauge length of 12.5 mm and a gauge diameter of 2.5 mm were machined from the rolled plates along the rolling direction (RD). Specimens were austempered in the Bähr Dil 805A dilatometer at the transformation temperatures listed in **Section 4.3.1**. Tensile testing was performed on a Zwick/Roell universal testing machine with a 250 kN load cell. The machine is equipped with a video extensometer for accurate strain measurements. A 10 $MPa.s^{-1}$ loading rate was used within the elastic regions, changing to a control by loading speed of 0.0115 $mm.s^{-1}$ during the yielding stage, and finally changing to 0.0067 s^{-1} in the plastic region. This loading plan is based on the DIN – 68921 standard for BH measurements.

4.5.2. Hardness test

Transformed dilatometry specimens were prepared by grinding down to 400 grit size. Vickers (HV30) hardness testing was performed using a Wolpert hardness tester equipped with a digital measurement system, the test was performed according to the ASTM92-83 standard.

4.5.3. Impact and impact transition temperature test

ASTM E23 notched Charpy subsize impact specimens with a 5 x 5 mm^2 cross section and a length of 50 mm were machined in the RD from the rolled steel plates and their bainitic transformation performed in the Bähr Dil 805A dilatometer. The impact transition temperature measurements were performed on regular sized Charpy specimens with a 10 x 10 mm^2 cross section and a length of 50 mm, a stainless-steel flask filled with liquid nitrogen was used as the cooling medium. To accurately reach the required sub-zero temperatures a dummy Charpy impact

specimen with a thermocouple spot welded on the opposite side of the notch was placed inside the liquid nitrogen for 5 min. Afterwards the dummy specimen was removed from the liquid nitrogen bath and placed in its correct test position on the impact machine. The time required for the dummy specimen to reach the test temperatures required was recorded to ascertain the time needed between removing the sample from the liquid nitrogen and performing the test.

4.5.4. Deformation induced ferrite transformation (DIFT)

DIFT was generated in (B-) group alloys (B4 was excluded from this investigation due to the presence of δ-ferrite). The thermo-mechanical (TM) cycles were determined with 5 x 10 mm^2 compression specimens using the DIL805D deformation dilatometer. Due to the difficulty in differentiating the fine DIF grains from the γ_r grains in a bainitic microstructure, martensitic specimens were used to investigate the DIF grains generated. Therefore, specimens were fully austenitized according to the temperatures listed in **Table 4-9**, followed by cooling at a slow rate of 2.5 $K.s^{-1}$ to the deformation temperature in the intercritical region, and held for 10 s for homogenization. A deformation strain of 0.5 was applied followed by an isothermal holding period of 15 or 30 min to allow for the growth of different amounts of DIF. Specimens were then quenched to room temperature (R.T.) and prepared for LOM according to the techniques mentioned in **Section 4.4.1**, etched with Le-Perra reagent where ferrite is expected to etch brown or blue.

Larger compression specimens with the geometry illustrated in **Figure 4-7 (a)** were subjected to the aforementioned TM cycles using the TTS820 simulator, however, after the isothermal holding at the intercritical temperature the specimens were quenched to 350 °C and austempered for 1 h to generate the fine bainitic microstructure required, the full TM cycle is presented in **Figure 4-7 (b)**. After the TM treatment, the specimen was milled to a thickness of 4 mm for tensile testing.

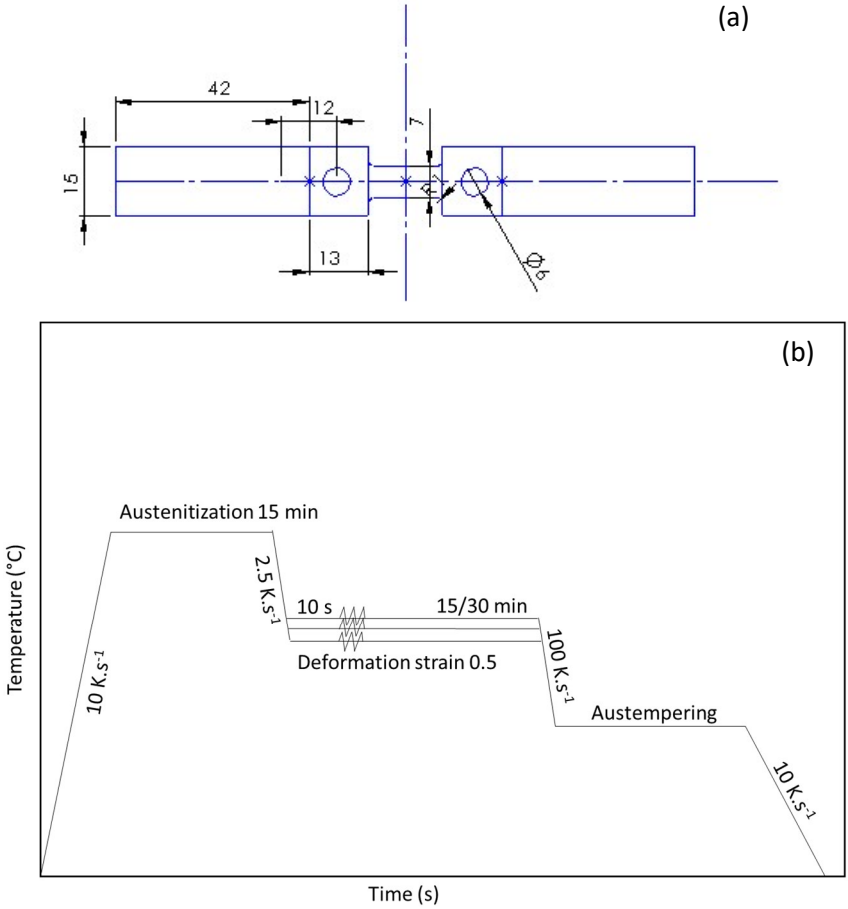

Figure 4-7: (a) Specimens used to generate DIFT via TM cycles performed in the TTS820 TM simulator, (b) thermal cycles employed to generate DIFT.

4.5.5. Bake hardening

Specimens for detailed BH response investigations were heat treated in a molten salt bath using Durferrit AS140 salt at 310 °C. The BH response of nB has been investigated by Soliman and Palkowski [16]; it was found that nB microstructures

do not display a BH effect without pre-straining. Hence, only pre-strained specimens were investigated in this research, subjected to a 2 % pre-strain directly followed by baking at RT, 100, 170, and 200 °C. Specimens were subjected to ageing times from 2 – 10000 min. Over-ageing was not of interest in this study, as it provides no real benefits or advantages. On the other hand, studying the transition from Cottrell atmosphere formation to precipitate formation, corresponding to the lower and upper BH plateaus, respectively, was a main objective for these investigations. Hence, the ageing times selected for each temperature focused mainly on describing the transition from the lower to the upper plateau and did not cover over-ageing. The (A1-) group was subjected to the BH_{20} treatment. By applying a 2 % pre-strain followed by ageing at 170 °C for 20 min, this procedure mimics the strain ageing a steel alloy is subjected to during paint baking in the automotive industry. Furthermore, three alloys (A13-2, B2 and B4) were selected for more intensive BH investigations. A13-2 and B2 were selected to represent the behaviour of the high C and low C alloys, respectively, while B4 was selected to investigate the effect of the presence of δ-ferrite in a nB microstructure on its BH response.

5. Results and discussion

5.1. Analysis and evaluation approach

It must be pointed out that, throughout the course of this dissertation, comparisons will be made between alloy conditions with multiple variables differing between them. While this might not be "scientific" in situations where a research is performed for pure science, in the current scope of work, where the aim is the development of practically viable alloying strategies, this approach was considered as the most suitable one.

As discussed in Chapter 2, the effects of individual elements on the thermodynamics, kinetics, and properties of nB alloys are well covered in literature. Therefore, the effects of a single element on a nB microstructure are not considered here in terms of the element itself, rather in terms of the alloying strategy that enables the use of this element. An example for this is the acceleration strategy relying on alloying with high Al contents, which also necessitates the addition of higher γ stabilizing C and Mn contents to maintain the hardenability of the alloy. In this case, the high Al alloys will be compared with ones lower in their Al content which also have lower Mn and C contents. In that case the disadvantages of the necessary high amounts of γ stabilizing elements are considered an innate part of the overall strategy.

5.2. The as-rolled structure

Figure 5-1 shows the as rolled structure for the alloys investigated in this work. The microstructures display a ferrite – pearlite composition, indicating a hypo-eutectoid nature. This confirms the ThermocCalc simulations of the alloy phase diagrams presented in **Figure 4-1**, indicating that the addition of Al shifts the eutectoid point towards higher C contents. Additionally, whether an alloy is fully austenitizeable or not can clearly be determined by the morphology of the α grains. Fully austenitizeable alloys contain allotriomorphic α that is more equiaxed in nature,

regardless of its size. On the other hand, A31 and B4 display the typical elongated large δ-ferrite grain morphology which is inherited from the solidification process.

5.3. Definition of the heat treatment cycles

Ms temperatures for the alloys investigated are listed in **Table 5-1**, with the corresponding change in length vs. temperature curves during quenching provided in **Figure 5-2**. Austempering temperatures were selected according to each alloy's Ms, see **Table 5-2**. A number of criteria were followed for selecting the transformation temperatures, to maintain a fine lamellar structure the first austempering temperature for the high C (A-) group was chosen to be within the range of Ms + 15 °C. Further austempering temperatures were then selected at 15 °C intervals up to 310 °C which was then increased to 350 °C for the higher Al alloys (A2 and A3) owing to their much higher Ms temperatures. A value of 350 °C was chosen as the upper limit as it is commonly reported as the highest austempering temperature at which a microstructure can be considered nB [95]. The difference between the various austempering temperatures was increased to 30 °C for the A13-2 and A4 alloys since it was observed that a 15 °C difference did not result in a large change in properties. Owing to their high Ms, alloys of the low C (B-) group were only austempered at 350 °C, with the exception of B1 which was austempered at both 310 and 350 °C.

Table 5-1: Experimentally determined Ms for the alloys investigated.

Alloy	Ms (°C)	Alloy	Ms (°C)	Alloy	Ms (°C)	Alloy	Ms (°C)	Alloy	Ms (°C)
A11	300	A21	283	A31	335	B1	296	B51	315
A12	265	A22	260	A32	324	B2	318	B52	322
A13	225	A23	250	A33	290	B3	310	B53	312
A13-2	235			A4	173	B4	315		

Table 5-2: Selected austempering temperatures for each of the alloys.

Alloy	Transformation Temperatures (°C)						
A11						310	
A12				280	295	310	
A13	235	250	265	280	295	310	
A21					295	310	350
A22			265	280	295	310	350
A23			265	280	295	310	350
A31							350
A32							350
A33					295	310	350
A4		250		280		310	
A13-2		250		280		310	
B1						310	350
B2, B3, B4, B51, B52, B53							350

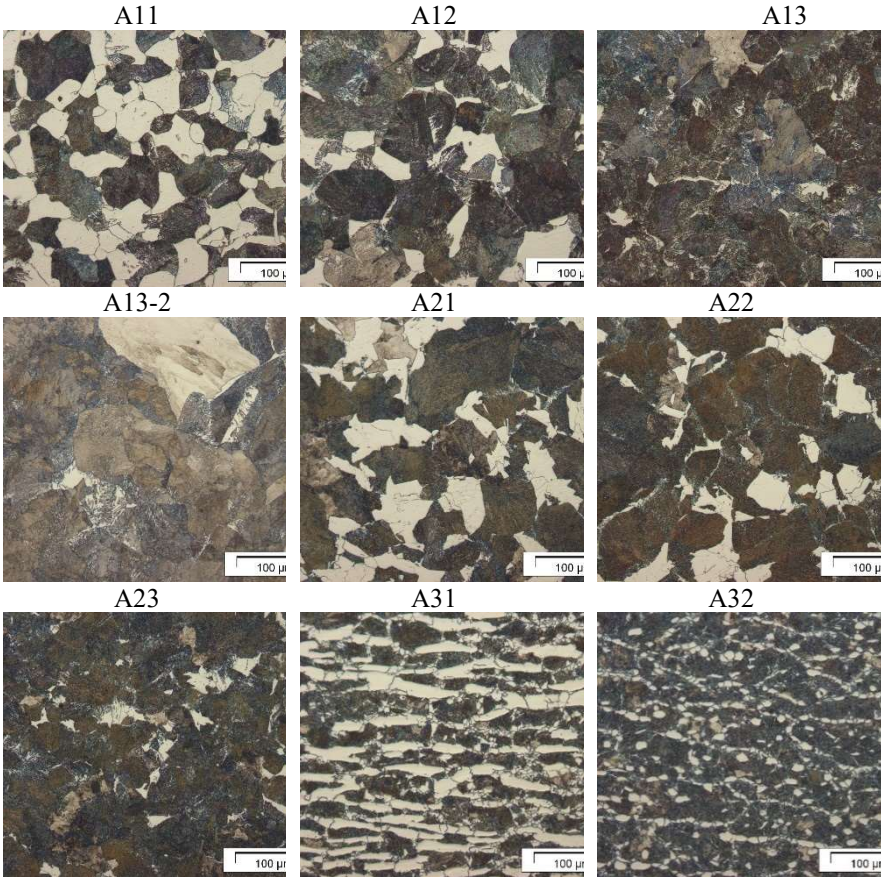

Figure 5-1 A: Structures of the as-rolled alloys.

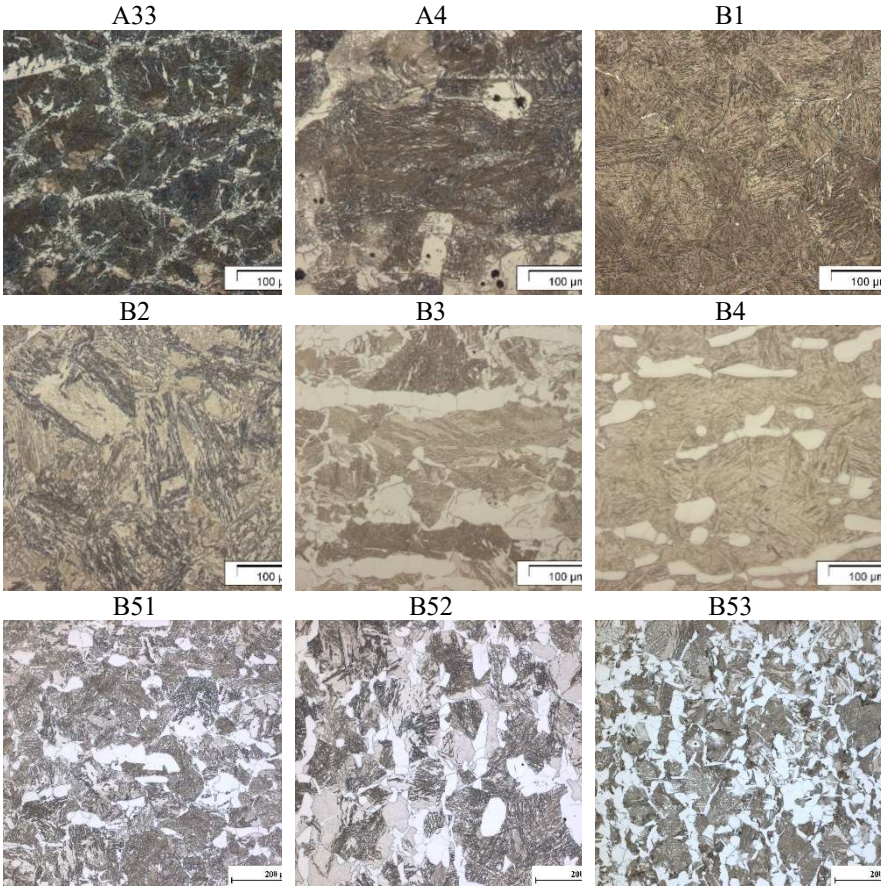

Figure 5-2 B: Structures of the as-rolled alloys.

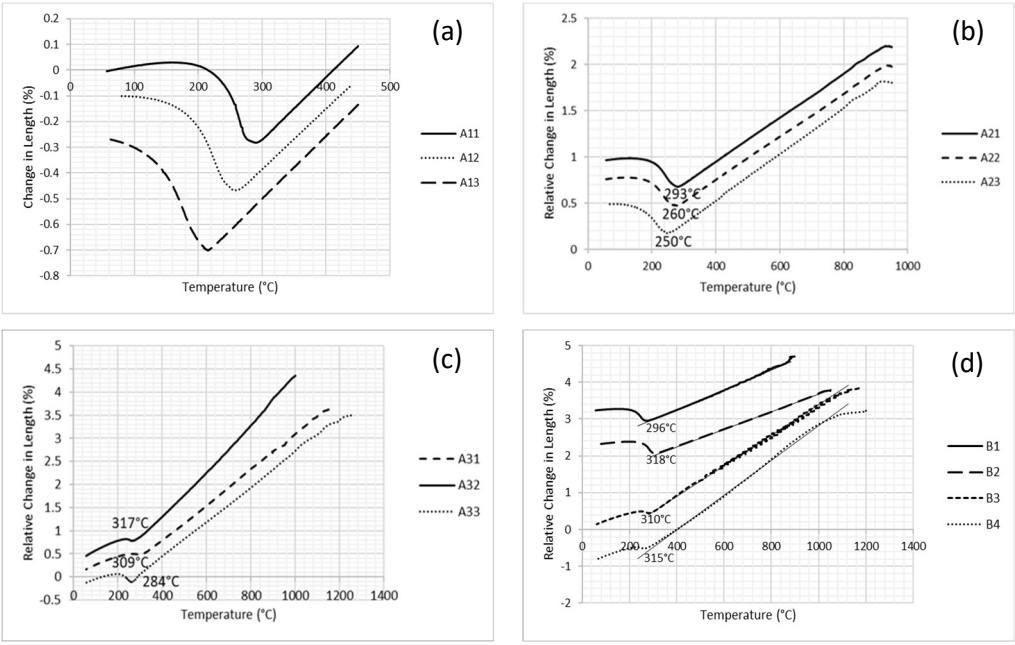

Figure 5-3: Relative change in length vs. temperature during quenching for (a) Group A1, (b) group A2 and A3, (c) group B, (d) A13-2, A4, B5 alloys.

5.3.1. Shortcomings of the available thermodynamic simulation techniques

Throughout the course of this research a number of discrepancies has been detected between the thermodynamic simulation results and the experimental ones. For well-established simulation programs it is expected to be able to accurately describe the behaviour of conventional alloys. However, the alloys designed under the scope of this research employ alloying strategies that are uncommon to the steel industry, Hence, inaccuracies as well as gaps in the present simulation tools are to be expected.

Figure 5-3 shows the microstructures of the A31, A32, B3 and B4 alloys at different austenitization temperatures. α is present in the microstructure at temperatures up to 200 °C above those theoretically calculated by ThermoCalc. A representation of this

temperature deviation is provided in **Figure 5-4** for the A31 and A32 alloys (a) and the B4 alloy (b). The TCFE9 database used in ThermoCalc is claimed to allow for aluminium additions of up to 10 wt.%. However, the experimental results demonstrate that the database's accuracy drops in some of the alloys investigated, which only have aluminium contents of 3 – 5 wt.%. The extent of the discrepancies between the theoretical and the experimental results is that some of the alloys designed specifically to avoid the γ loop (A31 and B4) could not be fully austenitized, due to existing in the α – γ region of the phase diagram. **Figure 5-4 (b)** shows the change in ferrite volume fraction with changing the austenitizing temperature for alloy B4, indicating that the ferrite volume fraction drops to a minimum of about 12 vol.% at 1200 °C, then increase to 18 vol.% at 1300 °C, and further proving the absence of a region where the alloy could be fully austenitized.

A number of results should be considered when assessing the observed shortcomings of the TCFE9 database. Alloy A4, with 5 wt.% Al, could be fully austenitized at a temperature of about only 100 °C above the theoretically calculated one. While A32 and A33, also with an Al content of 5 wt.% but with lower C, could only be fully austenitized at temperatures much higher than those theoretically determined. In addition to that, alloy A31, also with 5 wt.% Al was not fully austenitizeable. Moreover, a similar discrepancy in temperatures is found in the alloys B3 and B4, containing only 3 wt.% Al but with a much lower C-content of 0.31 and 0.23 wt.%, respectively. These trends imply that a more complex relationship governs the difference between the experimental and theoretical temperatures and the alloy composition. The inaccuracy of the TCFE9 database might be more dependent on the alloy hardenability than its aluminium content, increasing with its decrease.

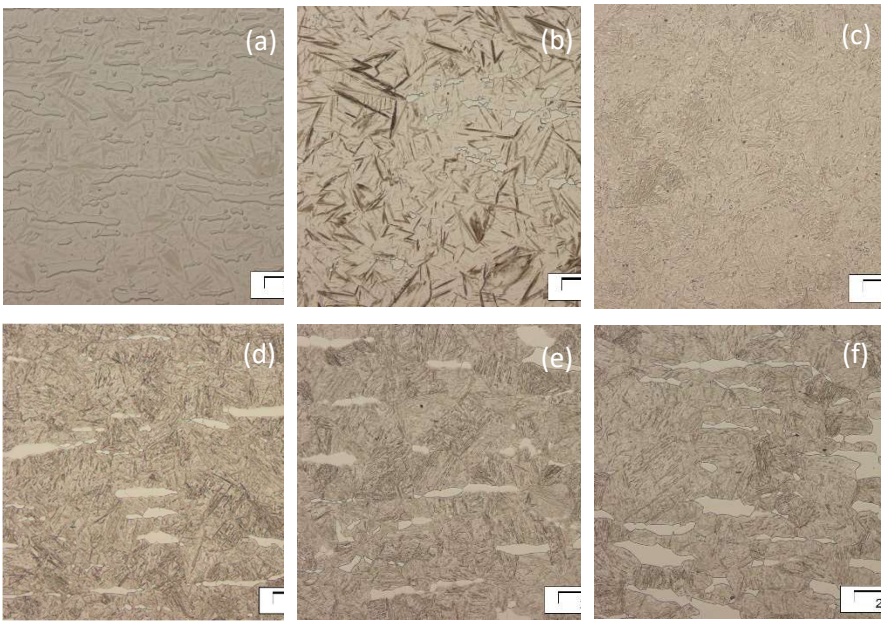

Figure 5-4: LOM images of quenched alloys (a) A31 from 1150 °C, (b) A32 from 1050 °C, (c) B3 from 1000 °C, (d) B4 from 1150 °C, (e) B4 from 1200 °C, (f) B4 from 1300 °C.

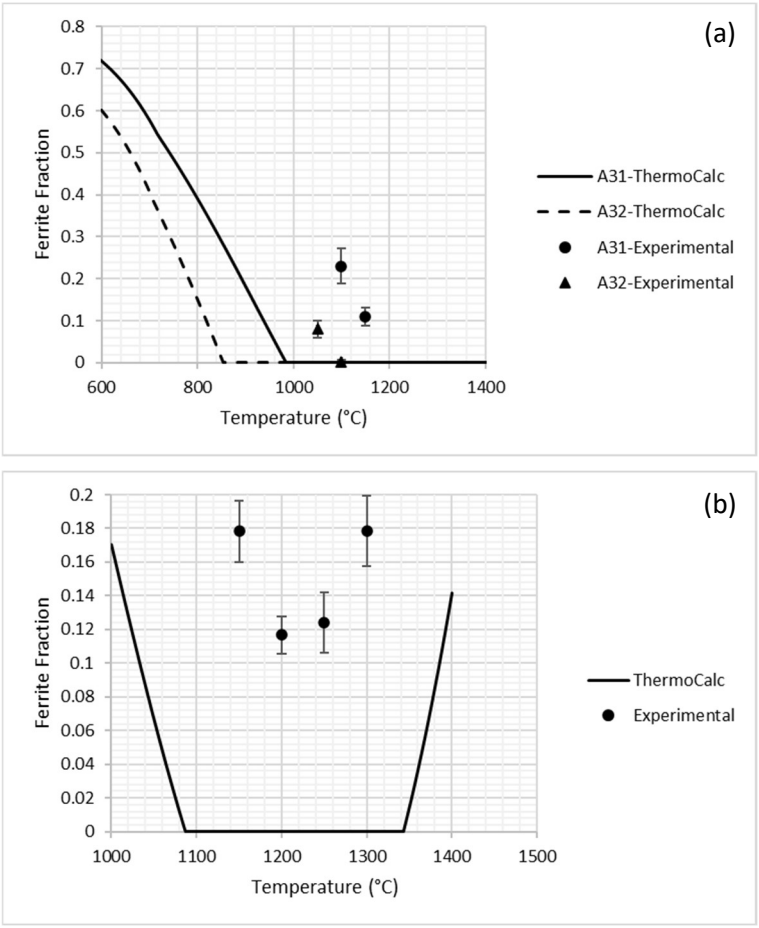

Figure 5-5: ThermoCalc simulated vs experimentally obtained ferrite fraction at different austenitization temperatures for (a) A31 and A32, (b) B4.

The effect of δ-ferrite on the properties of a nB microstructure has not been investigated in the present literature. Hence, specimens from the A31 and B4 alloys were austenitized at temperatures that would generate an approximate amount of 10 and 12 vol.% δ-ferrite (for A31 and B4, respectively) before austempering. As can be seen in **Figure 5-1**, the microstructure of the A4 alloy contained a number of dark

features that were initially thought to be MnS, however, after EDX investigation (**Figure 5-5**, **Table 5-3**) were found to be graphite nodules.

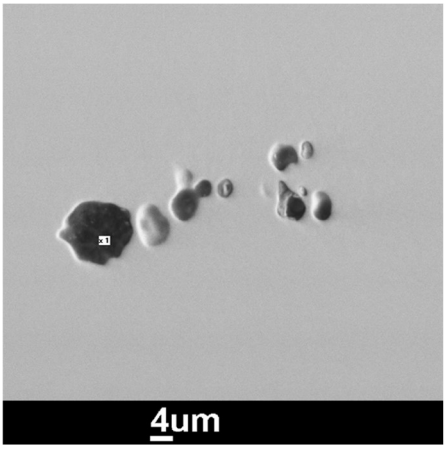

Figure 5-6: SEM micrograph of A4 showing graphite nodules.

Table 5-3: EDX analysis of a graphite nodule detected in A4.

Element	Amount (wt.%)	Amount (at.%)
Fe	5.93	1.37
Al	0.43	0.20
Si	0.36	0.16
C	86.21	92.56
O	7.08	5.70

As an element that serves the same role in suppressing cementite precipitation as Si, Al is also expected to have a similar effect encouraging graphite formation, a fact that is well reported in the cast iron literature [96–98]. The presence of graphite should, however, not be expected at C levels below the cast iron range, even for high Al contents of 5 wt.%. **Figure 5-6** shows a contour plot of the change in the graphite mass fraction with changing temperature and C content generated using ThermoCalc. Thermodynamic simulations show that only a negligible mass fraction of 0.01 graphite would form in all the studied alloys; this amount should remain unchanged as both the C and Al amounts are changed between the different alloys. While the simulations correctly predict the absence of graphite from the (A1-), (A2-) and (A3-) groups, the experimental results for alloy A4 indicate graphite formation. Additionally, the contour plots imply that the negligible amounts of graphite are expected to precipitate at temperatures below 600 °C, which, while thermodynamically possible, might be kinetically impossible.

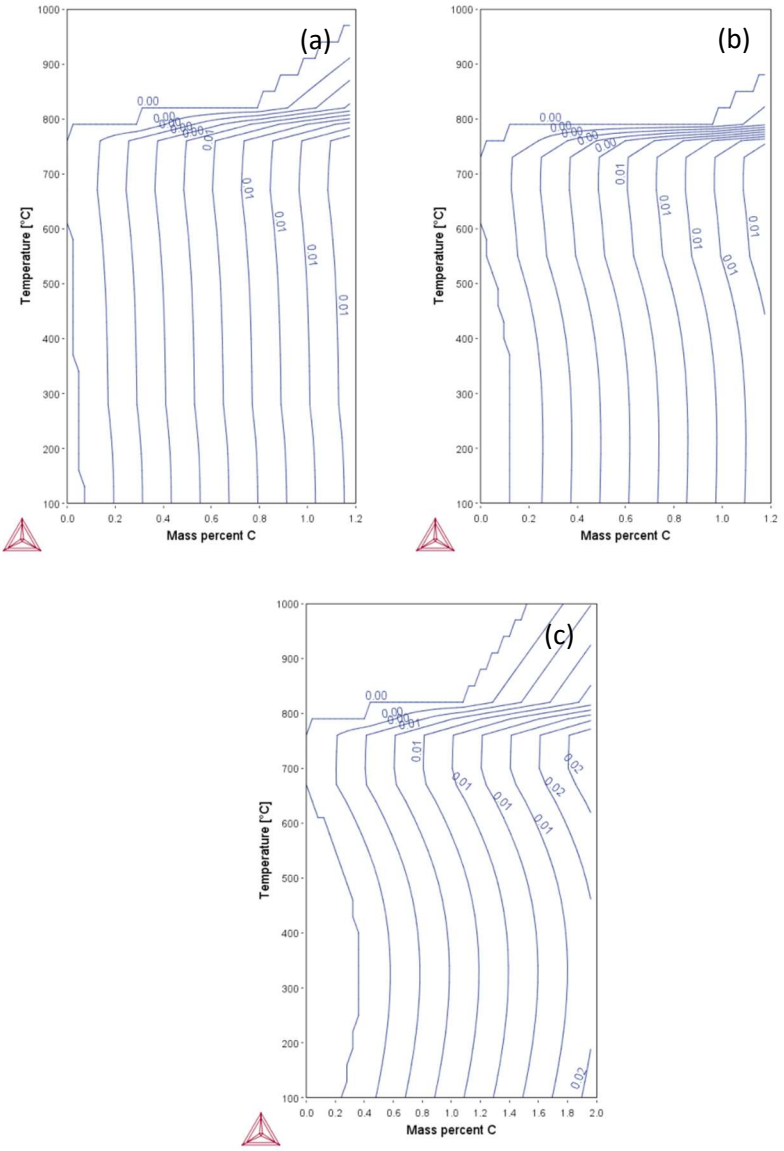

Figure 5-7: Contour diagrams for the change in graphite volume fraction with temperature and C content for (a) (A1-) system (1 wt.% Al), (b) (A2-) system (3 wt.% Al), (c) (A3/A4-) systems (5 wt.% Al).

On the other hand, the presence of graphite in the microstructure would explain the mechanical properties of the A4 alloy, which performed moderately well in terms of tensile strength while recording the lowest performance in terms of El% and impact properties as shown in **Figure 5-7**. Additionally, the presence of brittle, crack inducing particles in the microstructure would also cause the large deviation in the impact results for the specimens austempered at 310 °C.

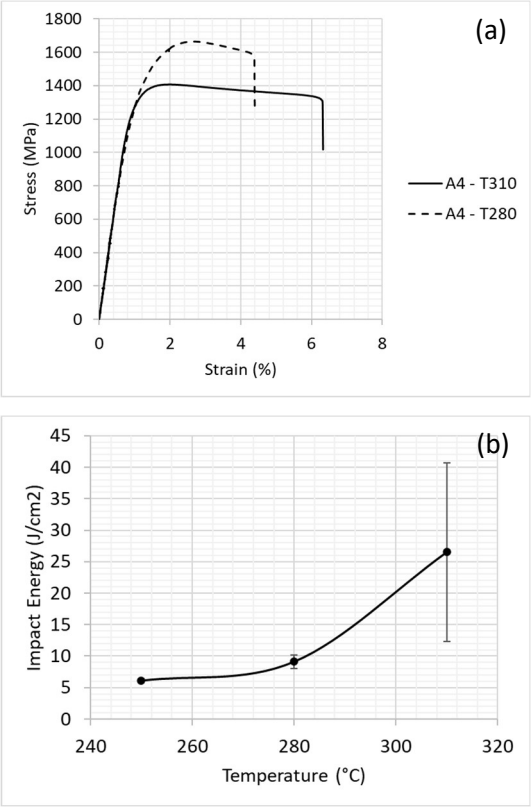

Figure 5-8: (a) Stress-strain diagram of the (A4-) alloy austempered at 310 and 280 °C, (b) change in impact energy vs austempering temperature for alloy (A4-).

5.4. Bainite transformation

5.4.1. High carbon, (A-) group, variants

Relative change in length with time curves for the (A-) group alloys are shown in **Figure 5-8**. The fastest transforming alloy in the (A-) group, as well as all the alloy groups studied is alloy A11 with a transformation time of 650 s at 310 °C. This is even faster than for the alloys transformed at 350 °C. In addition to the fast transformation time, a brief incubation period of about 10 s was recorded for this alloy as illustrated in **Figure 5-8 (a)**. A combination of low C content (0.54 wt.%) and low Mn content (0.29 wt.%) in addition to 1 wt.% Al yielded rapid transformation kinetics. On the other hand, the acceleration strategy of both low C and Mn yielded a high Ms, limiting the transformation temperature to only 310 °C. This negatively affects the maximum attainable mechanical properties as will be seen in the following section. As the C content is increased to 0.67 and 0.8 wt.%, the Ms decreases to 265 and 225 °C, respectively. However, as the C content increases, the incubation period increases to about 100 s, while the transformation time at 310 °C increases to 900 and 1700 s for alloys A12 and A13, respectively. Maximum transformation times required for each alloy were 2200 s for A12 at 280 °C and 6800 s for A13 at 235 °C.

The performance of the 3 wt.% Al (A2-) group is only slightly better compared to that of the (A1-) group. The lowest transformation time was recorded for A21 (0.77 wt.% C), requiring 1200 s and 1600 s to finish the transformation at 310 and 295 °C, respectively. However, the incubation period for A21 was similar to that of A13 at a value of about 100 s. Increasing C to 0.84 and 0.94 wt.% increases the incubation period to 200 – 300 s for A22 and 300 – 500 s for A23 and causes the transformation time at 310 °C to increase to 1800 s and 2200 s, respectively. The higher C content of the A22 and A23 alloys enabled their austempering at temperatures as low as 265 °C but increased the transformation times to 3200 s for alloy A22 and 4600 s for

A23. The performance of this group can only be gauged by comparing the performances of the alloys A13 and A22, both having similar C contents of approx. 0.8 wt.%. As evident from **Figure 5-8 (h)**, A22 required a slightly faster transformation time than A13, only a small improvement is achieved because of the increase in Mn, from 0.3 wt.% in the (A1-) group to 1.0 wt.% in the (A2-) group, which retards the bainitic transformation.

Further increasing the Al to about 5 wt.% is expected to accelerate the bainitic transformation time. The incubation period for the (A3-) group drops back to about 10 – 20 s as presented in **Figure 5-8 (g)**. However, the high Ms temperatures of the alloys A31 and A32 limit their austempering temperature to 350 °C. The fastest transforming alloy at 350 °C was A21 with a transformation time of 750 s. A31 and A32 recorded transformation times of 1000 s and 1200 s, respectively, which were comparable to the lower Al and higher C A22 alloy with a transformation time of 1200 s. Alloy A33, however, yielded a significant reduction in transformation time. From **Figure 5-8 (h)** it is apparent that the performance of A33 lies between that of A12 and A13, even though the C content of A33 is higher by about 0.1-0.2 wt.%. When comparing the transformation times of the (A3-) group at 350 °C, it is apparent that the change in C content, as well as the presence of δ-ferrite in the A31 alloy, have only a minor effect on the transformation times. At an austempering temperature of 350 °C, A31 with 10 vol.% δ-ferrite in the microstructure finishes the transformation after 1000 s, while both, A32 and A33, require around 1200 s to finish the bainitic transformation. The small differences in transformation times could be attributed to a combination of high Al content as well as high transformation temperature. Those two factors lead to a significant acceleration in bainite transformation kinetics, lowering it down to the order of 1000 s, at which differences in transformation times between the different alloys would be in the order of a few hundred seconds, which is not expected to be accurately detectable by the methods employed.

Increasing the Al content from 1 to 5 wt.% resulted in a drop in hardenability and an increase in the Ms requiring an increase in both, Mn and C, to partly counteract that effect. The added Mn reduced the accelerating effect of Al in group (A2-), leading to only a small reduction in transformation time and no change in the incubation period over the (A1-) group alloys of comparable C contents. Conversely, further increasing the Al beyond 3 wt.%, as in the case of A33, was sufficient to outperform A1 and A2 alloys with lower C and Mn contents in terms of transformation time as well as lowering the incubation period back to the 10 – 20 s range. The reduction in transformation time with increased Al content is presented in **Figure 5-9 (a)**. Additionally, **Figure 5-9 (b)** shows the change in transformation time at different austempering temperatures vs the C content of the alloy. The transformation time seems to decrease quite linearly with decreasing C content, however, A33 clearly recorded transformation times faster than those ones suggested by the linear trend, implying the success of the alloying strategy employed in accelerating the transformation kinetics.

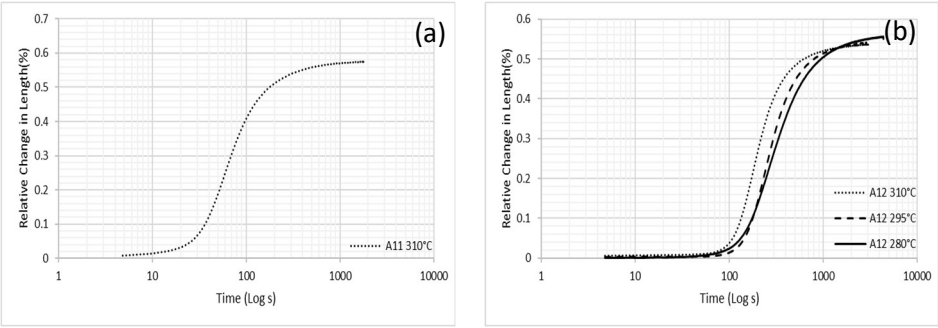

Figure 5-9 A: Dilatometric relative change in length vs time curves during austempering for alloys (a) A11, (b) A12.

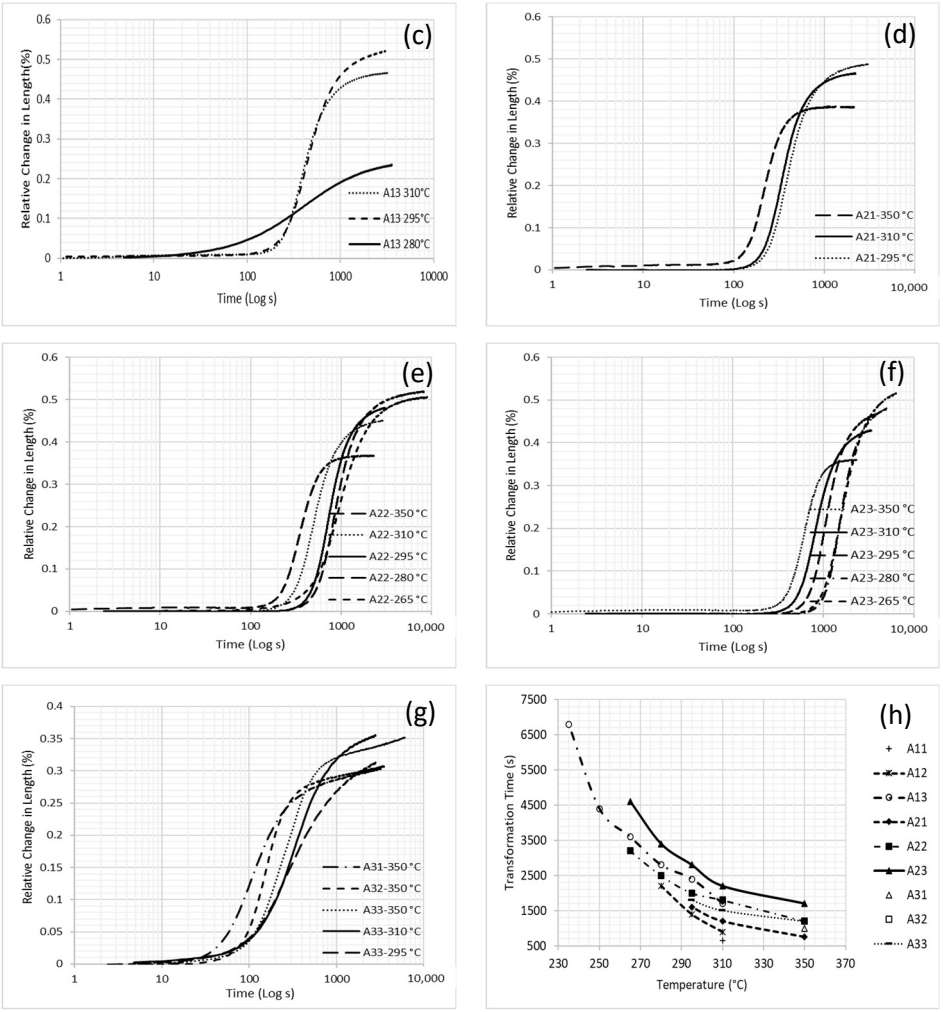

Figure 5-10 B: Dilatometric relative change in length vs time curves during austempering for alloys (c) A13, (d) A21, (e) A22, (f) A23, and (g) (A3-) group, (h) change in transformation time with austempering temperature for the (A-) group alloys.

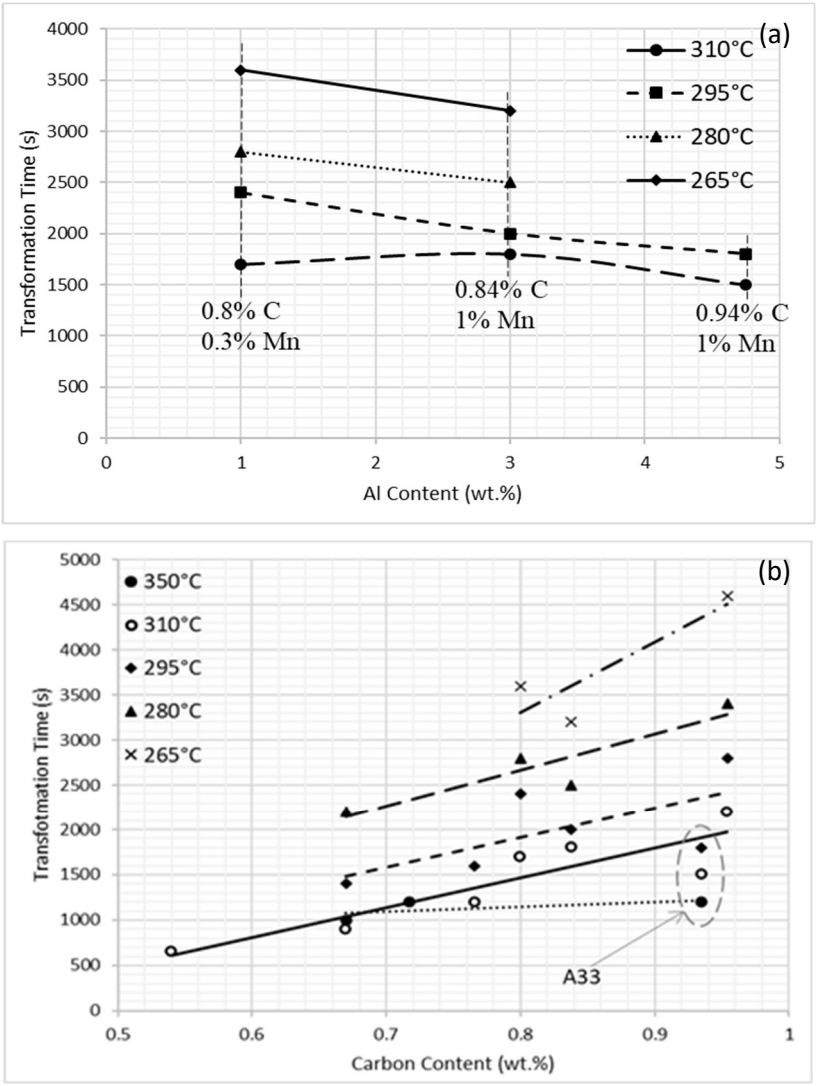

Figure 5-11: Transformation time vs (a) Al content, (b) C content for the (A-) group alloys.

5.4.2. Low carbon, (B-) group, variants

The dilatometric change in length vs. time curves for group (B-) are presented in **Figure 5-10 (a)**, the incubation periods for group (B-) are about 100 s for B1 and B4 and 40 s for B2, while the shortest incubation period was recorded by B3 at 10 s. **Figure 5-10 (b)** shows the change in transformation time with Al content for the 4 (B-) group alloys investigated. As the Al content is increased from 0.73 to 2.8 wt.% (alloys B1 to B3) the bainitic transformation time drops from 3000 s to 2000 s. On the other hand, both the B1 alloy, austempered at 310 °C, and B4, austempered at 350 °C, recorded a similar transformation time of 4000 s, which is the longest one for all the conditions tested. The low Al content in addition to a lower austempering temperature led to the slow transformation kinetics of alloy B1 at 310 °C. A number of factors influence the bainitic transformation time of B4 in comparison to the rest of the (B-) group alloys. In terms of its composition, B4 has the highest Al content of 3 wt.% and lowest C content of 0.22 wt.%, both would increase the stability of the ferrite phase at the expense of γ leading to an accelerated transformation. In addition, the presence of 12 vol.% δ-ferrite in the microstructure is believed to aid the nucleation of α_b. On the other hand, the presence 12 vol.% δ-ferrite is expected to cause some solute partitioning in the parent austenite. **Figure 5-10 (c)** indicate a negligible change in Al and Mn content and a marginal increase in C content as a result of the presence of δ-ferrite. Additionally, B4 has the highest Mn content of 4.17 wt.%, which has the opposite effect of stabilizing the γ and retarding the transformation. Considering the combination of aforementioned accelerating and retarding factors in B4, as well as the fact that it is the slowest transforming alloy in its group, these results imply that the retarding factors outweigh the accelerating ones, leading to an overall slower transformation kinetics.

Figure 5-11 shows the change in length vs time curves for the continuous cooling experiments performed on the alloys of the (B-) group. Three cooling rates (0.3, 0.03

and 0.003 $K.s^{-1}$) were investigated to determine the order of magnitude of the rate required for the transformation to finish. Determining whether the change in length observed is due to the bainitic or martensitic transformation is not straightforward. However, by correlating the isothermal transformation times presented in **Figure 5-10 (a)** with the duration of the transformation in Figures **5-11 (a-c)**, as well as the final microstructure in **Figures 5-11 (d-h)**, the nature of the transformation can be identified.

As illustrated in **Figures 5-11 (a-c)**, the specimens initially contract with reducing the temperature, which corresponds to the brief incubation period before the bainitic transformation begins. While this incubation period is undetectable when cooling at a rate of 0.003 $K.s^{-1}$, it takes up to a third of the cooling time at a rate of 0.3 $K.s^{-1}$. The dilatometry curves for continuous cooling at 0.3 $K.s^{-1}$ (**Figure 5-11 (a)**) imply a reaction that finishes after only a few hundred seconds, which can only be martensite, since the fastest isothermal transformation time recorded for a (B-) group alloy at 350 °C is 1500 s for B3. Experimental evidence for this is provided by the fully martensitic microstructures shown in **Figures 5-11 (d)** and **(e)** for this cooling rate. It is interesting to note a change in the nature of transformation noticeable in **Figure 5-11 (a)** for both the B2 and B3 alloys after around 400 s, implying that the bainitic transformation had initiated but did not finish before reaching the Ms. A similar trend could not be observed for B1 owing to its slower transformation kinetics, which caused the Ms to be reached during the incubation period for the bainite transformation.

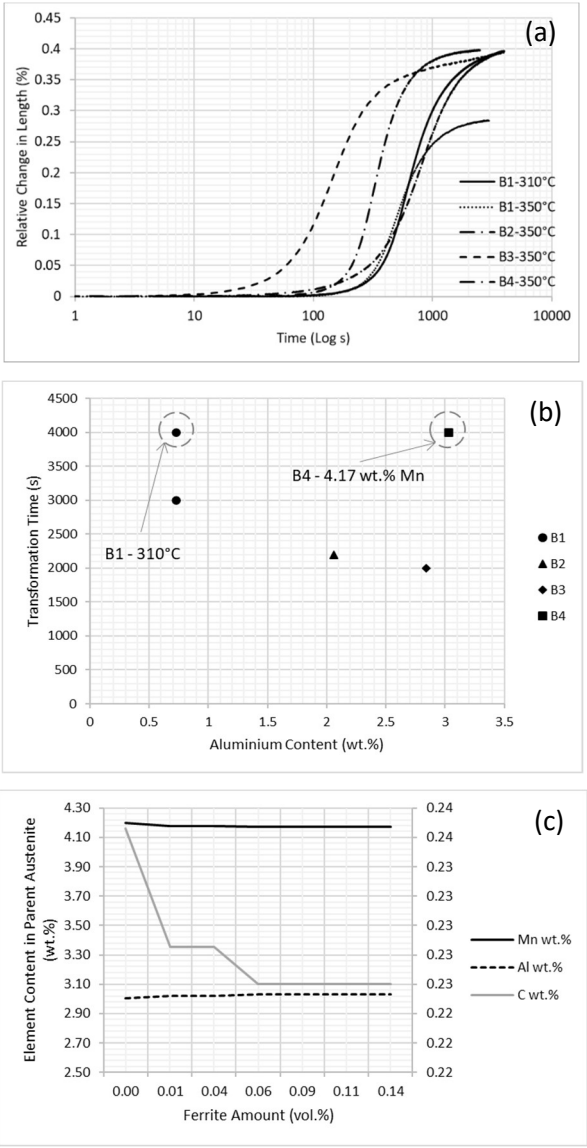

Figure 5-12: (a) Dilatometric relative change in length vs time curves during austempering for group (B-) alloys, (b) transformation time vs Al content for the (B-) group alloys , and (c) change in the contents of Mn, Al and C of the parent austenite with changing δ-ferrite volume fraction in alloy B4.

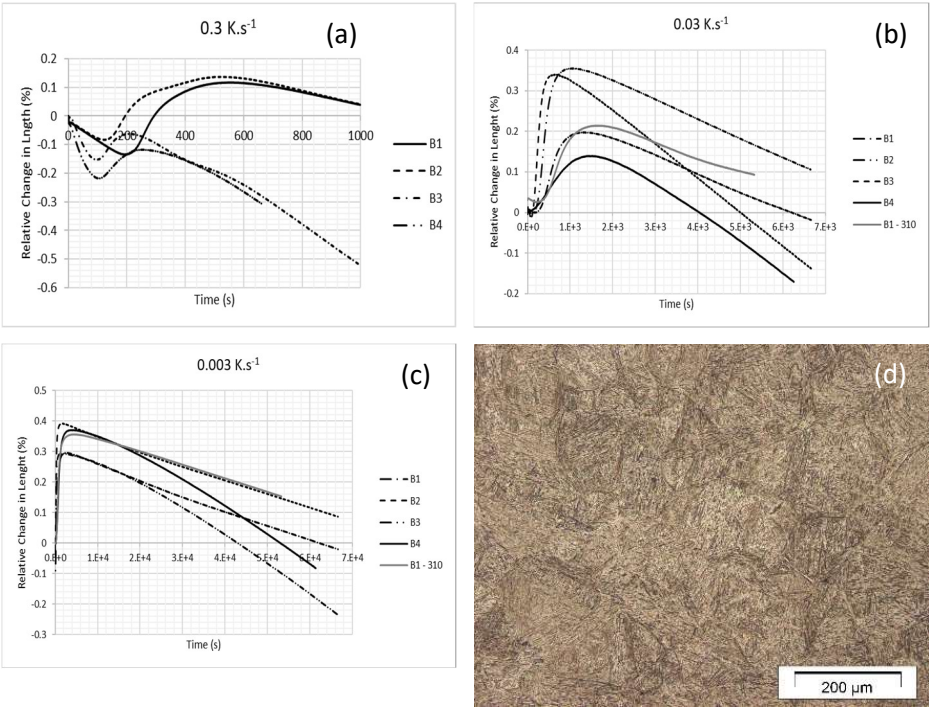

Figure 5-13 A: Dilatometric relative change in length vs time for (B-) group alloys continuously cooled at (a) 0.3 K.s-1, (b) 0.03 K.s-1, (c) 0.003 K.s-1, micrographs of (d) B1 continuously cooled at 0.3 K.s-1.

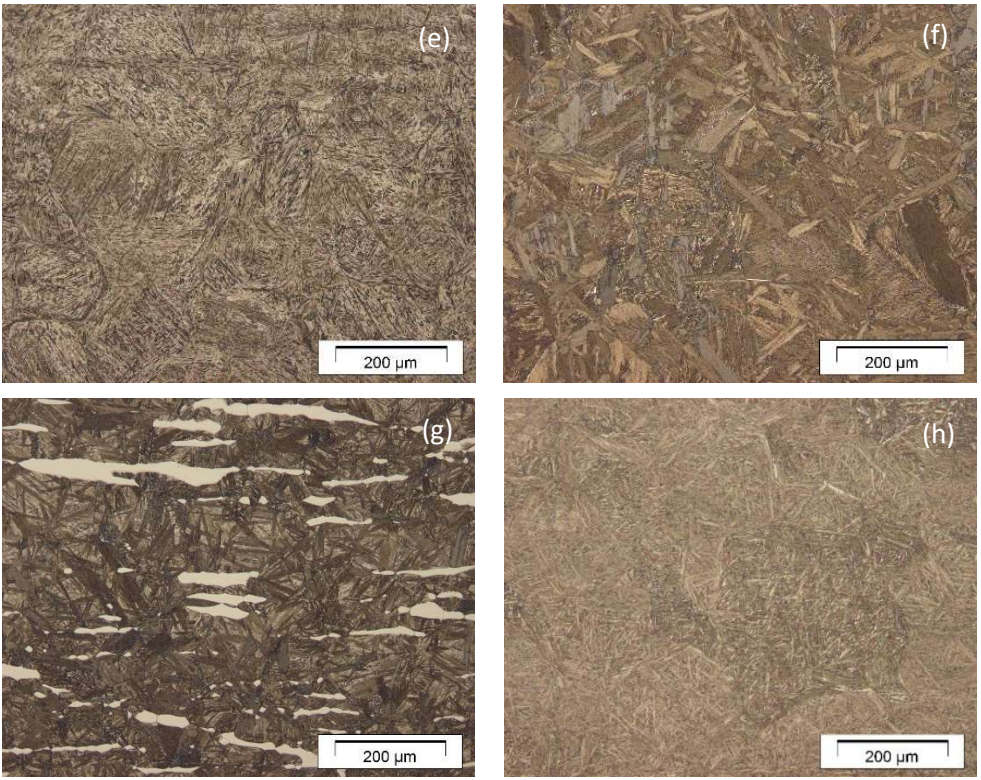

Figure 5-14 B: micrographs of (e) B2 continuously cooled at 0.3 K.s-1, (f) B3 continuously cooled at 0.03 K.s-1, (g) B4 continuously cooled at 0.03 K.s-1, (h) B1 quenched to 310 °C and continuously cooled at 0.003 K.s-1.

Lowering the cooling rate to 0.03 and 0.003 K.s-1 allows for sufficient time above the Ms for the bainitic transformation to proceed to completion. Dilation vs time curves, shown in **Figures 5-11 (b)** and **(c)**, indicate no change in the rate of cooling during the transformation. This is further supported by the microstructures presented in **Figures 5-11 (f-h)**, displaying bainitic microstructures similar to those ones obtained from isothermal holding.

5.5. Microstructure characterization

LOM was used to identify and quantify a number of microstructural features that are on a scale much larger than the bainitic lamellar thickness (which is unresolvable under LOM). LOM investigations were performed on all the transformed dilatometry specimens to determine whether α grains are present in the microstructure, to determine whether a microstructure is bainitic or martensitic (similar to **Figure 5-11 (d-h)**), as well as to measure the volume percentage of δ-ferrite grains in the case of A31 and B4. Additionally, LOM was used to reveal the PAGs as presented in **Figure 5-12**. For the group (A-) alloys, austempering at 950 -1150 °C results in a PAGs of about 50 µm (40 – 60 µm), which further increases to about 250 µm as the austenitization temperature is increased to 1200 and 1250 °C. The PAGs results for group (B-) display a similar trend, with the PAGs increasing from about 100 µm at an austempering temperature of 1050 °C to 122 µm for B3 austempered at 1170 °C followed by a further drop to 89 µm in the case of B4 austempered at 1200 °C. It is evident from the PAGs values of A31 and B4 that the presence of δ-ferrite in the microstructure of these alloys resulted in a drop in PAGs to values similar to alloys austempered at much lower temperatures. Where A31 austempered at 1150 °C recorded a PAGs of 50 µm similar to the A2 group austempered at 950 °C, and B4 austempered at 1200 °C recorded a PAGS of 89 µm similar to B1 and B2 austempered at 1050 °C.

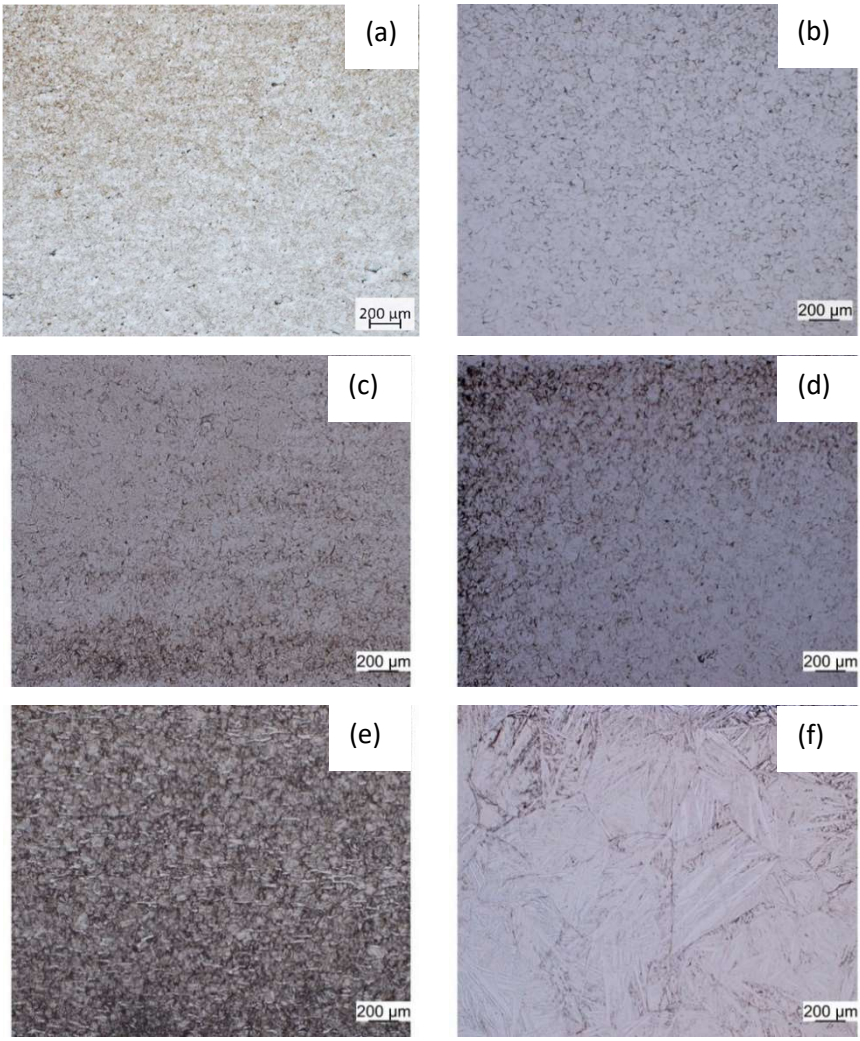

Figure 5-15 A: LOM micrographs of quenched dilatometry specimens showing prior austenite grains in (a) A13 (b) A21, (c) A22, (d) A23, (e) A31, (f) A32.

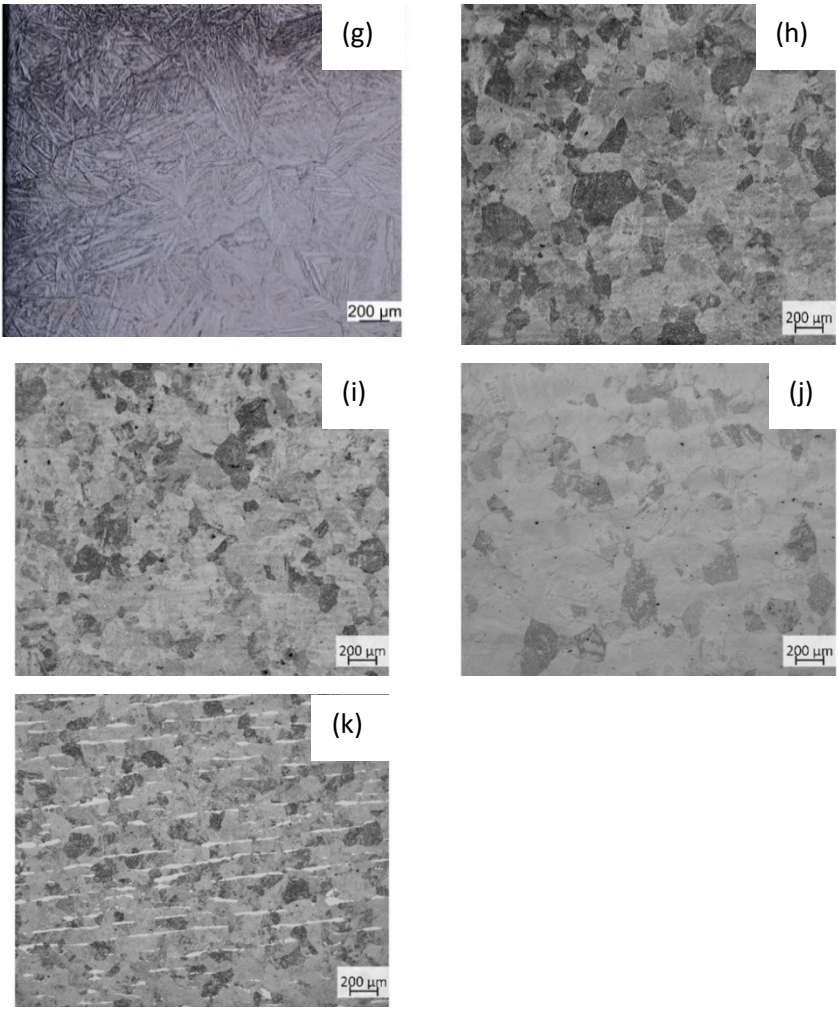

Figure 5 – 12 B: LOM micrographs of quenched dilatometry specimens showing prior austenite grains in (g) A33, (h) B1, (i) B2, (j) B3, (k) B4.

Scanning electron (SEM) and transmission electron microscopy (TEM) were essential to resolve the bainitic lamellae as well as measure their thicknesses. **Figure 5-13** shows the microstructures of selected alloys of the current investigation. All of

the alloys investigated illustrate the typical microstructure of a nB alloy, consisting of packets of bainitic lamellae sharing an orientation alternating with γ_r, as well as larger blocky γ grains. Large martensite grains could also be detected, which are caused by the low stability of a portion of the blocky γ, transforming to martensite during cooling.

TEM images presented in **Figure 5-14** further illustrate the fine lamellar structure of the nano-bainitic grains generated. Garcia-Mateo et al. report no difference between the bainitic lamellar thickness measurements obtained via SEM and TEM measurements [99]. Hence, the less expensive and more readily available SEM measurements were employed for lamellar thickness measurements in this research. On the other hand, the bainitic lamellae of the A13-2 specimens austempered at 250 °C could not be resolved using the SEM, thus, TEM measurements were used to determine their lamellar thicknesses, found to be 22 nm. Additionally, no non-metallic precipitates could be detected in the TEM investigations, confirming that no cementite precipitation had occurred and its successful inhibition by the alloying strategies investigated.

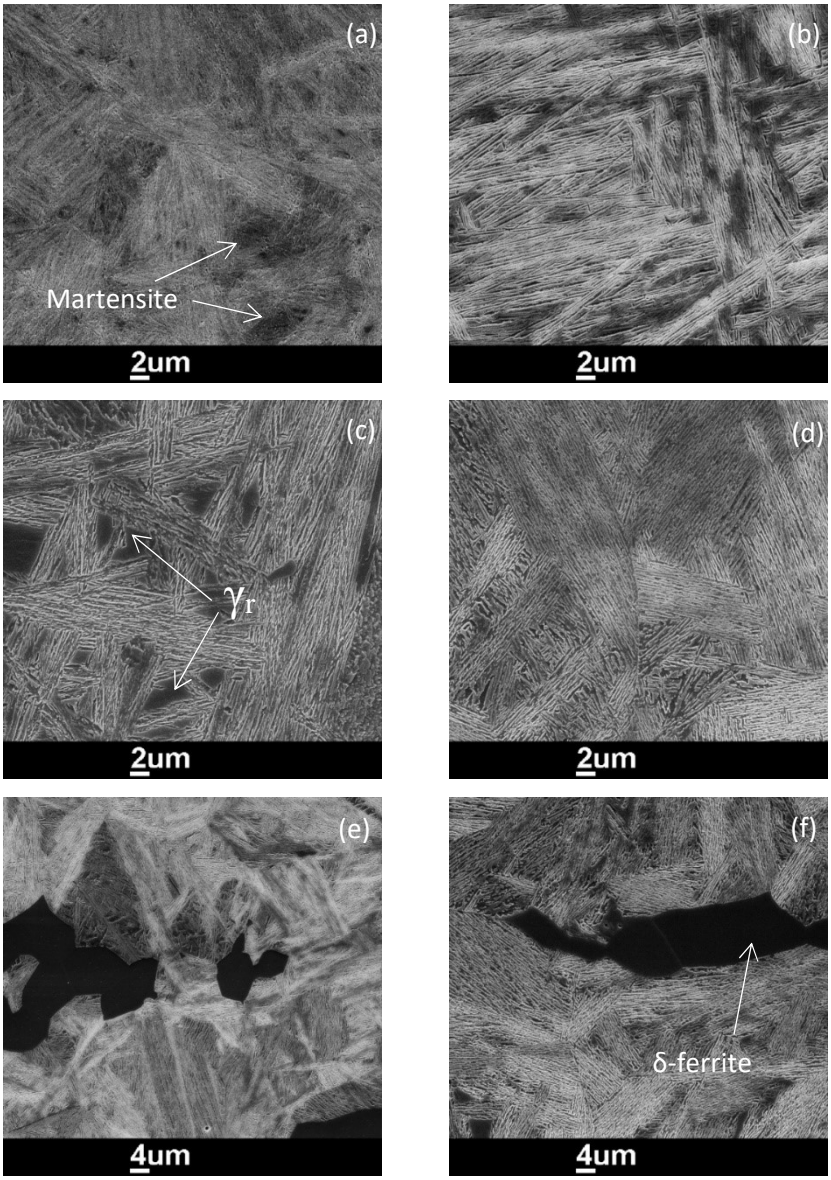

Figure 5-16: SEM micrographs of (a) A13-2 austempered at 250 °C, (b) A33 austempered at 350 °C, (c) B1 austempered at 350 °C, (d) B3 continuously cooled at 0.003 K.s-1, (e) A31 austempered at 350 °C, (f) B4 austempered at 350 °C.

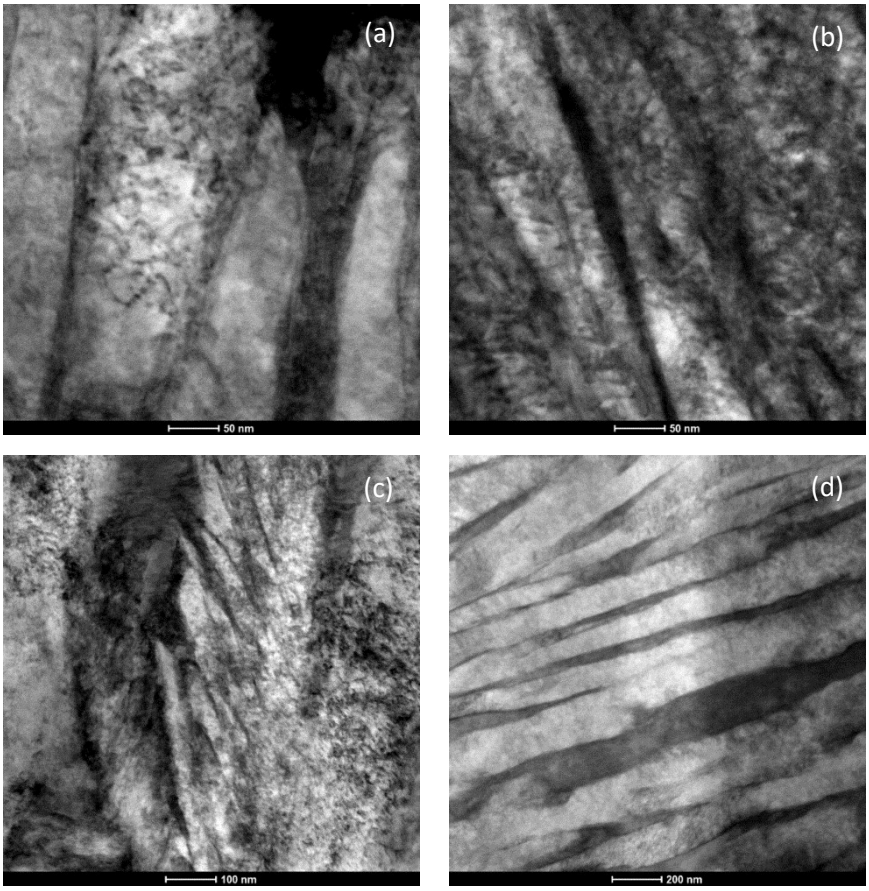

Figure 5-17: TEM micrographs of austempered (a) A33 at 310 °C, (b) A23 at 265 °C, (c) A13-2 at 250 °C, (d) B3 at 350 °C.

The change in bainitic lamellar thickness with alloy C content is displayed in **Figure 5-15**. A trend is illustrated whereby the lamellar thickness drops from 90 nm at 0.23 wt.% C (B4) to about 40 nm for the high C, (A-) group alloys, with no major change as the C content is increased beyond 0.7 wt.%. A number of factors govern the bainitic lamellar thickness, the most significant is the parent-γ strength, refining the

lamellar thickness with its increase. Another factor affecting the lamellar thickness is the driving force, also refining the lamellar thickness with its increase [12,100]. Increasing the C content is expected to strengthen the parent γ while lowering the driving force for bainite transformation, the trend illustrated in **Figure 5-15** implies that up to a C content of 0.7 wt.%, the effect on γ strengthening is the dominant one, leading to a refinement in lamellar thickness. However, the reduction in driving force associated with increasing the C content from 0.7 – 0.9 wt.% appears to become more significant, leading to the lamellar thickness remaining, more or less, constant at about 40 nm.

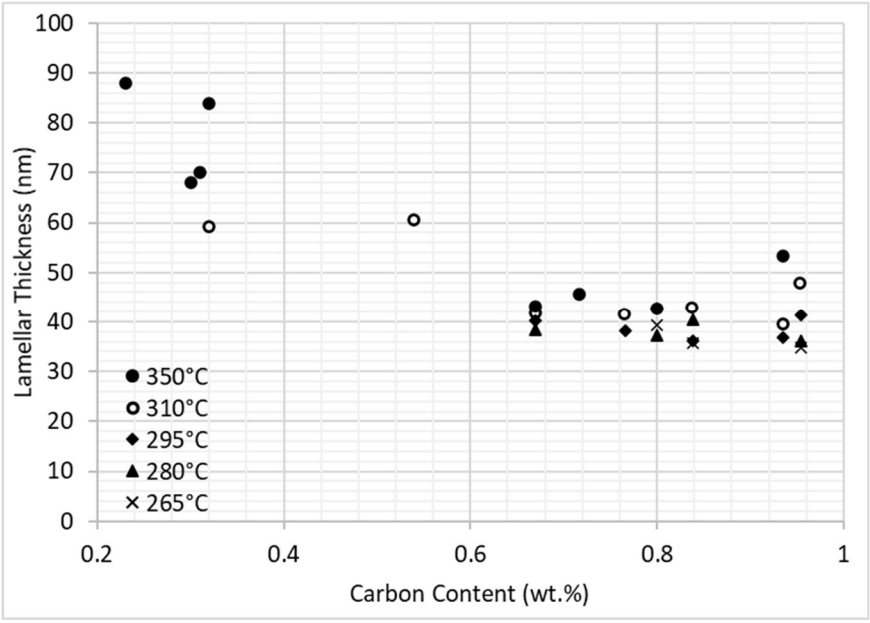

Figure 5-18: Bainitic lamellar thickness vs. carbon content for the alloys investigated.

5.5.1. X-ray diffraction

Figure 5-16 shows the synchrotron XRD patterns for selected alloys from the (A-) group. A qualitative analysis of the XRD patterns reveals that the amount of γ_r in the (A2-) and (A3-) groups is much more pronounced than those in the (A1-) group. A change in the amount of γ_r with changing austempering temperatures presented in **Figure 5-16 (d)** shows that the lowest amounts of γ_r were recorded for the (A1-) group, while the (A2-) and (A3-) groups recorded γ_r amounts comparable to those of the higher Mn, (B-) group alloys. The amount of γ retained in a nB microstructure is dependent on its stability. Elements such as C and Mn increase the γ stability and an increase in their amount is expected to lead to higher γ_r contents. While on the other hand, higher Al contents lower the stability of the γ grains, hence leading to a higher amount of it transforming to martensite during cooling. On the other hand, γ stabilizing elements shift the T_0 curve towards lower C contents, leading to a lower amount of α_b to be generated and, consequently, a higher amount of γ_r. The differences in γ_r amounts between the (A1-) group and the other alloy groups indicate a considerable effect of the alloy's Mn content on γ_r. However, whether group A1's low γ_r is due to a higher amount of α_b, or a lower stability of γ that transforms to martensite during cooling cannot be determined solely by the results of the XRD investigations.

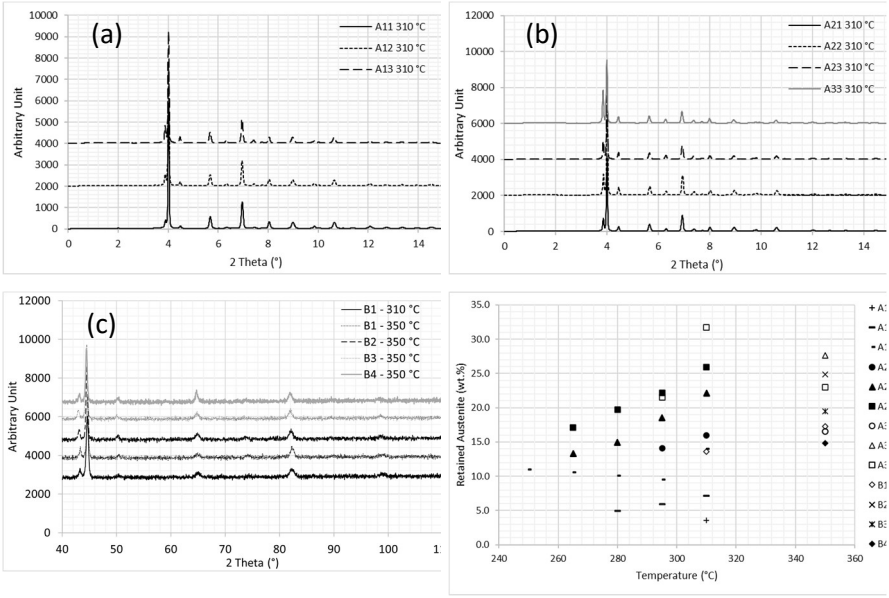

Figure 5-19: XRD diffraction patterns for (a) Select (A1-) group alloys, (b) Select (A2-) and (A3-) group alloys, (c) (B-) group alloys, and (d) variation of γr vs. austempering temperature.

5.5.2. T_0 curves and γ stability

As discussed in **Section 2.3.1**, the ductility of a nB microstructure relies on its γ_r content. However, for a positive contribution it has to be stable enough to neither transform into martensite during cooling to RT, nor at low levels of loading. A prominent metric for the stability of γ_r is its degree of enrichment with C. The extent of γ enrichment during the austempering process is determined by the T_0 curve (see **Section 2.2.1**), which is the locus of all the points of temperature where γ and α of the same C content have the same free energy, and thus, at which the bainitic transformation ceases. The position of the T_0 curve governs the final amount of α_b in the microstructure and is only affected by the substitutional alloying elements in the composition. Alloying elements such as Al shift the T_0 curve towards higher C

contents, enabling the enrichment of γ_r with more C and, consequently, enabling higher amounts of α_b to form. Additionally, this C enrichment results in a more stable γ_r at RT as well as more γ that can contribute to improve ductility via the TRIP mechanism.

Figure 5-17 shows the simulated T_0 curves using ThermoCalc for the alloy systems investigated, as well as Cγ for each of the austempered specimens determined via the XRD and Eq. 2. As the Al content increases from 1 wt.% in the (A1-) group to 3 wt.% in the (A2-) group the T_0 curve noticeably shifts towards higher C contents. The Cγ values determined from the XRD investigations appear to be, in most cases, higher than those ones predicted by the T_0 curve. This is commonly reported in literature and has been attributed by Bhadeshia and Edmonds to the differences in C contents between the C-rich film γ and the less stable blocky γ that is expected to transform to martensite upon cooling, skewing the Cγ results towards higher values [101]. As the Al content is increased to 5 wt.% in the (A3-) group, the simulated T_0 curve seems to shift back towards lower C contents. Contrary to the simulated results, however, the experimentally determined Cγ values indicate a higher C enrichment in A3 than in both the (A1-) and (A3-) groups. A similar trend can be observed for the (B-) group alloys, where T_0 shifts to higher C contents in B2 (2 wt.% Al) and then moves back to lower C contents for B3 and B4 (3 wt.% Al), while on the other hand, the Cγ results for B2, B3 and B4 are very similar, and all (B-) group Cγ results are at much higher values than those of the simulated T_0 curve, which is another trend to be found in both **Figures 5-17 (c)** and **(d)**.

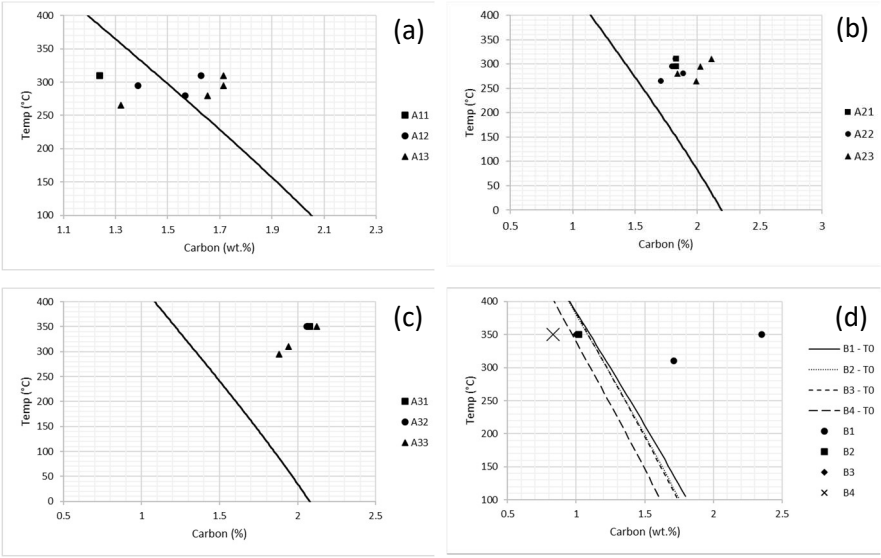

Figure 5-20: Simulated T0 curves (ThermoCalc) and XRD measured γr C contents for (a) (A1-) group, (b) (A2-) group, (c)(A3-) group and (d) (B-) group.

The ThermoCalc simulations presented in **Figure 5-17** imply that as the Al content is increased to 2-3 wt.% the T_0 curve shifts towards higher C content. Further increases in Al shifts the curve back towards lower C amounts. The experimental results, however, deviate – in some cases – from the simulated trends. A number of factors need to be considered to explain these deviations. The experimental values for group (A-) imply a continued increase in Cγ with Al content for all three alloy groups. Additionally, while groups A1 and A2 yielded similar Cγ values to those predicted by ThermoCalc, A3 recorded much higher values in comparison. Considering the inability of the ThermoCalc TCFE9 database to accurately predict the phase diagrams of the A3 group it could be argued that the database is simply underequipped to deal with similar alloys. Conversely, the Cγ values for group (B-) confirm the ThermoCalc simulation, with B1 recording the highest Cγ values and B2-B4 recording lower values, which are also closer to the predicted T_0 curves. The

results of group (B-) indicate that while ThermoCalc might not be capable of predicting the phase diagrams of high Al alloys, its prediction of the T_0 curves appear to be adequate.

To reconcile the discrepancy between the simulated T_0 curves and the experimental $C\gamma$ values for A3 it is important to consider the effects of Al on the stability of γ_r. The addition of Al would result in two opposing effects on γ_r stability. The first is the lowering of the chemical stability of γ leading to higher driving forces for the bainite transformation as well as higher Ms. The second effect is increasing the chemical stability of γ via shifting the T_0 curve towards higher C contents, resulting in a highly enriched γ that is more stable. The combination of the ThermoCalc predictions and the experimental findings suggest that as Al is increased from 1 – 5 wt. % the destabilizing effect of Al on the γ_r becomes more dominant. The results presented in **Figure 5-17** can be used to assess the γ_r stability of the alloys investigated. Bhadeshia and Edmonds reported that $C\gamma$ values much higher those predicted by the T_0 curves indicate lower stability γ_r with a higher amount of it transforming to martensite upon cooling [11]. Where a low γ_r value is not an indication of a higher volume fraction of α_b, but of a higher portion of unstable γ transforming to fresh martensite upon cooling, since the XRD measurements do not account for the difference between α_b and martensite. Conversely, $C\gamma$ values closer to those predicted by the T_0 imply higher stability γ_r and lower fresh martensite amounts. The results presented in **Figure 5-17** suggest that for Al additions up to 3 wt.%, as higher amount of bainitic ferrite forms (T_0 shifted to higher C contents) leading to γ_r enriched with more C, the stabilizing effect of the C enrichment outweighs the destabilizing effect of the Al addition. Contrary to that, as Al is increased to 5 wt.%, the effect of C enrichment is insufficient to counteract the effect of 5 wt. % Al on lowering the chemical stability of the γ_r. This analysis is further supported by the XRD data presented in **Figure 5-16 (d)**, where the γ_r amounts appear to increase with the increase of Al content from 1 to 3 wt.% followed by a

drop as the Al content is further increased to 5 wt.%. Additionally, these results also imply a negative effect of Al contents higher than 3 wt.% on the mechanical properties caused by a drop in γ stability which will be discussed further in **Section 5.6**.

For strain ageing experiments, the specimens are typically stored at temperatures of about -20 °C to slow down C diffusion. For this case the stability of γ at negative temperatures had to be considered. As evident from the SEM micrographs in **Section 5.5**, the presence of martensite could be detected in most of the microstructures generated. Martensite in a nB alloy is an indication of one of three situations. The first is that the transformation occurred below the Ms, as mentioned in **Section 2.4.3**. However, that was not the case in the current research. The second and third situations are concerned with the decomposition of γ into martensite during cooling due to either an unfinished transformation or the presence of blocky γ grains that cannot be sufficiently enriched with C to remain stable at RT. The viability of the transformation time determination method was discussed in **Section 4.3.2** and employed in this research, was experimentally verified as well as its effect on the martensite content in the microstructure and consequently, the mechanical properties of the austempered alloy.

Martensite formation during cooling can be detected by temperature vs relative change in length curves during cooling after austempering, **Figure 5-18** gives a representative cooling curve of the A13-2 alloy austempered at 310 °C for 4 h, depicting the Ms determination method covered in this section. The change in the slope of the curve indicates martensite formation with the temperature at which this change occurs indicating the stability of the blocky γ in the microstructure. Higher stability martensite is expected to have a lower Ms temperature. Comparing these Ms temperatures after different isothermal holding times at the same austempering temperature can be an indication for the reason of the martensite formation. If the

transformation is unfinished, the Ms will be lower the longer the austempering time is. On the other hand, if martensite formation is a matter of blocky γ size, composition and stability, the Ms will not change with changing the austempering time.

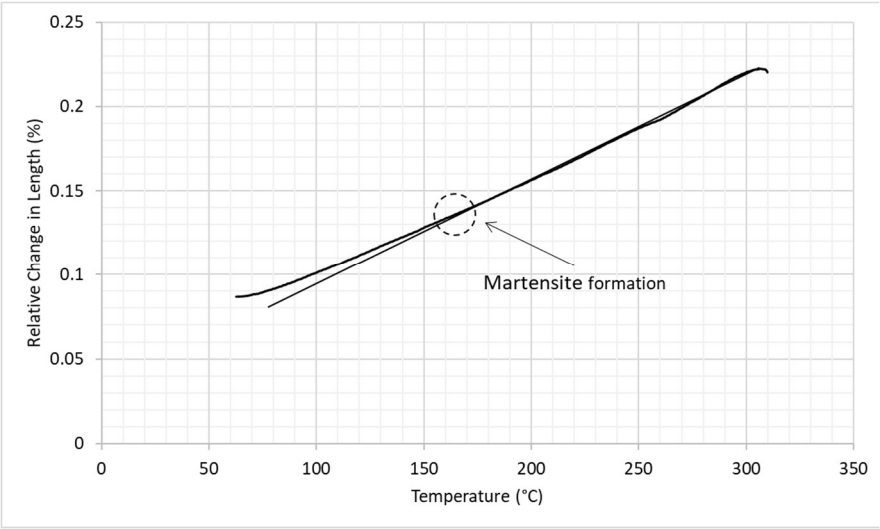

Figure 5-21: Relative change in length vs temperature during cooling for alloy A13-2, austempered for 4 h at 310 °C.

The aforementioned procedure was performed on dilatometric specimens sampled from alloy A13-2, the results are shown in **Table 5-4**. Austempering times of 2 ks, 4 ks and 6 ks indicate the time required for completion of the transformation at 310 °C, 280 °C and 250 °C, respectively, as presented in **Section 5.4**. An austempering time of 4 h was selected as a safe duration time ensuring the completion of the transformation for all alloys (maximum transformation time recorded was less than 3 h for A13 austempered at 235 °C, as well as not being long enough for cementite to precipitate. Moreover, an austempering time of 6 h was added for the lowest transformation temperature of 250 °C to investigate the effect of further prolonging

the austempering time on the stability of γ. It is evident from **Table 5-4** that there is a negligible change in the Ms values with changing austempering time, implying that the transformation time is not the main factor causing the transformation of blocky γ grains into martensite during cooling.

Table 5-4: Ms for A13-2, austempered at different temperatures and times.

	Ms (°C)		
Austempering Time	A13-2 – at 310°C	A13-2 – at 280°C	A13-2 – at 250°C
6h			124
4h	156	144	132
6ks			128
4ks		142	
2ks	158		

The γ stability depends on several factors, such as chemical stabilization via elements e.g. C and Mn, mechanical stabilization via increased dislocation density, and the γ grain size [102]. The alloying strategies employed in this research, while beneficial in accelerating the transformation, were inadequate in stabilizing the larger sized portions of the γ_r population. The SEM micrographs presented in **Figure 5-19 (a)** depict several populations of γ_r. The film γ benefits from chemical stabilization by C that partitioned into it during the bainitic transformation, as well as mechanical stabilization caused by the volume expansion of the α_b platelets surrounding it. On the other hand, the blocky γ lacks the conditions required for mechanical stabilization. Hence, chemical stabilization and grain size are the only factors governing its transformation into martensite. The condition of para-equilibrium necessitates that the blocky γ inherits the same nominal composition of substitutional alloying elements. While on the other hand, its C content is dependent

on the diffusion distance from the nearest transforming α_b, which is affected by the size of the γ grain in question. The different acceleration strategies studied rely on chemical compositions that increase the stability of α at the expense of that of the γ to accelerate the bainite transformation. A consequence of the aforementioned analysis is that the γ grains in the alloys studied rely solely on their grain size for stability on two levels. The first of which the grain size directly affects the transformation into martensite, in addition to a second indirect effect where the grain size influences C diffusion and consequently the chemical stability. Further evidence of this analysis is given with **Figure 5-19 (a)**, where martensite is clearly visible as resulting from larger prior γ grains, while the smaller blocky grains exhibit no clearly distinguishable evidence of martensite transformation. A similar effect of grain size on γ stability was reported by Lee et. al for TRIP steels [102].

Considering both the aforementioned γ stability analysis as well as the γ_r amounts measured via XRD experiments, a number of conclusions can be drawn concerning the effect of the alloying strategies on γ stability. The (A1-) group recorded the lowest γ_r amounts (**Figure 5-16 (d)**, 4 – 11 wt.%), implying the possibility that a portion of the γ_r transformed to martensite during cooling. On the other hand, difficulties clearly identifying martensite under both the LOM and SEM made it impossible to quantify the differences (or lack thereof) in martensite amounts between the different alloy groups.

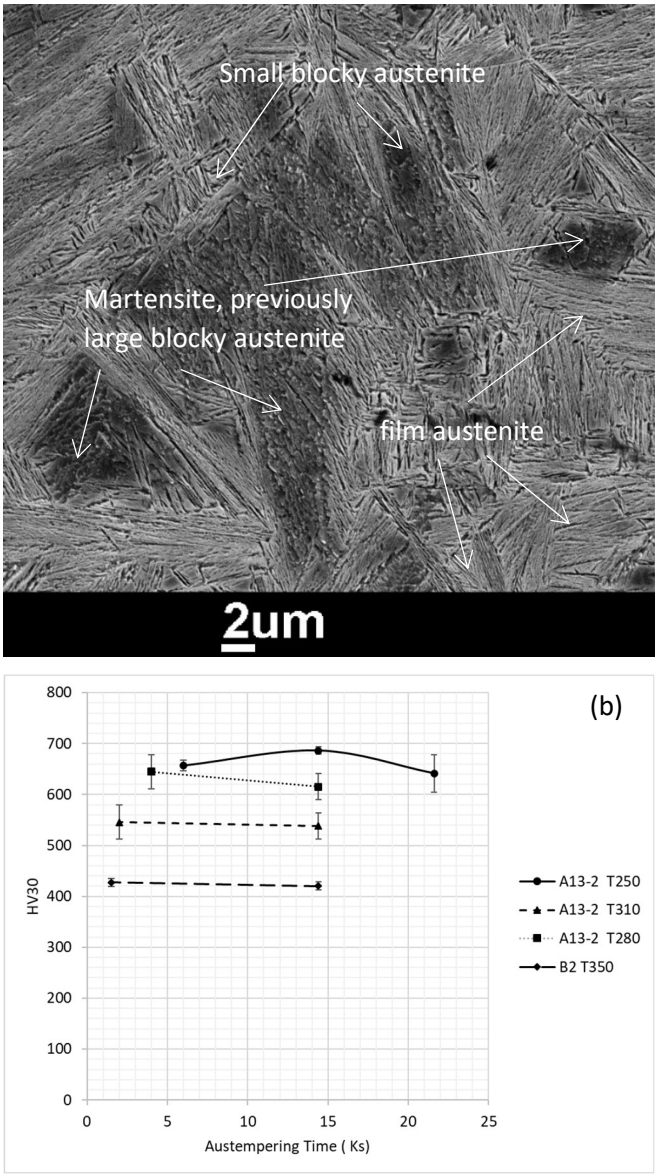

Figure 5-22: (a) SEM micrograph of alloy A13-2 after austempering for 2 ks at 310 °C, (b) change in hardness with austempering time for the A13-2 and B2 alloys.

Figure 5-19 (b) shows the difference in hardness between the specimens austempered for 4 h (and 6 h for A13-2 at 250 °C) and those that were quenched directly after the transformation was finished (according to the transformation criteria discussed in **Section 4.3.2**). A typical variation of hardness with austempering time would follow the following trend: Initially the hardness would be at a maximum, as most of the microstructure would transform to martensite during cooling. As the bainite transformation progresses, the hardness would drop with the formation of bainite, consequently enriching the γ. The hardness would reach a minimum when the transformation is finished, as most – if not all – of the microstructure would be αb and γr. This hardness value would remain constant up to the point where cementite precipitation begins, therewith starting with a further increase in hardness. Statistical analysis performed on the results displayed in **Figure 5-19 (b)** revealed that prolonging the austempering time up to 4 h had no significant difference on the hardness value. A conclusion from this analysis is that the transformation time determination criteria employed in this study was adequate, and that prolonging the isothermal holding time had no effect on further stabilizing the γr in the microstructure.

5.5.3. Effect of sub-zero temperatures on γ stability

It has become clear from the analysis performed in the previous section that the γ stability during cooling was a concern, hence, further cooling of the specimens below RT for storage for the strain ageing experiments could lead to more martensite formation, consequently adding an unwanted influence on the BH results.

Therefore, small pieces (10 mm x 10 mm) were cut from the rolled A13-2 samples, heat treated in a salt bath according to the procedure detailed in Chapter 4 and split into six groups. The first group was tested for its hardness immediately after cooling to RT, -5 °C and -20 °C. The second group was kept at the same three aforementioned temperatures for one week before hardness testing. The changes in

hardness were considered as indications of the martensite content of the microstructure.

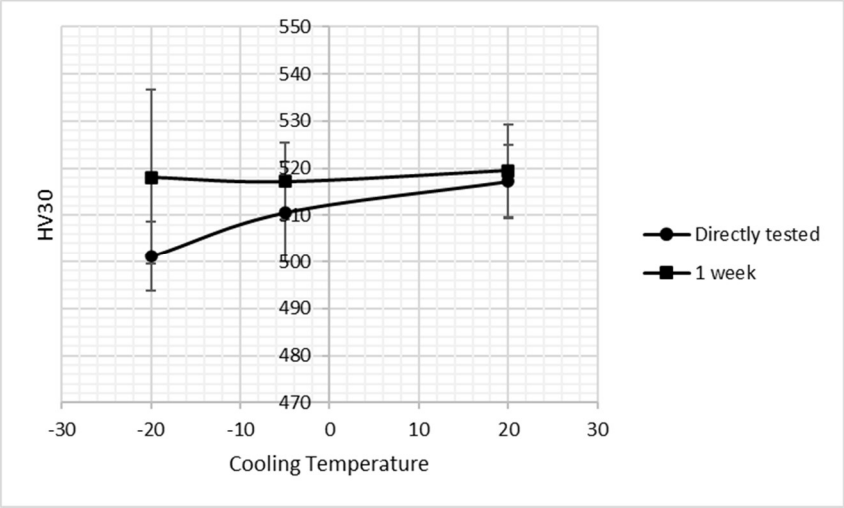

Figure 5-23: Hardness test results for A13-2 austempered at 310 °C after cooling to RT, -5 and -20 °C and directly testing or isothermal holding for 1 week.

Figure 5-20 shows an increasing gap as the temperature decreases between the hardness measured directly after austempering and the ones after storing for one week at the designated temperatures. Statistical analysis for all the conditions studied indicate that the only significant difference in hardness is between the specimen cooled to -20 °C and the one stored at -20°C for one week. This result implies the increase in martensite content with time at -20°C, which is in line with literature sources that report a transition in martensite formation from athermal to isothermal below a certain sub-zero temperature [103,104]. Since nB microstructures do not experience the effects of strain aging without pre-straining [16], and as a results of this investigation, while being mostly inconclusive, it was decided to avoid storing the BH test specimens, and instead plan the experiments so that the specimens are

tested directly after finishing the pre-straining and aging to avoid any effects that possible alterations to the microstructure due to low temperature storage could have on the experimental results.

5.6. Mechanical testing

5.6.1. High carbon, (A-) group, variants

Tensile strength results for the (A1-) group shown in **Figure 5-21 (a)** display the usual trend of nB steels, with a strength increase as the transformation temperature decreases. Increasing the C content has no direct effect on the strength of these nB alloys, with the only factor governing the strength being the lamellar thicknesses. The slightly higher strength of the A13 alloy at all austempering temperatures is however due to the indirect effect of the higher C content, increasing the strength of the parent γ grains which leads to refining the lamellar thickness.

The (A1-) group recorded the highest tensile strength values in this research, with values close to the upper limit of nB tensile strength recorded in literature. A11 exhibits a UTS of 1895 MPa at 310 °C, while the values of A13 range from 1910 MPa at 310 °C to 2140 MPa at 280 °C. A notable feat in this research is the ability to produce a nB alloy with a tensile strength of approximately 1900 MPa after an austempering time of only 10 min (A11, austempered at 310 °C), which is considered a significant improvement compared to the current literature. On the other hand, it was not possible to obtain tensile results for A13 from specimens austempered at temperatures below 280 °C owing to the high notch sensitivity of the microstructure causing the tensile specimens to fail at the radii near the grips. Brittle failure at the radii of the tensile specimens was observed to occur in both first and second castings of A13, as well as for the alloy B1. The three alloys in question have recorded the highest tensile strengths among all of the groups studied. This phenomenon was not only limited to the sub-size tension specimens, but also to the larger TTS820 flat

compression dilatometer specimens used to generate DIF (Deformation Induced Ferrite) in the B1 alloy and discussed more thoroughly in **Section 5.6.4**.

Tensile strength results of the (A2-) group, shown in **Figure 5-21 (a)**, display similar trends to those of the (A1-) group. An interesting observation is that alloy A21, the one with the lowest C content, recorded the highest tensile strength after austempering at 310 °C (1700 MPa), while the highest C alloy A23 recorded the least (1665 MPa). This is likely due to the higher amount of γ_r associated with a higher C alloy as discussed in **Section 5.5.2**. However, the difference in tensile strength between the alloys treated at the same austempering temperature is, as in the aforementioned case of the (A1-) group, minimal, as C does not directly affect the strength of nB alloys. High Ms temperatures of the alloys A31 and A32 limited their transformation temperature to 350 °C, hence, limiting their maximum attainable tensile strength. A31 and A32 recorded the lowest tensile strengths of the A-alloy family with 1330 MPa and 1465 MPa, respectively, implying a negative effect of the high Al amount on the tensile strength. On the other hand, A33 outperformed all the A2 alloys at the same transformation temperature in terms of tensile strength despite of a higher amount of γ_r than that of the (A2-) group alloys. Recording a UTS of 1735 MPa at a transformation temperature of 310 °C and 1845 MPa at a transformation temperature of 295 °C.

Tensile strength vs elongation values, presented in **Figure 5-21 (b),** indicate that for both of the (A1-) and (A2-) groups, the elongation values range about 10 %. Changes in tensile strength do not seem to have an effect on EL%. The values recorded for A1 and A2 are within the typically reported ranges for nB microstructures, which are listed in literature to be 5 – 30 % [16,35,36,105]. On the other hand, the (A3-) group significantly underperforms in terms of its elongation values, with A32 and A33 recording values of approx. only 5 %, which is considered to be the lower limit of the aforementioned reported range of EL% for nB alloys. However, due to the

presence of 10 vol.% δ-ferrite in the microstructure of A31, its ductility is improved by the presence of the soft phase up to 9.5 %, which is on par with the results obtained from the (A1-) and (A2-) groups.

Impact energy results of the (A-) group alloys are presented in **Figure 5-22**. The impact values range from 5 – 35 J/cm^2, which is in line with the range of values reported in literature for similar microstructures [16,35,36,105]. The impact energy drops with the decrease in austempering temperature, and there is a tendency for alloys with lower C content to record higher impact energy values than alloys of higher C content at the same austempering temperature. One notable exception for that trend is alloy A31, which recorded a significantly lower impact value than that of the higher C A32, which could be attributed to the presence of δ-ferrite in its microstructure. δ-ferrite is known to have an adverse effect on the impact properties of steel alloys due to its large, elongated morphology [106,107].

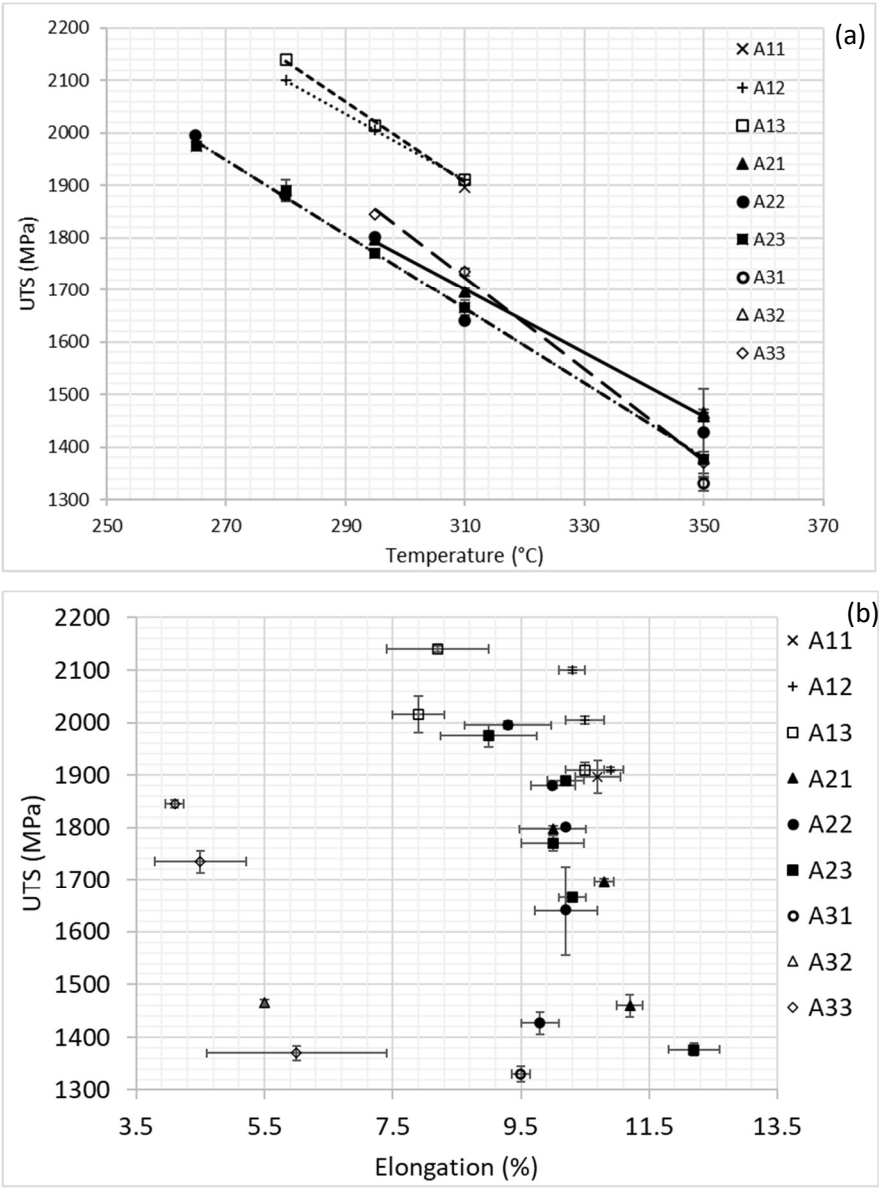

Figure 5-24: UTS vs (a) austempering temperature, (b) EL% for the (A-) group alloys.

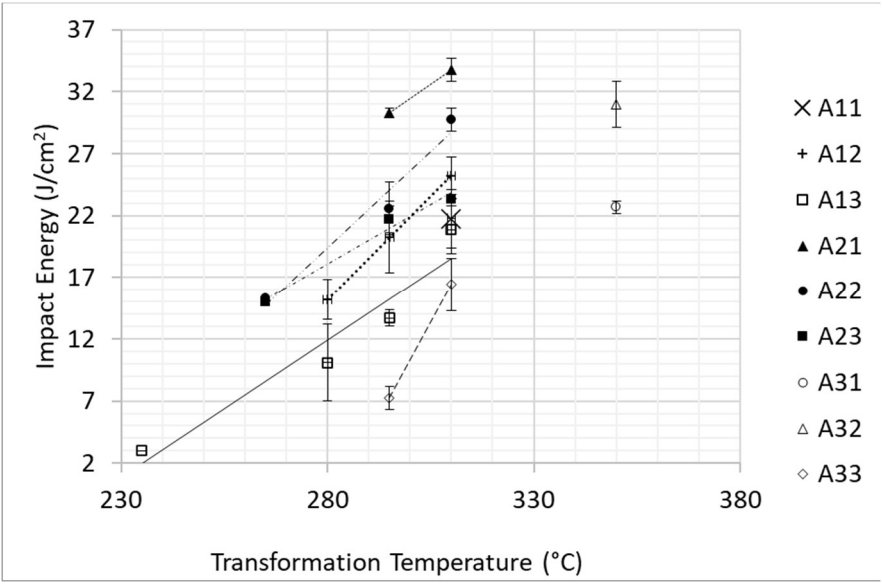

Figure 5-25: Impact energy vs transformation temperature for the (A-) group alloys.

5.6.2. Low carbon, (B-) Group, variants

The group B alloys with low C content were limited to higher austempering temperatures owing to their higher Ms temperature. High transformation temperatures led to significantly lower tensile strength values compared to those of the (A-) group. Tensile strengths (**Figure 5-23 (a)**) for the isothermally treated specimens ranged from 1500 MPa for B1 austempered at 310 °C, down to a minimum of 1100 MPa for B4 austempered at 350 °C and with 10 vol.% δ-ferrite in its microstructure. As the Al content is increased from 0.73 wt.% (B1) to 2.8 wt.% (B3), a slight drop in strength of 60 MPa was detected, which is in line with the previous trend, see **Section 5.6.1** for Al contents up to 3 wt.%. Additionally, elongation values still range around 10 % similar to those recorded for the (A-) group, with the exception of alloy B4 with the lowest C content, also containing δ-

ferrite, which recorded the highest elongation with 16 %. The higher EL% of B4, similarly to that of A31 discussed in **Section 5.6.1**, is a result of the presence of the soft and ductile δ-ferrite phase in the microstructure.

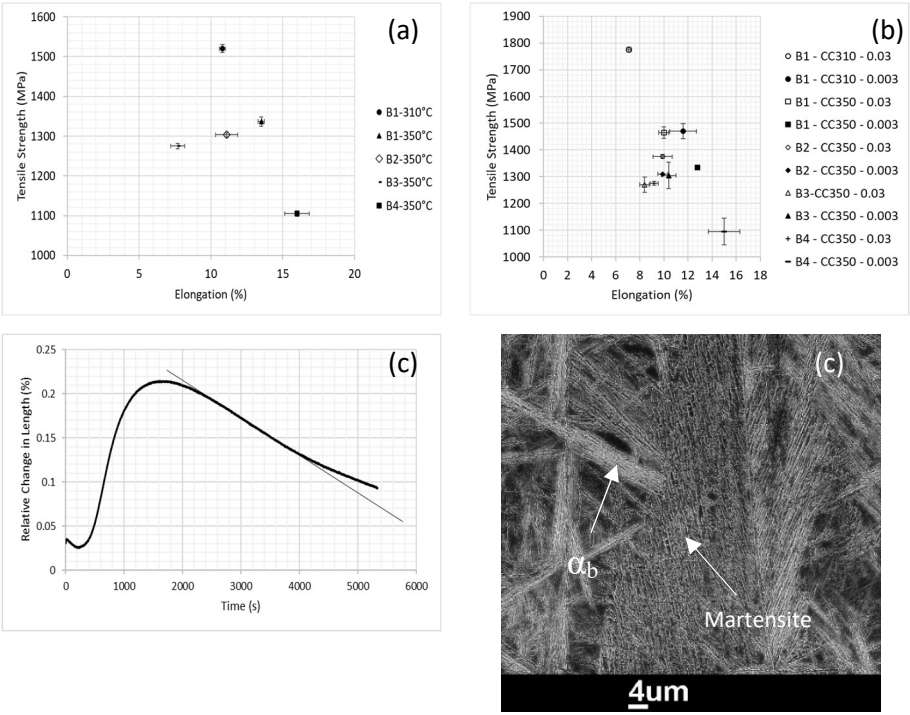

Figure 5-26: (a) Tensile strength vs EL% for the isothermally treated conditions, (b) tensile strength vs EL% for the continuously cooled conditions, (c) dilatometric relative change in length vs time curve for B1 quenched to 310 °C and continuously cooled at 0.03 K.s^{-1}, (d) SEM micrograph for B1 quenched to 310 °C and continuously cooled at 0.03 K.s^{-1}.

Continuous cooling yielded improved tensile test results for all of the conditions studied. **Figure 5-23 (b)** shows an increase in tensile strength of approx. 100 MPa for most specimens continuously cooled at a rate of 0.03 K.s^{-1} compared to the isothermally treated conditions. Conversely, no significant strength increase was

obtained by continuous cooling at a reduced rate of 0.003 $K.s^{-1}$. Continuous cooling is expected to refine the bainitic lamellar thickness via a continued lowering of both the transformation temperature and the Ms, as the transforming bainite enriches the γ with more C, enabling the bainitic transformation at continuously lowering temperatures. In case of the 0.003 $K.s^{-1}$ cooling rate, it allowed sufficient time for the transformation to finish near the starting temperature, as the drop in temperature from 350 °C to 340 °C required approximately 3300 s, while the slowest transforming alloys of group (B1 and B4) required around 4000 s to finish their bainitic transformation. Hence, no difference in results could be expected comparing to the isothermally treated condition. Nevertheless, the faster cooling rate of 0.03 $K.s^{-1}$ was fast enough to allow bainitic transformation at continuously lowering temperatures without hitting the Ms, and consequently, the improvement in the tensile strength was the result. On the other hand, the elongation values for the continuously cooled conditions remained comparable to those recorded by the isothermal conditions (approx. 10 % for B1-B3 and 16 % for B4). The only exception for that trend were the specimens of B1, quenched to 310 °C and then continuously cooled at 0.03 $K.s^{-1}$, scoring the low EL% value of 7.1 %. **Figure 5-23 (c)** shows the relative change in length vs time for B1 under these conditions. The clear increase in length towards the end of the transformation indicates martensite formation, which is also visible in the SEM (**Figure 5-23 (d)**). The presence of a considerable fraction of martensite in the microstructure would explain the significantly higher strength combined with a lower ductility.

Changes of impact energy values vs the Al content are provided in **Figure 5-24**. Both the isothermally treated as well as the continuously cooled conditions reveal the same trend, with an increase of the impact energy up to a maximum at an Al content of 2 wt.%. This increase is followed by a decrease as the Al content is increased further to 3 wt.%. The impact energy values are, however, still higher than those of the 0.73 wt.% Al specimens for the isothermally treated conditions, while

dropping to values similar to those of the 0.73 wt.% Al specimens for the continuously cooled ones. The lowest impact energy values are recorded for B4, both in the isothermally treated and the continuously cooled conditions. The large elongated morphology of the δ-ferrite grains coupled with the segregation of Mn atoms at the δ-ferrite – parent γ grain boundaries provides advancing cracks with large, weakened paths for its propagation, thus deteriorating the impact energy [108]. Another specimen that recorded low impact values was B1, continuously cooled at 0.03 $K.s^{-1}$ after quenching to 310 °C. The low impact values for this condition is due to the high amount of martensite in its microstructure, as previously discussed in this section.

5.6.3. Impact transition temperature

Alloying with a high content of Al is expected to deteriorate the impact transition properties of a steel alloy, shifting it towards higher temperatures [109]. Impact testing was performed over a range of temperatures from -160 °C to 50 °C to investigate the effect of the current alloying strategies on the impact transition. **Figure 5-25** illustrates that changing the Al content from 1 – 3 wt.% has no effect on the transition temperature for all the alloys studied (A13-2, B2 and B4) recording transition temperatures of about -10 °C. Both A13-2 and B4 recorded a low value of upper plateau energy at approx. 20 J/cm^2, with a lower plateau energy of only 1 and 2 J/cm^2, respectively. On the other hand, the performance of B2 presents a significant improvement compared to A13-2 and B4, with a lower plateau of 6 J/cm^2 and an impact energy value of 100 J/cm^2 at 50 °C (the upper plateau was not reached).

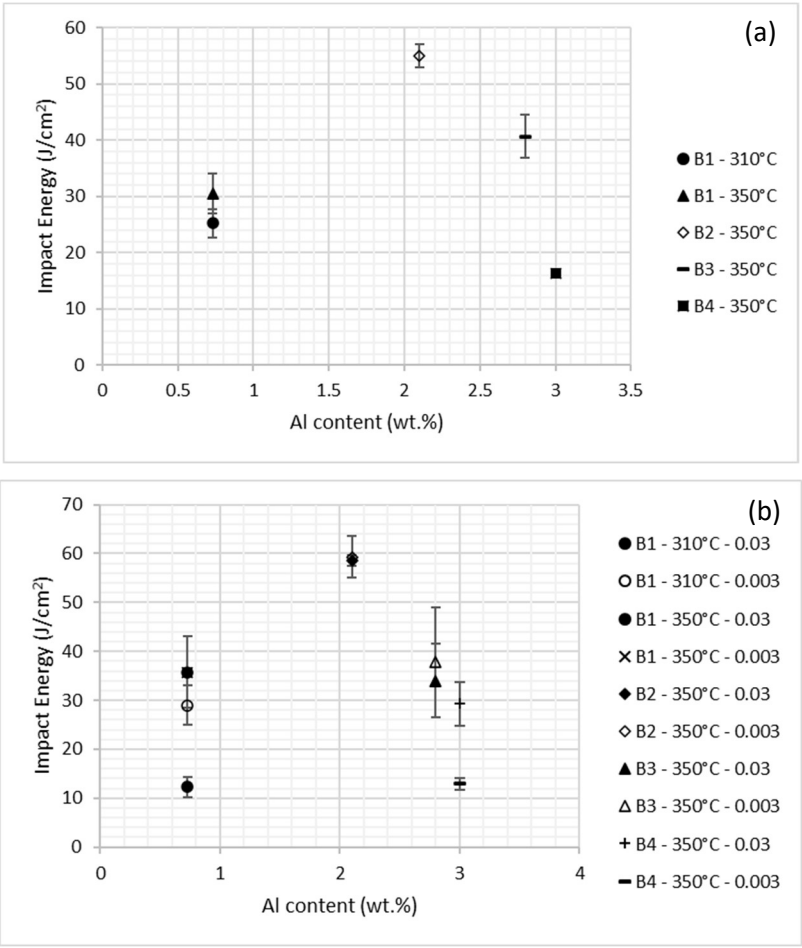

Figure 5-27: Impact energy vs Al content for (B-) group alloys after (a) isothermal treatment, (b) continuous cooling. Besides the alloy, starting temperature of cooling and cooling rate, if appropriate, is given.

Literature reports the main factor affecting the impact transition of displacive microstructures such as martensite and bainite as being the high angle boundaries of the prior γ grains [110,111]. This is dubbed the "effective grain size" and presents the smallest microstructural feature that has an effect on the impact properties. However, the experimental results presented in **Figure 5-25** contradict the

aforementioned literature, illustrating that A13-2 with an average prior γ gain size of about 40 µm and B2 and B4 with average prior γ grain sizes of about 97 and 90 µm, respectively, recorded similar impact transition temperatures. Sandvik and Nevalainen report that the impact properties of nB are dependent on both the effective grain size as well as the amount and morphology of the γ_r [112]. It is not implausible that the impact transition temperature would be dependent on a complex interaction between the effective grain size, the morphology of γ_r as well as its stability, however, the analysis undertaken in this work was insufficient to identify the details of such relationship.

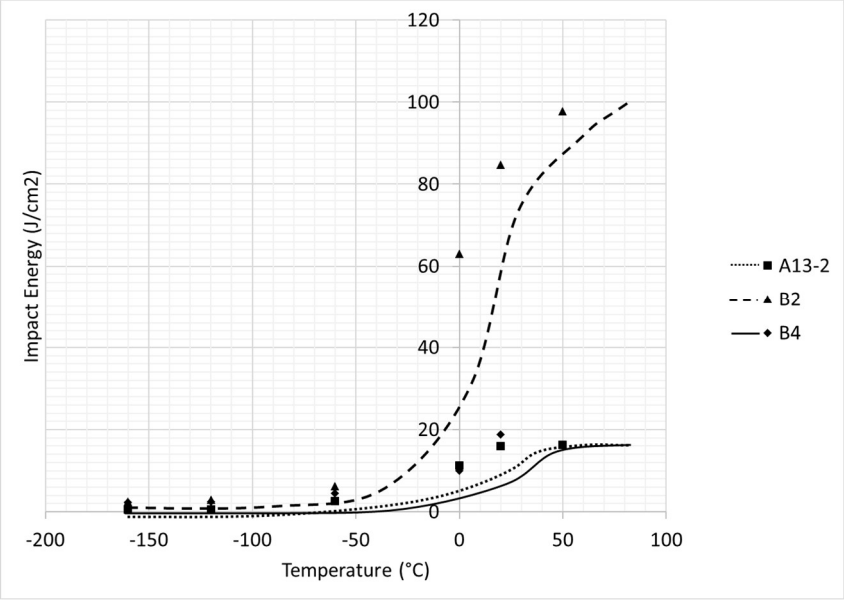

Figure 5-28: Change in impact energy with impact temperature for the A13-2, B2 and B4 alloys.

While B2 recorded relatively high impact energy values, those recorded for A13-2 and B4 were much lower. As previously mentioned in **Section 5.6.3**, the presence of large, elongated δ-ferrite grains in the microstructure of B4 are stated being the cause for its low impact energy values. Conversely, the low impact energy values of A13-

2, as compared to those of B2, can be attributed to a difference in the amount of γ_r in the microstructure. γ_r is expected to undergo strain induced transformation into martensite along the advancing crack tip, consuming more energy and improving the impact properties. However, for γ_r to be able to sufficiently dissipate energy in the aforementioned manner it must be adequately stable at room temperature. A C content of around 1 wt.% was reported by Jirkova et. al as the minimum required for γ_r to undergo strain induced transformation at adequate stress levels. However, it was also reported that C contents above 1.8 wt.% would lead to very stable γ_r that would not transform to martensite, thus not contributing to the deformation [113]. Additionally, the lower γ_r amount in A13-2 combined with a high Cγ is also an indication of a higher martensite content (as discussed in **Section 5.5**), the presence of which is expected to deteriorate the impact properties. Consequently, it seems plausible that a combination of lower amount of highly C-enriched and stable γ_r as well as more martensite content limited the ability of A13-2 to hindering crack propagation, thus leading to a much lower impact energy results when compared to B2.

5.6.4. Deformation induced ferrite transformation (DIFT)

Owing to the inaccuracies of the thermodynamic simulations (as discussed in **Section 5.3.1**), it was not possible to accurately target DIF generation temperatures, and a considerable amount of trial and error was required to locate the a_3 using the DIL805 deformation dilatometer. However, ThermoCalc simulated TTT diagrams (**Figure 5-26**), coupled with knowledge of the differences between the simulated and experimental a_3 temperatures were used to determine suitable DIF generation temperatures. The simulated and experimental a_3 temperatures for the three alloys investigated (B1, B2, and B3) as well as the selected DIFT generation temperatures are provided in **Table 5-5**.

Table 5-5: Simulated and experimental a3 temperatures for the alloys of (B-) group selected for DIFT experiments as well as their respective DIFT generation temperatures.

Alloy	Simulated a_3 temperatures (°C)	Experimental a_3 temperatures (°C)	DIFT generation temperatures (°C)
B1	835	805	760
B2	914	905	760
B3	1004	1120	860

Figure 5-27 illustrates the DIF grains generated in martensitic microstructures. The DIF was not detected using Nital as the etchant, as it was not possible to differentiate between the γ_r and the α grains, hence, Le Pera reagent was used etching α shades of brown or blue. The DIF takes the form of fine equiaxed grains that nucleate along the prior γ grain boundaries, a morphology similar to that reported in literature [114,115]. The lowest amount of DIF was generated in the B1 specimens, recorded at 5 and 12 vol.% after holding for 15 and 30 min, respectively. 10 and 12 vol.% ferrite was generated in B2 after holding for 15 and 30 min, respectively. The highest amount of DIFT was generated in B3 at 14 and 20 vol.% after holding for 15 and 30 min, respectively.

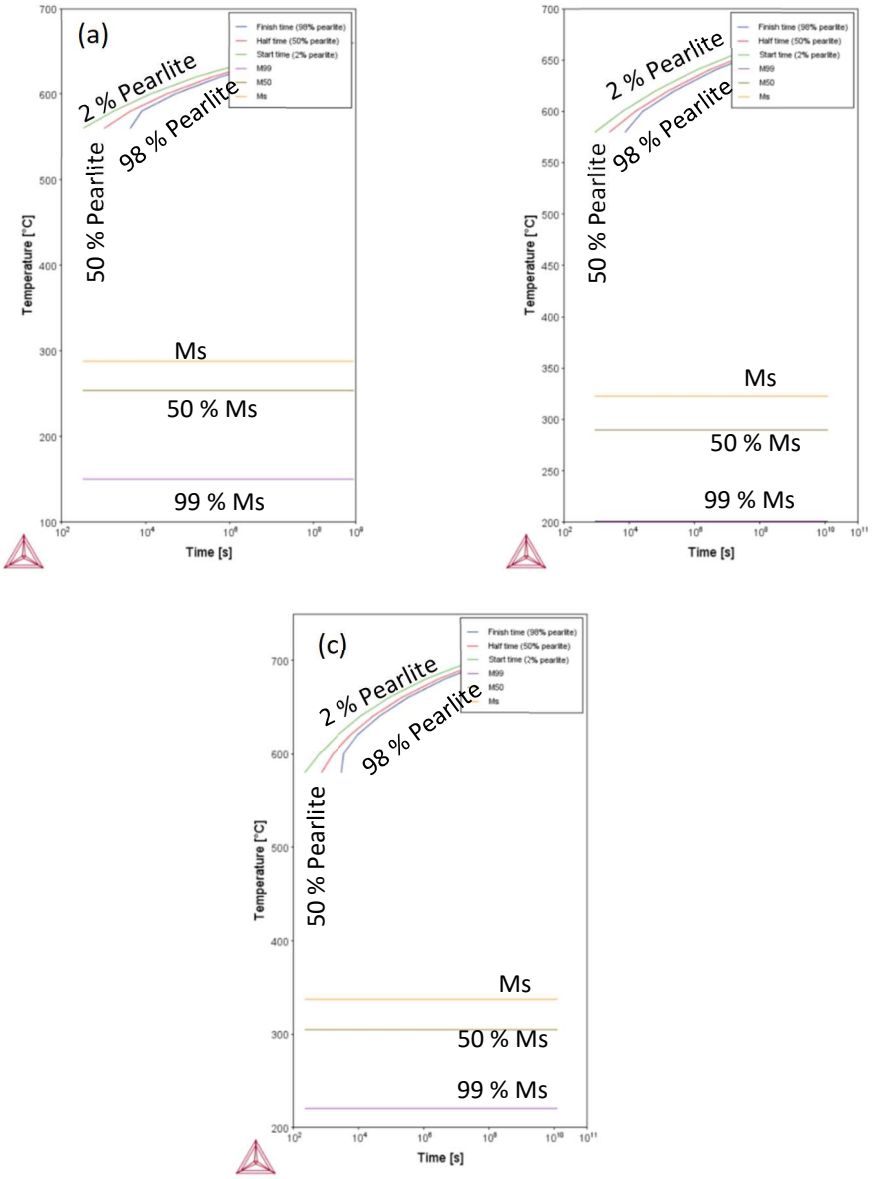

Figure 5-29: ThermoCalc simulated TTT curves for (a) B1, (b) B2, and (c) B3 alloys.

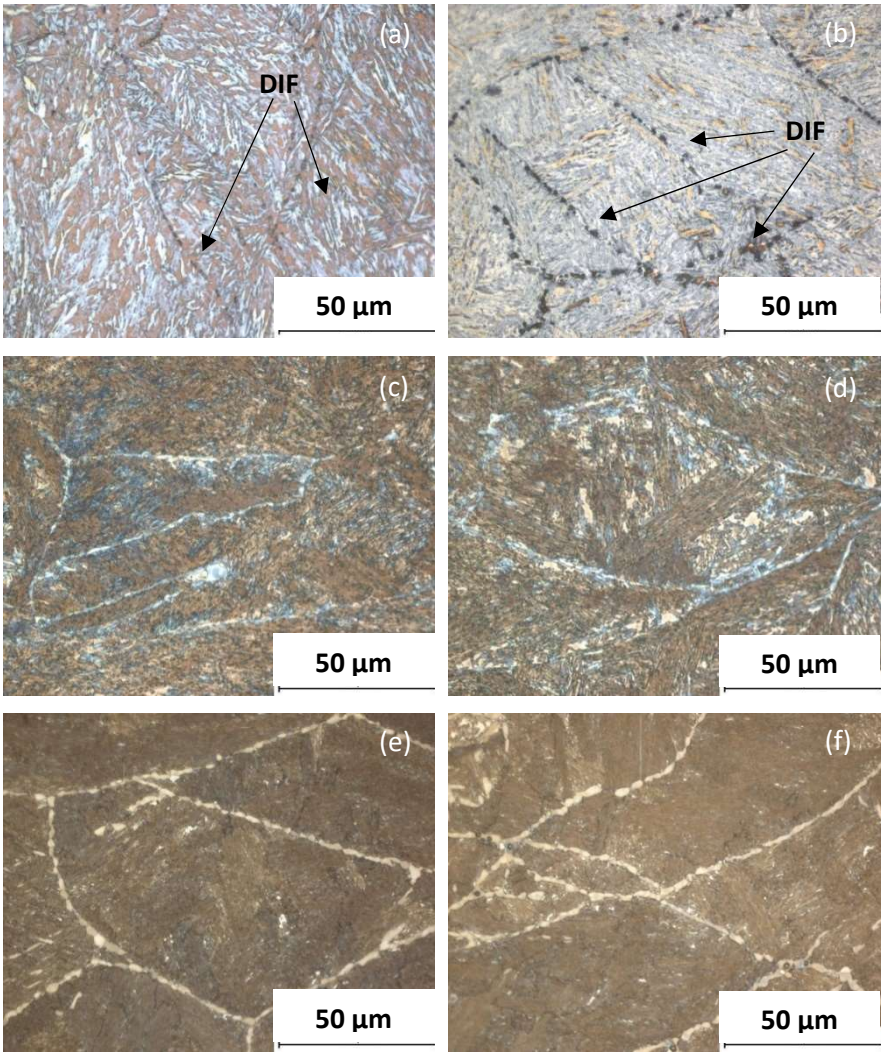

Figure 5-30: LOM images of DIFT specimens undergoing 0.5 deformation of (a) B1 at 760 °C and isothermally held for 15 min before austempering, (b) B1 at 760 °C and isothermally held for 30 min before austempering,(c) B2 at 760 °C and isothermally held for 15 min before austempering, (d) B2 at 760 °C and isothermally held for 30 min before austempering, (e) B3 at 860 °C and isothermally held for 15 min before austempering, (f) B3 at 860 °C and isothermally held for 30 min before austempering.

Figure 5-28 shows stress-strain curves of the B2 and B3 tensile specimens with DIF in their microstructures in comparison to isothermally treated B2 and B3 fine bainitic specimens. No tensile testing results could be obtained for the B1 specimen since, similarly to the case of the A13 specimen discussed in **Section 5.6.1**, high notch sensitivity of the microstructure generated led to the specimens breaking near the specimen shoulders. However, in this case, the notch sensitivity is likely caused by the large geometry of the specimen, which places the specimen shoulders further away from the heaters in the TTS820 TM simulator, meaning that, as shown in **Figure 5-28 (c)** during quenching to the austempering temperature, their temperature is expected to drop below the Ms, generating a considerable amount of brittle martensite. The presence of martensite at the radii of the specimen, coupled with the critical geometry present at the radius is expected to lead to brittle fracture at said radii.

The tensile behaviour of B2 (**Figure 5-28 (a)**) indicates that introducing DIF into the microstructure of a nB alloy results in a drop of the tensile strength, with the UTS dropping from 1303 MPa for the isothermally treated condition to 1250 MPa and 1230 MPa for the conditions where a deformation of 0.5 was applied and the specimens were held at the deformation temperature for 15 and 30 min, respectively. A reduction in tensile strength is expected to be associated with the introduction of soft, low-strength phases such as ferrite into the microstructure. Additionally, a marked improvement in the EL%, namely the uniform elongation, can be observed as a result of introducing the DIF to B2. An initially low uniform elongation value of 4.1 % was improved to approx. 8 % for both DIF specimens. On the other hand, introducing DIF to the B3 alloy (**Figure 5-28 (b)**) led to a drop of 35-45 MPa in tensile strength and no effect on the uniform elongation, remaining around 3 % for

all 3 conditions. However, the total elongation of the DIF specimens dropped down to 4 % and 5.5 % for the conditions held for 15 and 30 min, respectively.

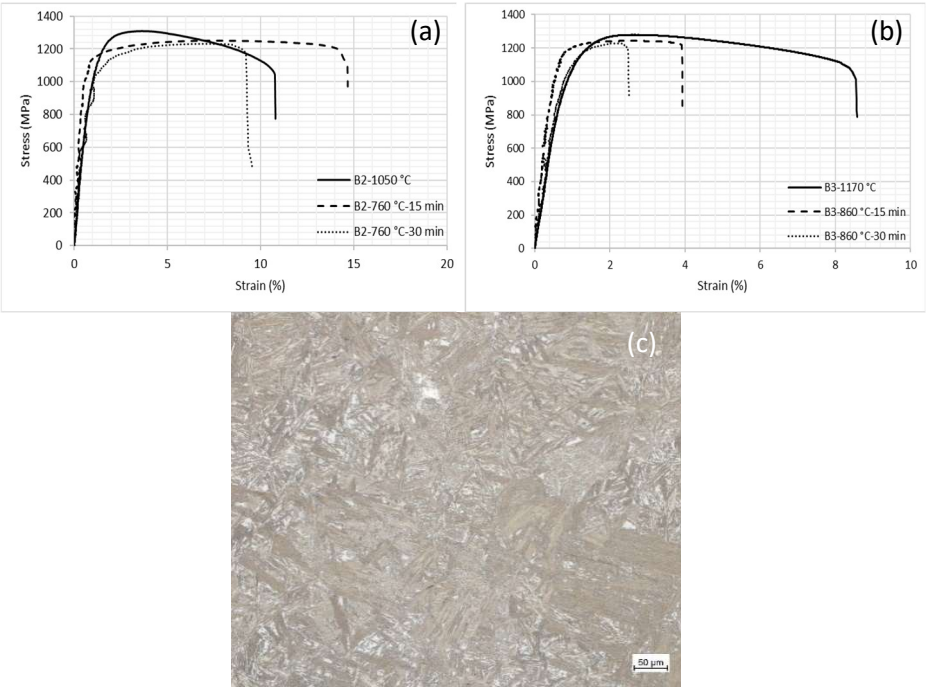

Figure 5-31: Stress-strain curves for (a) B2, (b) B3, with and without DIF in their bainitic microstructure, and (c) LOM image of the shoulder of B1 tensile specimen showing a fully martensitic structure.

5.6.5. Bake hardening

Literature sources on the BH behaviour of nB steels are severely lacking, with only Soliman and Palkowski (2016) reporting preliminary testing results showing a very promising BH response [16]. The fine, nano-sized lamellar microstructure of nB steels is expected to yield a significant BH response, as a finer microstructure is reported to improve the BH strength increase [116,117]. **Figure 5-29** shows

representative stress strain curves for group A1 alloys in the un-aged condition as well as after being subjected to a BH_{20} treatment. An increase in yield strength of 213 MPa was recorded for A11, while both A12 and A13 record approx. a 250 MPa yield increase. No drop in EL% can be detected after a BH_{20} treatment after factoring in the 2 % pre-straining applied, implying that strain ageing had no negative effect on the ductility of the investigated microstructures.

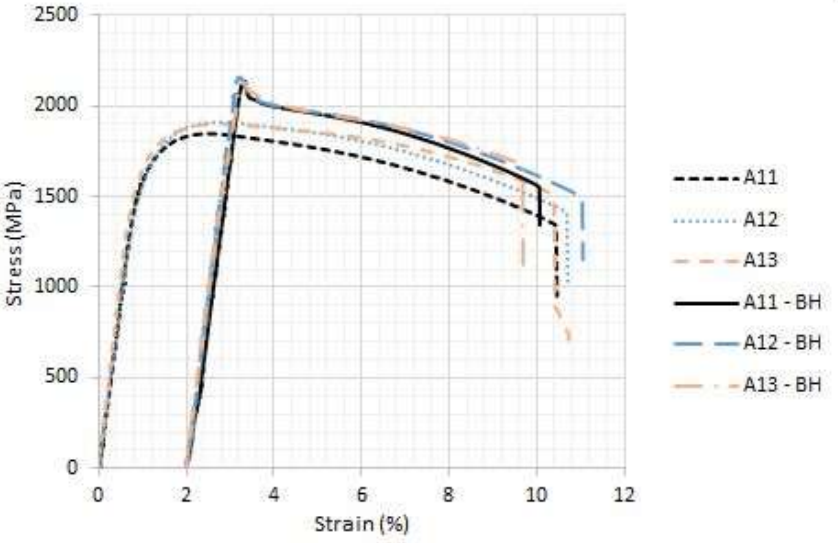

Figure 5-32:Stress-strain curves for the (A1-) group with and without BH20 treatment.

Literature describes the strain ageing process as one consisting of three stages. The first is an initial lower plateau attributed to Cottrell atmosphere formation hindering dislocation motion. The second plateau is responsible for the maximum achievable increase in yield strength and is attributed to the precipitation of fine carbide clusters, further hindering dislocation movement. The final stage is over-ageing, where the carbide clusters coarsen leading to a reduction in their ability to hinder dislocation motion and, consequently, a drop in yield strength [68,118]. Since the yield strength

increase associated with strain ageing is related to the precipitation of fine carbide particles, it would be plausible to postulate that the conditions for strain ageing would be sufficient for the tempering of martensite grains, a process which is also dependent on fine carbide precipitation. The tempering of martensite grains that formed from unstable γ during cooling after austempering would explain why the aged alloys retained their original ductility after the strain ageing process.

Extensive strain ageing experiments were conducted on the A13-2, B2 and B4 alloys to determine their bake hardening profiles as well as help expand the MatCalc bake hardening model, originally developed for dual phase steels, to include nB microstructures. Strain ageing experiments were performed on the aforementioned alloys at R.T., 100 °C, 170 °C and 200 °C at ageing times from 2 to 10000 min. The experimental findings were used to validate the results obtained from the MatCalc model. The original MatCalc bake hardening model was developed for DP steels. The model, described in [119], regards Cottrell atmosphere formation and carbide precipitation as separate processes. The Cottrell atmosphere formation model [120] was used to model the initial phase of the ageing process, while the classical nucleation theory [121] and SFFK growth model [122] were employed for the carbide precipitation stage. The model was adjusted to account for bainitic ferrite being the phase undergoing strain ageing (contrary to martensite in DP steels). The trapping energy for C in dislocations (ΔE) was set as 55000 – 20T, where T is the temperature. Additionally, the coefficient (A) for the coordination number was taken as 104. The dislocation density was set to 1×10^{16} and 9×10^{15} for the alloys austempered at 310 °C and 350 °C, respectively [123], [124]. The C content of the bainitic ferrite was taken as 0.03 wt.% [125]. Finally, the C diffusion in bainitic ferrite was corrected by 5×10^{-2} for A13-2 and B2 and by 10^{-1} for B4 to account for the effect of C supersaturation in steel on lowering the diffusivity reported in [126].

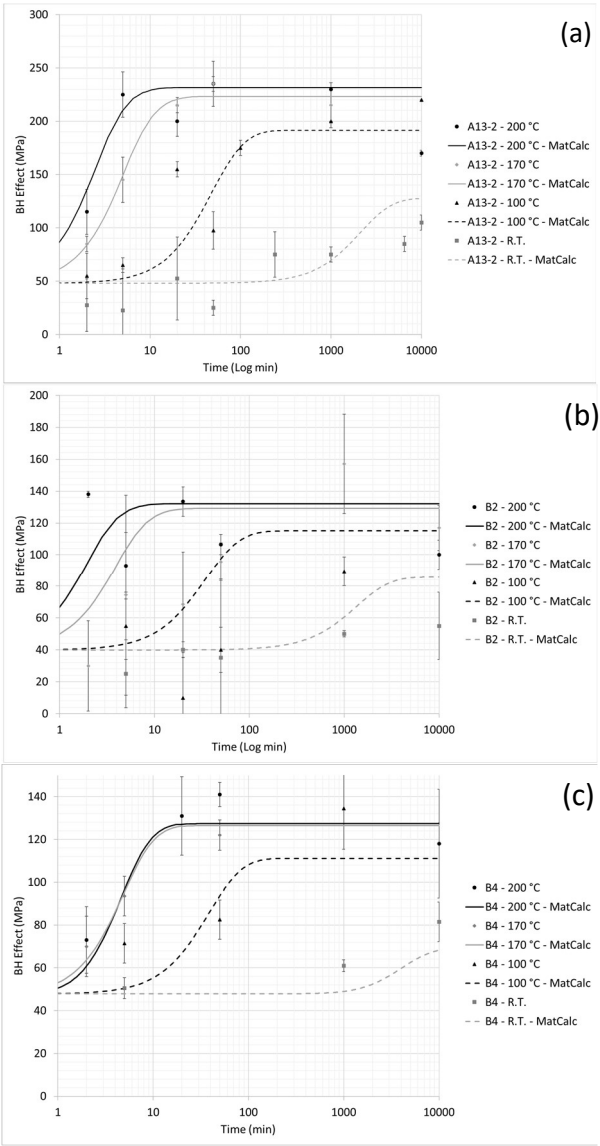

Figure 5-33: Experimental vs. MatCalc simulated bake hardening response for (a) A13-2, (b) B2 and (c) B4.

Figure 5-30 shows the bake hardening response obtained from experimental results as well as the MatCalc simulations for the three alloys investigated. All three alloys illustrate rapid bake hardening strength increases at the highest temperatures of 200 and 170 °C, with A13-2 reaching the upper plateau after about 5 min, while B2 and B4 reach it within the first 10 – 20 min. The MatCalc model predicts similar ageing kinetics at both 200 and 170 °C, which was confirmed by the experimental findings, especially in the case of B4 (**Figure 5-30 (c)**) where the bake hardening profiles at both temperatures are almost identical. The bake hardening strength increase was recorded at the upper plateau for A13-2 at 230 MPa (**Figure 5-30 (a)**), while those for B2 and B4 were recorded at about 130 MPa (**Figure 5-30 (b, c)**). The difference in strength increase is attributed to the aforementioned effect of the finer lamellar thickness of A13-2 (39 nm) in contrast to those of B2 and B4 (68 and 88 nm, respectively).

Literature reports that an increase in ageing temperature only serves to accelerate the ageing kinetics without affecting its underlying mechanisms [67,118]. Conversely, the MatCalc simulation predicts a lower value for the upper plateau after ageing at 100 °C than that obtained after ageing at 200 and 170 °C. Furthermore, the experimental findings also imply an upper plateau with a lower value, however, the experimental values are consistently higher than those predicted by MatCalc. On the other hand, all three alloys failed to reach the upper plateau after ageing at R.T. up to an ageing time of 10000 min. The MatCalc simulation was able, with sufficient accuracy, to predict the ageing kinetics at R.T., with the increase towards the upper plateau recorded to begin after about 1000 min of ageing time for all alloys.

As previously discussed in this section, carbide precipitation is the main mechanism behind the second stage of bake hardening and is the cause of the yield strength increase reaching the second plateau. Henceforth, accurate prediction of the development of the precipitate size during ageing is key to simulate the bake

hardening profiles. **Figure 5-31** shows TEM micrographs of A13-2 aged at 200 °C for 50 min (**Figure 5-31 (a)**), B2 aged at 200 °C for 20 min **(Figure 5-31 (b))** and B4 aged at 200 °C for 20 min **(Figure 5-31 (c))**, representing ageing times where the respective alloys reached the upper plateau. The TEM micrographs illustrate precipitates around a size of 10-30 nm, which is similar to that predicted by the MatCalc simulation **(Figure 5-31 (d))** at 45 nm. The simulated precipitate size development does not predict over-ageing over the duration investigated, which would be indicated by an increase in the precipitate size over time. The predicted precipitate size for A13-2 and B2 remain constant at about 45 nm for the full duration of the ageing time, which is in line with the experimental results showing no drop in strength due to over-ageing. On the other hand, MatCalc predicts an increase in precipitate size for B4 after 2000 min of ageing, reaching about 70 nm after 10000 min. However, neither the simulated bake hardening profiles nor the experimental results for B4 indicate any loss of strength resulting from this predicted coarsening of precipitates. Implying that a size of 70 nm is not sufficiently large to cause the drop in strength associated with over-ageing.

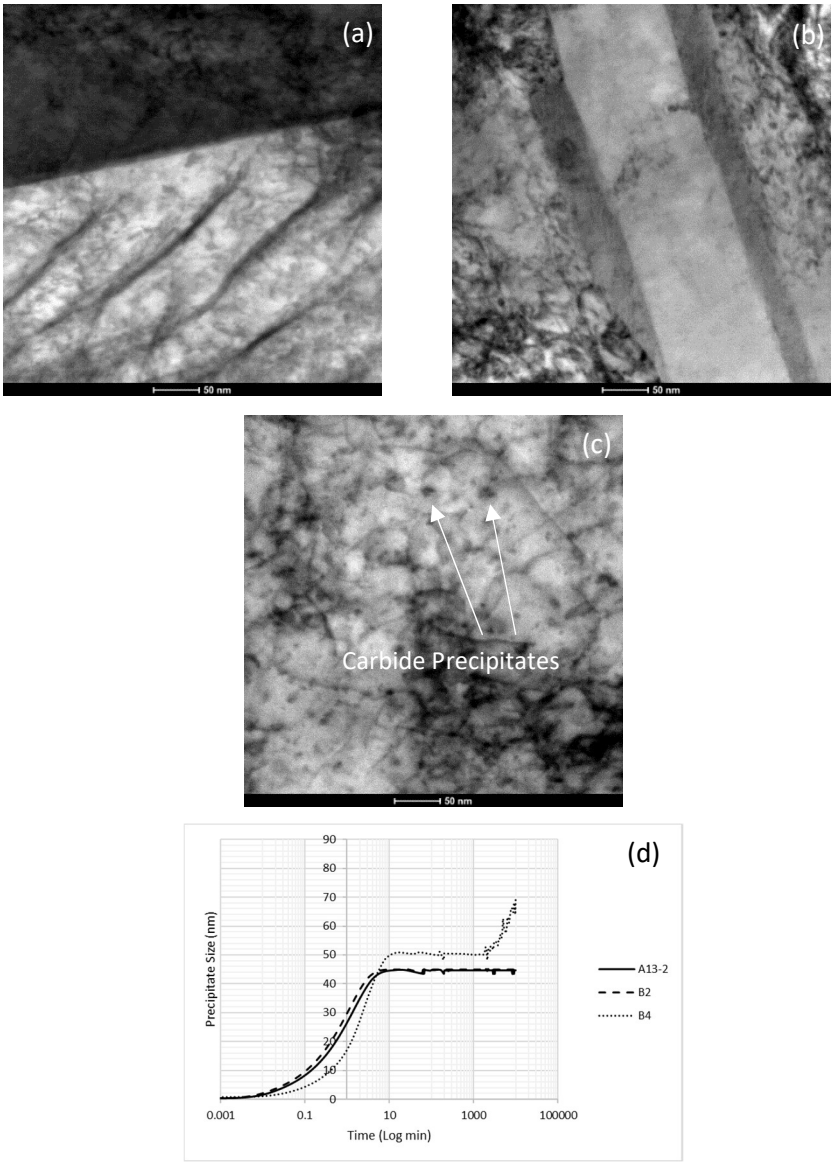

Figure 5-34: TEM micrographs of (a) A13-2 aged at 200 °C for 50 min, (b) B2 aged at 200 °C for 20 min (c) B4 aged at 200 °C for 20 min, and (d) MatCalc simulated development of the precipitate size with ageing time after ageing at 200 °C.

5.6.6. Fracture surface analysis

Figure 5-32 shows the fracture surfaces for selected conditions of the nB alloys investigated at low magnification. All alloys - except for A4 - displayed some extent of cup and cone fractures, indicative for a ductile behaviour. On the other hand, the fracture of A4 tensile specimens appear to be 100 % brittle, with no evidence for ductile regions observed under the SEM, and with the crack seemingly originating from a region on the edge of the specimen, where a large graphite particle was observed (**Figure 5-33 (a)**).

A31 and B4 possess 10 vol.% δ-ferrite in their microstructure, which, as a soft phase, is expected to improve the ductility at the cost of reducing the alloy's strength. Both fracture surfaces indicate ductile fracture (**Figure 5-32 (a)** and **(c)**) though the causes for fracture appear to be different. Upon inspecting the A33 alloy (**Figure 5-33 (d)**), it would appear that the fracture was caused by the brittle failure of certain regions that are distributed over the cross section of the specimen. These brittle features have a maximum size of 20 μm, some of them even smaller. These features are similar in size to the martensite grains depicted in **Figure 5-19 (a)** for A13-2, which further supports the hypothesis that the brittleness of the higher Al (A3) group is caused by a higher γ_r content that transforms into brittle martensite in the microstructure. Contrary to A33, both of the specimens with δ-ferrite in the microstructure (A31 and B4) appear to have a dispersion of micro cracks that are surrounded by regions of brittle fracture, implying that the failure occurred at those regions.

The mechanical property mismatch between the soft δ-ferrite and the harder bainite and martensite would lead void coalescence and cracking at the interface between δ-ferrite and the surrounding hard phases, resulting in fracture surfaces with features such as those observed in **Figures 5-33 (c)** and **(f)**. The presence of a soft phase in the microstructures of A31 and B4 improved their ductility as well as their strain hardening capacity and, consequently, a total elongation over all the other alloys

with similar alloying strategies. It has been observed that, regardless of composition, amounts of phases, or austempering temperature, the EL% for all investigated conditions remained within the range of 8-11 %, except for the alloys B1 and B4. This result implies the presence of a factor that is more or less constant among all conditions, limiting the ductility to the values obtained; such a factor does not exist (or at least exists at a lesser extent) in the alloys B1 and B4.

The main drawback of the alloying strategy employed in this investigation is that it generates microstructures with γ of low stability. Upon loading, these γ blocks would quickly transform into martensite limiting their ductility, with B1 and B4 being the exceptions because of the low Al and higher Mn of B1, as well as B4 having the highest Mn content in all the alloys studied, which would mitigate the negative effects the alloying strategies employed has on the γ formation in both alloys. As a result, they record a higher EL% during tensile testing.

A possible improvement that could be employed to increase the stability of the γ is to refine the prior γ grains. Long homogenization times are a common practice in nB literature; however, this process is expected to result in a significant amount of grain growth. Larger prior γ grains, as previously mentioned in **Section 2.3.1**, are reported to lower the γ stability and increase the C diffusion distance during partitioning, which in turn would cause the centre of these large blocks to have lower C and hence transform into martensite during cooling. In addition to that, refining the γ grains would further accelerate the bainitic transformation as the increased density of grain boundaries would facilitate bainite nucleation.

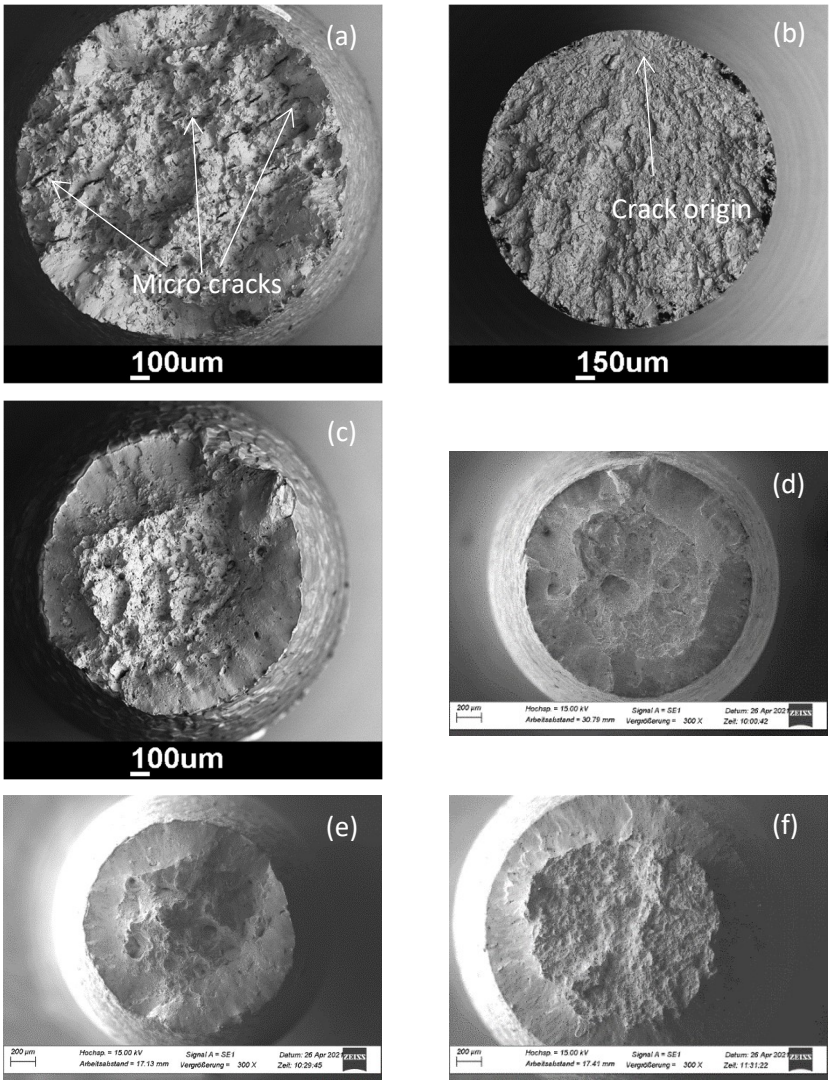

Figure 5-35: Micrographs for the fracture surfaces of (a) A31 austempered at 350 °C, (b) A4 austempered at 310 °C, (c) B4 austempered at 350 °C, (d) B1 austempered at 310 °C, (e) B2 austempered at 350 °C, and (f) A13-2 austempered at 310 °C.

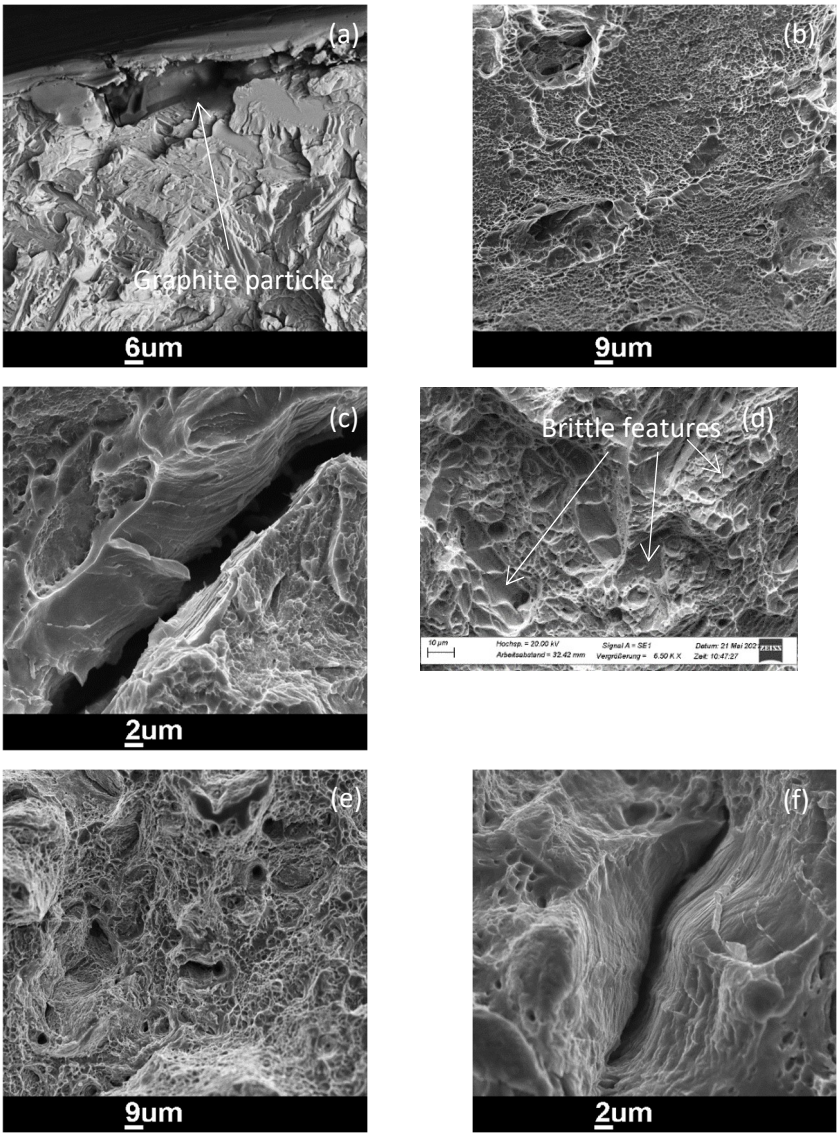

Figure 5-36: SEM micrographs of (a) A4, graphite particle at crack origin, (b) A31, ductile fracture, (c) A31, brittle regions near cracks, (d) A33, brittle regions distributed throughout the fracture surface, (e) B4, ductile fracture, (f) B4, brittle regions around cracks similar to A31.

5.6.7. General discussion

While the results presented in this thesis indicate an initial success at achieving the projected goals of low cost, high strength and fast transformation time, a separate assessment is needed for the feasibility of the alloying strategies presented as well as their practical viability. The addition of Al to a steel alloy has the theoretical effect of accelerating the bainitic transformation as well as increasing the amount of the bainitic phase in the final microstructure. However, owing to the aforementioned negative effects that Al has on hardenability, a high Al alloying strategy must be accompanied by additions of hardenability elements, in this study Mn and C, which would hinder the benefits of the high Al content.

Figure 5-34 shows the change in bainitic transformation time with changing Al and Mn content for all of the alloys investigated. **Figure 5-34 (a)** shows that an increase in Al from 1 to 3 wt.% in general leads to a slight increase in transformation time. Further increasing Al to 5 wt.% results in transformation times dropping back to similar ranges of those with 1 wt.% Al. However, the main factor affecting the transformation time is the Mn content as presented in **Figure 5-34 (b)**. As illustrated in **Figure 5-34 (b)**, the bainitic transformation time steadily increases with increasing Mn content, which puts into question the viability of using Al for transformation acceleration if it must be accompanied by the addition of Mn that lowers its effect (in case of 5 wt.% Al conditions) or even completely negates it (in case of 3 wt.% Al conditions).

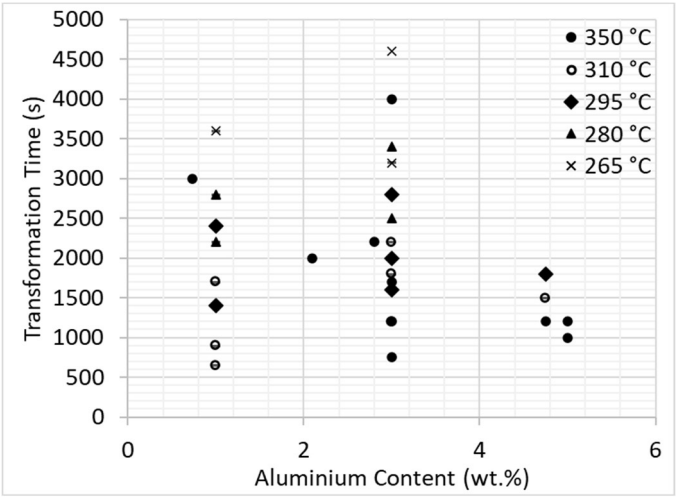

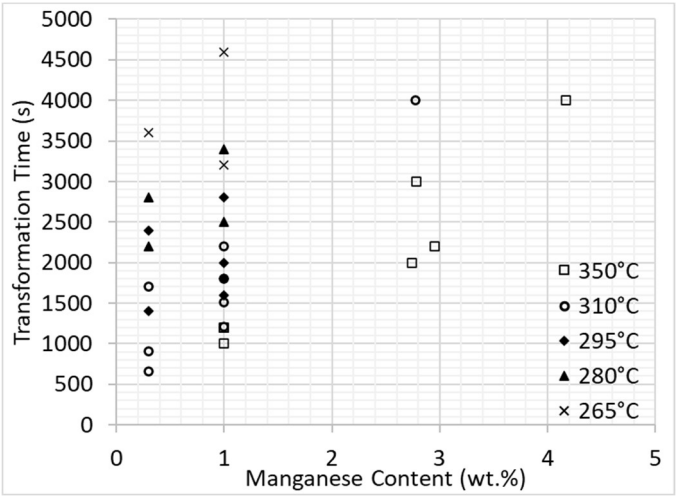

Figure 5-37: Change of bainitic transformation time with (a) Al content, (b) Mn content.

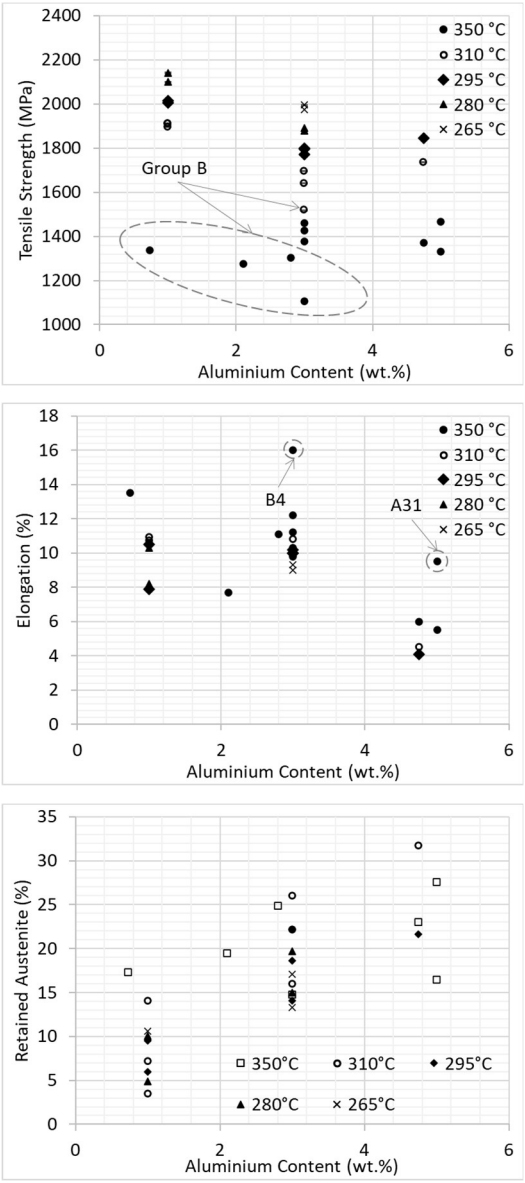

Figure 5-38: Effect of Al content on (a) tensile strength, (b) EL%, and (c) γr content.

Additionally, the mechanical properties resulting from the addition of Al as well as its accompanying hardenability elements need to be considered along with the transformation time. According to the data presented in **Figure 5-35 (a)**, there is a tendency for tensile strength to drop with increasing Al content, with the aforementioned exception of that case being the A33 alloy displaying a slightly increased tensile strength over its (A2-) group counterparts. The drop in tensile strength is more pronounced when considering that an increase in Al content up to 5 wt.% limited most of the conditions to ausforming at the high temperature of 350 °C (A31 and A32), as well as generating microstructures with δ-ferrite (A31), which drastically reduced the microstructure's strength potential.

Additionally, lower C variants continuously record tensile strength lower than their higher C counterparts at the same transformation temperature. While the C content is not supposed to directly influence the strength of a nB alloy, with the bainitic lamellar thickness being the main factor dictating it [16], higher C indirectly leads to finer bainitic lamellae by increasing the γ strength. This drop in tensile strength is accompanied by a marginal increase in the EL% (**Figure 5-35 (b)**) as the Al content is increased to 3 wt.%. However, a steep drop in EL% results from further increasing the Al content to 5 wt.%, hindering the utilization of the transformation acceleration and strength improvement that the 5 wt.% Al condition provides compared to the 3 wt.% condition. The only ones recording an EL% value significantly higher than the other conditions with the same Al content are those for B4 and A31 owing to the presence of δ-ferrite, which deteriorates their tensile strength and impact properties. On the other hand, the alloy B1 austempered at 310 °C recorded a higher tensile strength compared to A2 and A3 austempered at 350 °C, implying that the transformation temperature is the most significant factor concerning the mechanical properties of nB alloys. This finding has significant implications on the conclusions of this study considering that increasing the Al content is usually accompanied by

the restriction of austempering temperatures to higher values as a result of an increased Ms.

Moreover, as depicted in **Figure 5-35 (c)**, an increased Al content is also accompanied by an increased amount of γ_r in the final microstructure. This result contradicts known literature ones (**Section 2.4.1**) as Al is commonly reported being an element that increases the driving force for the bainitic transformation and is thus expected to lower the final fraction of γ_r in the microstructure. However, the observed increase in γ_r fraction is only indirectly a result of the added Al, but more the effect of the increased Mn and C required to maintain a high Al alloy's hardenability and low Ms. This increased γ_r fraction is likely the cause for the reduced tensile strength displayed by the (A2-) and (A3-) groups.

The findings of the current research present the need for a compromise between transformation time and mechanical properties, with the faster transformation times accompanied by a reduction in EL%. However, to put the advantages and drawbacks of the presented alloying strategy into perspective, it must be compared to the results of nB alloys reported in literature. **Figure 5-36** represents a comparison between a wide selection of the nB alloys found in literature (from the references provided in **Table 2-1**) and the different alloy groups investigated over the course of this research. **Figure 5-36 (a)** illustrates a trend over the years of the transformation time dropping at the cost of a reduction in tensile strength. On the other hand, the data presented in **Figure 5-36** also indicate that all of the alloy groups studied present a considerable improvement, in terms of transformation times, over the results reported in literature. Additionally, the tensile strength values recorded compare very well to the strength values reported in literature, with the exception of the conditions austempered at 350 °C, displaying the lowest strength values among all of the conditions listed.

The EL% values shown in **Figure 5-36 (b)** indicate that the alloys investigated recorded values that are considerably lower than those ones reported in literature with an average EL% of 9 % for the investigated conditions as compared to the 14 % for the results obtained from literature. An improvement in the EL% values would be necessary to ensure that the developed nB alloys are competitive with the conditions that reached a tensile strength of around 1800 MPa at EL% values upwards of 15 %. The exact mechanism with which γ_r contributes to the ductility of nB remains yet unclear in the present literature, with contradicting reports on whether the TRIP effect positively contributes to the ductility of nB [127]. Attempts to improve the ductility of the proposed alloying strategies would need to be preceded by a sufficient understanding of the underlying mechanisms governing the relationship between γ_r, its amount, stability, deformation mechanisms and morphology on the ductility of nB. Additionally, from the results depicted in both **Figures 5-36 (a)** and **(b)** it is evident that while alloying nB steels with 5 wt.% Al successfully lowers the transformation time, it is nonetheless counterproductive. The 5 wt.% Al (A3-) group could only achieve high tensile strength values (1750-1850 MPa) at a C content of 0.9 wt.%, lower C contents increased the Ms above 300 °C severely limiting the maximum attainable strength of A31 and A32. Moreover, even for A33, which could be austempered at 310 and 295 °C, the EL% values recorded were among the lowest recorded ones for nB alloys, both in this investigation and the literature covered in general, implying that Al additions beyond 3 wt.% are not beneficial.

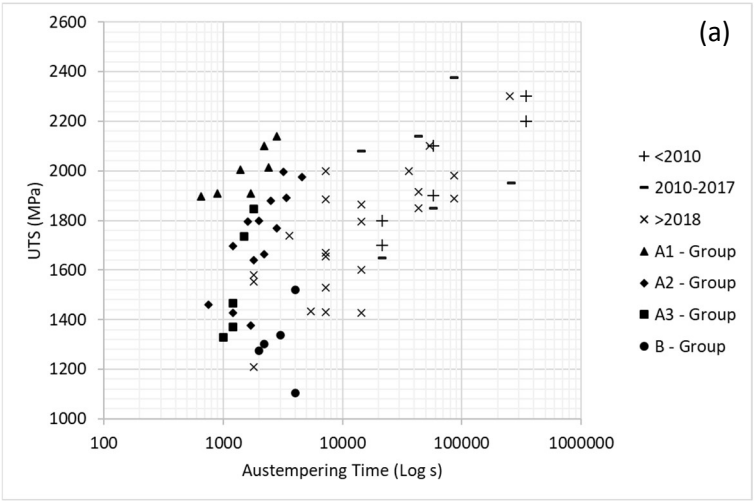

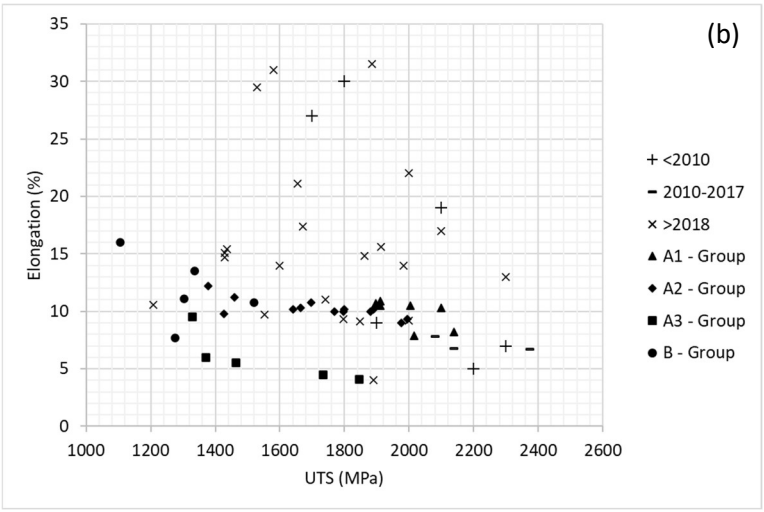

Figure 5-39: Comparison between the alloys developed and nB alloys from different time periods in the literature available since 2010 in terms of (a) tensile strength vs austempering time, and (b) EL% vs tensile strength.

One of the main aims of this research was the development of low-cost alloying strategies for nB alloys with fast transformation times. Hence, part of the assessment of the success of this current research is through how the cost of the alloys developed compares to that of nB alloys found in literature. **Figure 5-37** illustrates how the nB alloys developed perform in terms of cost of substitutional elements [75] as compared to the alloys found in literature and listed in **Table 2-1**. It is apparent from **Figure 5-37 (a)** that the alloys developed provide the best combination of low cost and fast transformation time. On the other hand, a number of alloying strategies found in literature achieved lower substitutional element cost, however, these are mostly nB steels that only rely on alloying with Mn and Si and employ no transformation accelerating elements, hence why they underperform in terms of transformation time. On the other hand, the data provided in **Figure 5-37 (b)** indicate that in terms of tensile strength there are other strategies in the current literature that provide similar, or even higher, strength values at similar -or slightly lower- costs. The results presented in **Figure 5-37** further reinforce the premise followed in this research that nB alloy design is an optimization problem between alloying element cost, mechanical properties and transformation time. The strategies relying on alloying with Mn and Si only would provide the lowest costs and highest strengths at the cost of long transformation times, those relying on Co addition would have faster transformation times and high strength but would suffer from higher costs. The alloying strategies presented in this research provide a compromise, where a comparable - if slightly lower - tensile strength is achieved at comparably low costs while providing the benefit of accelerated transformation times.

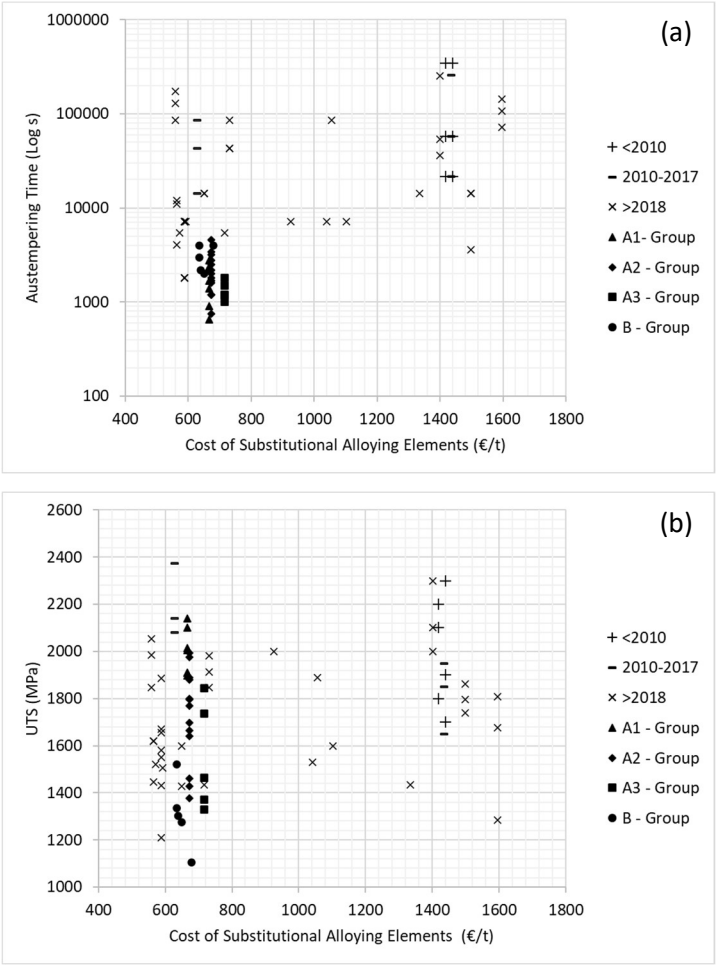

Figure 5-40: Comparison between the alloys developed and nB alloys from different time periods in the literature available since 2010 in terms of cost of substitutional alloying elements vs (a) austempering time, (b) UTS.

6. Conclusions and outlook

6.1. Conclusions

Three low-cost alloying strategies for the generation of nano-bainitic microstructures were developed and investigated, aiming at high mechanical properties as well as fast transformation times. The main findings of the investigation are as follows:

1- Nano-bainitic microstructures were successfully generated with mechanical properties on par with those reported in literature by using alloying strategies that completely exclude expensive alloying elements such as Co, Cr, and Ni.
2- Fast transformation times with a minimum of 650 s and a maximum of 6000 s were recorded, which presents a significant improvement over the transformation times commonly reported in literature.
3- Alloying with minimal Mn as well as 1 wt.% Al in the (A1-) group yielded the best combinations of tensile strength as well as transformation time.
4- Increasing the Al content up to 3 wt.% in the (A2-) group slightly improves the transformation time as well as improves the impact properties while yielding a slight drop in tensile strength.
5- Increasing the Al content further to 5 wt. in the (A3-) group improved the tensile strength over the 3 wt.% Al condition, while also improving the transformation time over all other conditions of similar C content. Conversely, the addition of this high amount of Al was detrimental to the alloy's ductility.
6- The low C alloy (B-) group yielded the longest transformation times among all the groups investigated (2000 – 4000 s at 350 °C) as well as the lowest strength values. However, the highest ductility results were recorded by alloys from this group.

7- The major factor affecting the tensile strength of the alloys investigated was the austempering temperature, with lower temperatures yielding improved mechanical properties due to a finer bainitic thickness as well as a higher fraction of α_b generated. This presented a challenge for the alloys with higher Al contents due to their higher martensite start temperature limiting their ausforming temperatures to higher values and consequently lowering their maximum attainable strength.

8- The strategies proposed rely on improving the driving force for α formation at the cost of that of γ, this had the negative effect of creating unstable γ_r that transformed to martensite at low levels of loading leading to ductility values that are lower than those achievable by other nano-bainitic alloys reported in literature.

9- The presence of δ-ferrite in a nano-bainitic microstructure improves the ductility of the alloy at the cost of a drop in both the tensile strength as well as the impact properties.

10- Nano-bainitic microstructures illustrated very high bake hardening strength improvements without noticeable losses in ductility.

11- Successful bainitic transformation during continuous cooling illustrate the potential for sheet products of the low C variants (B-) to be austempered in the rolling mill during the coiling process.

6.2. Outlook

Some drawbacks were found for the proposed alloying strategies. The limitations in martensite start temperature as well as the γ_r stability, which dictates the alloy's ductility, would need to be addressed to make the proposed low-cost strategies even more viable. However, attempting to increase the γ stability would contradict the original aim of increasing the driving force for α transformation, and would lead back to longer austempering times. Therefore, this line of thinking was not

conceptually pursued. On the other hand, the high Al additions used in this study imply that the concept of nano-bainite could be extended to low density steels. Combining the two concepts of low density and nano-bainitic steels would yield interesting specific properties that would be of interest, not only for the automotive industry. Moreover, there is a good synergy between the heat treatment cycles required to generate nano-bainitic microstructures and those required to avoid the formation of large-sized, brittle AlN precipitates in low density steels. Currently, funding from the Deutsche Forschungsgemeinschaft (DFG) was granted for a project to investigate the behaviour as well as optimize alloy designs for low density nano-bainitic steels. Work on this project is expected to start in the beginning of 2022.

Additionally, the findings of this research shed the light on the lack of a complete understanding of the factors affecting the ductility of nB alloys. Further research into the how the γ_r influences the ductility of nB is essential for the continued progress of this type of steels. A research project is currently under formulation, where the effect of the γ_r on the ductility of nB at different austempering temperatures will be thoroughly investigated. Additionally, a neural network model is planned to be developed, with the aim to predict the mechanical properties of nB alloys based on inputs of the chemical composition and transformation temperature.

Finally, while a wealth of basic research into the topic of nB exists in the present literature, there is a lack of research into how these steels can translate into actual products. A transfer project is currently being formulated, whereby the deformability of low C nB alloys will be investigated with the final aim of fabricating a formed sheet product by an industry partner. Furthermore, the sheet product will then be subjected to the relevant testing to ensure its viability for the selected application. This project is planned to present a proof of concept that nB steel sheet products can be employed as a replacement for the currently available high strength steels.

Bibliography

1. Fonstein, N. *Advanced High Strength Sheet Steels;* Springer International Publishing: Cham, 2015.
2. Rowe, J.D. *Advanced materials in automotive engineering;* Woodhead: Oxford, 2012, ISBN 978-0-85709-546-6.
3. Shome, M.; Tumuluru, M. *Welding and joining of advanced high strength steels (AHSS)*, 1st edition; Elsevier: Amsterdam, 2015, ISBN 978-0-85709-858-0.
4. Varshney, A.; Sangal, S.; Kundu, S.; Mondal, K. Super strong and highly ductile low alloy multiphase steels consisting of bainite, ferrite and retained austenite. *Mater. Des.* **2016**, *95*, 75–88, doi:10.1016/j.matdes.2016.01.078.
5. Caballero, F.G.; Bhadeshia, H. Very strong bainite. *Curr. Opin. Solid State Mater. Sci.* **2004**, *8*, 251–257, doi:10.1016/j.cossms.2004.09.005.
6. Garcia-Mateo, C.; Caballero, F.G.; Bhadeshia, H. K. D. H. Acceleration of Low-temperature Bainite. *ISIJ Int.* **2003**, *43*, 1821–1825, doi:10.2355/isijinternational.43.1821.
7. Garcia-Mateo, C.; Caballero, F.G. Ultra-high-strength Bainitic Steels. *ISIJ Int.* **2005**, *45*, 1736–1740, doi:10.2355/isijinternational.45.1736.
8. Bhadeshia, H. K. D. H.; Edmonds, D.V. Bainite in silicon steels: new composition–property approach Part 1. *Met. Sci.* **1983**, *17*, 411–419, doi:10.1179/030634583790420600.
9. Zhang, F.; Yang, Z. Development of and Perspective on High-Performance Nanostructured Bainitic Bearing Steel. *Engineering* **2019**, *5*, 319–328, doi:10.1016/j.eng.2018.11.024.
10. Bhadeshia, H. K. D. H.; Christian, J.W. Bainite in steels. *Metall. Trans. A* **1990**, *21*, 767–797, doi:10.1007/BF02656561.
11. Bhadeshia, H.; Edmonds, D.V. The mechanism of bainite formation in steels. *Acta Metall.* **1980**, *28*, 1265–1273, doi:10.1016/0001-6160(80)90082-6.
12. Singh, S.; Bhadeshia, H. Estimation of bainite plate-thickness in low-alloy steels. *Mater. Sci. Eng., A* **1998**, *245*, 72–79, doi:10.1016/S0921-5093(97)00701-6.
13. Kabirmohammadi, M.; Avishan, B.; Yazdani, S. Transformation kinetics and microstructural features in Low-Temperature Bainite after ausforming process. *Mater. Chem. Phys.* **2016**, *184*, 306–317, doi:10.1016/j.matchemphys.2016.09.057.

14. Samanta, S.; Biswas, P.; Singh, S.B. Analysis of the kinetics of bainite formation below the M S temperature. *Scr. Mater.* **2017**, *136*, 132–135, doi:10.1016/j.scriptamat.2017.04.030.
15. Wu, H.-D.; Miyamoto, G.; Yang, Z.-G.; Zhang, C.; Chen, H.; Furuhara, T. Incomplete bainite transformation in Fe-Si-C alloys. *Acta Mater.* **2017**, *133*, 1–9, doi:10.1016/j.actamat.2017.05.017.
16. Soliman, M.; Palkowski, H. Development of the low temperature bainite. *Arch. Civ. Mech. Eng.* **2016**, *16*, 403–412, doi:10.1016/j.acme.2016.02.007.
17. Long, X.Y.; Kang, J.; Lv, B.; Zhang, F.C. Carbide-free bainite in medium carbon steel. *Mater. Des.* **2014**, *64*, 237–245, doi:10.1016/j.matdes.2014.07.055.
18. Quidort, D.; Bréchet, Y. The role of carbon on the kinetics of bainite transformation in steels. *Scr. Mater.* **2002**, *47*, 151–156, doi:10.1016/S1359-6462(02)00121-5.
19. He, J.; Zhao, A.; Huang, Y.; Zhi, C.; Zhao, F. Acceleration of Bainite Transformation at Low Temperature by Warm Rolling Process. *Mater. Today-Proc.* **2015**, *2*, S289-S294, doi:10.1016/j.matpr.2015.05.040.
20. He, S.H.; He, B.B.; Zhu, K.Y.; Huang, M.X. On the correlation among dislocation density, lath thickness and yield stress of bainite. *Acta Mater.* **2017**, *135*, 382–389, doi:10.1016/j.actamat.2017.06.050.
21. Yoozbashi, M.N.; Yazdani, S.; Wang, T.S. Design of a new nanostructured, high-Si bainitic steel with lower cost production. *Mater. Des.* **2011**, *32*, 3248–3253, doi:10.1016/j.matdes.2011.02.031.
22. Gong, W.; Tomota, Y.; Harjo, S.; Su, Y.H.; Aizawa, K. Effect of prior martensite on bainite transformation in nanobainite steel. *Acta Mater.* **2015**, *85*, 243–249, doi:10.1016/j.actamat.2014.11.029.
23. Gong, W.; Tomota, Y.; Koo, M.S.; Adachi, Y. Effect of ausforming on nanobainite steel. *Scr. Mater.* **2010**, *63*, 819–822, doi:10.1016/j.scriptamat.2010.06.024.
24. Soliman, M.; Palkowski, H. Microstructure Development and Mechanical Properties of Medium Carbon Carbide-free Bainite Steels. *Procedia Eng.* **2014**, *81*, 1306–1311, doi:10.1016/j.proeng.2014.10.148.
25. Hu, H.; Xu, G.; Dai, F.; Tian, J.; Chen, G. Critical ausforming temperature to promote isothermal bainitic transformation in prior-deformed austenite. *Mater. Sci. Technol.* **2019**, *35*, 420–428, doi:10.1080/02670836.2019.1567663.
26. Caballero; Rementeria; Morales-Rivas; Benito-Alfonso; Yang; de Castro; Poplawsky; Sourmail; Garcia-Mateo. Understanding Mechanical Properties

of Nano-Grained Bainitic Steels from Multiscale Structural Analysis. *Metals* **2019**, *9*, 426, doi:10.3390/met9040426.
27. Tsai, Y.T.; Lin, C.R.; Lee, W.S.; Huang, C.Y.; Yang, J.R. Mechanical behavior and microstructural evolution of nanostructured bainite under high-strain rate deformation by Hopkinson bar. *Scr. Mater.* **2016**, *115*, 46–51, doi:10.1016/j.scriptamat.2015.12.013.
28. Golchin, S.; Avishan, B.; Yazdani, S. Effect of 10% ausforming on impact toughness of nano bainite austempered at 300 °C. *Mater. Sci. Eng., A* **2016**, *656*, 94–101, doi:10.1016/j.msea.2016.01.025.
29. Dong, B.; Hou, T.; Zhou, W.; Zhang, G.; Wu, K. The Role of Retained Austenite and Its Carbon Concentration on Elongation of Low Temperature Bainitic Steels at Different Austenitising Temperature. *Metals* **2018**, *8*, 931, doi:10.3390/met8110931.
30. Asako, S.; Kawabata, T.; Aihara, S.; Kimura, S.; Kagehira, K. Micro-processes of brittle fracture initiation in bainite steel manufactured by ausforming. *Procedia Structural Integrity* **2016**, *2*, 3668–3675, doi:10.1016/j.prostr.2016.06.456.
31. Zhao, J.; Lv, B.; Zhang, F.; Yang, Z.; Qian, L.; Chen, C.; Long, X. Effects of austempering temperature on bainitic microstructure and mechanical properties of a high-C high-Si steel. *Mater. Sci. Eng., A* **2019**, *742*, 179–189, doi:10.1016/j.msea.2018.11.004.
32. Yang, J.; Wang, T.S.; Zhang, B.; Zhang, F.C. Microstructure and mechanical properties of high-carbon Si–Al-rich steel by low-temperature austempering. *Mater. Des.* **2012**, *35*, 170–174, doi:10.1016/j.matdes.2011.08.041.
33. Amel-Farzad, H.; Faridi, H.R.; Rajabpour, F.; Abolhasani, A.; Kazemi, S.; Khaledzadeh, Y. Developing very hard nanostructured bainitic steel. *Mater. Sci. Eng., A* **2013**, *559*, 68–73, doi:10.1016/j.msea.2012.08.020.
34. Zhao, J.; Jia, X.; Guo, K.; Jia, N.N.; Wang, Y.F.; Wang, Y.H.; Wang, T.S. Transformation behavior and microstructure feature of large strain ausformed low-temperature bainite in a medium C - Si rich alloy steel. *Mater. Sci. Eng., A* **2017**, *682*, 527–534, doi:10.1016/j.msea.2016.11.073.
35. Soliman, M.; Mostafa, H.; El-Sabbagh, A.S.; Palkowski, H. Low temperature bainite in steel with 0.26wt% C. *Mater. Sci. Eng., A* **2010**, *527*, 7706–7713, doi:10.1016/j.msea.2010.08.037.
36. Yang, J.; Qiu, H.; Xu, P.; Yu, H.; Wang, Y. The substitution of aluminum for cobalt in nanostructured bainitic steels. *AIP Conf. Proc.* **2018**, 20001, doi:10.1063/1.5041096.

37. Tian, J.; Xu, G.; Zhou, M.; Hu, H.; Xue, Z. Effects of Al addition on bainite transformation and properties of high-strength carbide-free bainitic steels. *J. Iron Steel Res. Int.* **2019**, *17*, 49, doi:10.1007/s42243-019-00253-7.
38. Jacques, P.J.; Girault, E.; Mertens, A.; Verlinden, B.; van Humbeeck, J.; Delannay, F. The Developments of Cold-rolled TRIP-assisted Multiphase Steels. Al-alloyed TRIP-assisted Multiphase Steels. *ISIJ Int.* **2001**, *41*, 1068–1074, doi:10.2355/isijinternational.41.1068.
39. Yang, H.-S.; Bhadeshia, H. K. D. H. Designing low carbon, low temperature bainite. *Mater. Sci. Technol.* **2008**, *24*, 335–342, doi:10.1179/174328408X275982.
40. Vuorinen, E.; Heino, V.; Ojala, N.; Haiko, O.; Hedayati, A. Erosive-abrasive wear behavior of carbide-free bainitic and boron steels compared in simulated field conditions. *P. I. Mech. Eng. J-J-Eng.* **2018**, *232*, 3–13, doi:10.1177/1350650117739125.
41. Sk, M.B.; Chakrabarti, D.; Chatterjee, S. Microstructural engineering and strength-impact toughness prediction in ultra-low carbon bainitic steel. *Mater. Sci. Technol.* **2018**, *34*, 1910–1918, doi:10.1080/02670836.2018.1496553.
42. Khare, S.; Lee, K.; Bhadeshia, H. Carbide-Free Bainite: Compromise between Rate of Transformation and Properties. *Metall and Mat Trans A* **2010**, *41*, 922–928, doi:10.1007/s11661-009-0164-z.
43. Avishan, B. Transformation induced plasticity effect under tensile and compression stresses in nanostructured bainite. *Materials Science and Engineering: A* **2018**, *729*, 362–369, doi:10.1016/j.msea.2018.05.085.
44. Foughani, M.; Kolahi, A.; Palizdar, Y. The effect of double steps heat treatment on the microstructure of nanostructure bainitic medium carbon steels. *AIP Conf. Proc.* **2018**, 20024, doi:10.1063/1.5018956.
45. Xinpan, Y.; Huibin, W.; Fanfan, F. Effect of prior martensite on the thermal stability of nanobainitic steels. *Mater. Res. Express* **2019**, *6*, 46512, doi:10.1088/2053-1591/aadec1.
46. Zhao, J.; Zhang, F.; Lv, B.; Yang, Z.; Chen, C.; Long, X.; Zhao, X.; Chu, C. Inconsistent effects of austempering time within transformation stasis on monotonic and cyclic deformation behaviors of an ultrahigh silicon carbide-free nanobainite steel. *Materials Science and Engineering: A* **2019**, *751*, 80–89, doi:10.1016/j.msea.2019.01.100.
47. Yao, Z.; Xu, G.; Hu, H.; Yuan, Q.; Tian, J.; Zhou, M. Effect of Ni and Cr Addition on Transformation and Properties of Low-Carbon Bainitic Steels.

Trans. Indian Inst. Met. **2019**, *72*, 1167–1174, doi:10.1007/s12666-019-01590-7.

48. Kumar, A.; Dutta, A.; Makineni, S.K.; Herbig, M.; Petrov, R.H.; Sietsma, J. In-situ observation of strain partitioning and damage development in continuously cooled carbide-free bainitic steels using micro digital image correlation. *Materials Science and Engineering: A* **2019**, *757*, 107–116, doi:10.1016/j.msea.2019.04.098.
49. Chu, C.; Qin, Y.; Li, X.; Yang, Z.; Zhang, F.; Guo, C.; Long, X.; You, L. Effect of Two-Step Austempering Process on Transformation Kinetics of Nanostructured Bainitic Steel. *Materials (Basel)* **2019**, *12*, doi:10.3390/ma12010166.
50. Guo, H.; Feng, X.; Zhao, A.; Li, Q.; Chai, M. Effects of ausforming temperature on bainite transformation kinetics, microstructures and mechanical properties in ultra-fine bainitic steel. *J. Mater. Res. Technol.* **2020**, *9*, 1593–1605, doi:10.1016/j.jmrt.2019.11.085.
51. Yu, X.; Wu, H.; Gu, Y.; Yuan, R.; Zhang, Y.; Feng, Y. Effect of prior martensite on bainite transformation and microstructure of high-carbon nano-bainitic steel. *Journal of Iron and Steel Research International* **2021**, doi:10.1007/s42243-021-00591-5.
52. Guo, H.; Fan, Y.P.; Feng, X.Y.; Li, Q. Ultrafine bainitic steel produced through ausforming-quenching process. *J. Mater. Res. Technol.* **2020**, *9*, 3659–3663, doi:10.1016/j.jmrt.2020.01.103.
53. Kumar, A.; Singh, A. Deformation mechanisms in nanostructured bainitic steels under torsion. *Materials Science and Engineering: A* **2020**, *770*, 138528, doi:10.1016/j.msea.2019.138528.
54. Liu, W.; Jiang, Y.; Guo, H.; Zhang, Y.; Zhao, A.; Huang, Y. Mechanical properties and wear resistance of ultrafine bainitic steel under low austempering temperature. *Int. J. Miner. Metall. Mater.* **2020**, *27*, 483–493, doi:10.1007/s12613-019-1916-4.
55. Chen, G.; Hu, H.; Xu, G.; Tian, J.; Wan, X.; Wang, X. Optimizing Microstructure and Property by Ausforming in a Medium-carbon Bainitic Steel. *ISIJ Int.* **2020**, *60*, 2007–2014, doi:10.2355/isijinternational.ISIJINT-2020-054.
56. Huang, C.; Zou, M.; Qi, L.; Ojo, O.A.; Wang, Z. Effect of isothermal and pre-transformation temperatures on microstructure and properties of ultrafine bainitic steels. *J. Mater. Res. Technol.* **2021**, *12*, 1080–1090, doi:10.1016/j.jmrt.2021.03.038.

57. Gao, G.; Wang, K.; Su, H.; Gui, X.; Li, Z.; Misra, R.; Bai, B. The potential of mechanical twinning in ultrafine retained austenite to enhance high cycle fatigue property of advanced bainitic steels. *Int. J. Fatigue* **2020**, *139*, 105804, doi:10.1016/j.ijfatigue.2020.105804.
58. Hasan, S.M.; Ghosh, M.; Chakrabarti, D.; Singh, S.B. Development of continuously cooled low-carbon, low-alloy, high strength carbide-free bainitic rail steels. *Materials Science and Engineering: A* **2020**, *771*, 138590, doi:10.1016/j.msea.2019.138590.
59. Mousalou, H.; Yazdani, S.; Parvini Ahmadi, N.; Avishan, B. Nanostructured Carbide-Free Bainite Formation in Low Carbon Steel. *Acta Metall. Sin. (Engl. Lett.)* **2020**, *33*, 1635–1644, doi:10.1007/s40195-020-01091-3.
60. Soliman, M.; Palkowski, H. Ultra-fine Bainite Structure in Hypo-eutectoid Steels. *ISIJ Int.* **2007**, *47*, 1703–1710, doi:10.2355/isijinternational.47.1703.
61. Zou, H.; Hu, H.; Xu, G.; Xiong, Z.; Dai, F. Combined Effects of Deformation and Undercooling on Isothermal Bainitic Transformation in an Fe-C-Mn-Si Alloy. *Metals* **2019**, *9*, 138, doi:10.3390/met9020138.
62. Eres-Castellanos, A.; Morales-Rivas, L.; Latz, A.; Caballero, F.G.; Garcia-Mateo, C. Effect of ausforming on the anisotropy of low temperature bainitic transformation. *Mater. Charact.* **2018**, *145*, 371–380, doi:10.1016/j.matchar.2018.08.062.
63. Toji, Y.; Matsuda, H.; Raabe, D. Effect of Si on the acceleration of bainite transformation by pre-existing martensite. *Acta Mater.* **2016**, *116*, 250–262, doi:10.1016/j.actamat.2016.06.044.
64. Zhou, W.; Hou, T.; Tao, L.; Wu, K. In Situ Observation on the Effects of Prior Martensite Formation on Nanostructured Low–Temperature Bainite Transformation. *Metals* **2018**, *8*, 818, doi:10.3390/met8100818.
65. Heinz Palkowski. *Thermomechanisch hergestellter extrem fester Bainit mit reduziertem C-Gehalt*, 2011.
66. Mousalou, H.; Yazdani, S.; Avishan, B.; Ahmadi, N.P.; Chabok, A.; Pei, Y. Microstructural and mechanical properties of low-carbon ultra-fine bainitic steel produced by multi-step austempering process. *Mater. Sci. Eng., A* **2018**, *734*, 329–337, doi:10.1016/j.msea.2018.08.008.
67. v. Ballarin; Soler, M.; Perlade, A.; Lemoine, X.; Forest, S. Mechanisms and Modeling of Bake-Hardening Steels: Part I. Uniaxial Tension. *Metall and Mat Trans A* **2009**, *40*, 1367–1374, doi:10.1007/s11661-009-9813-5.

68. Baker, L.J.; Parker, J. d.; Daniel, S.R. Mechanism of bake hardening in ultralow carbon steel containing niobium and titanium additions. *Mater. Sci. Technol.* **2002**, *18*, 541–547, doi:10.1179/026708302225001741.
69. Ji, D.; Zhang, M.; Zhu, D.; Luo, S.; Li, L. Influence of microstructure and pre-straining on the bake hardening response for ferrite-martensite dual-phase steels of different grades. *Materials Science and Engineering: A* **2017**, *708*, 129–141, doi:10.1016/j.msea.2017.09.127.
70. Abdalla, A.J.; Hein, L.; Pereira, M.S.; Hashimoto, T.M. Mechanical behaviour of strain aged dual phase steels. *Materials Science and Technology* **1999**, *15*, 1167–1170, doi:10.1179/026708399101505211.
71. Waterschoot, T.; Cooman, B.C. de; De, A.K.; Vandeputte, S. Static strain aging phenomena in cold-rolled dual-phase steels. *Metall and Mat Trans A* **2003**, *34*, 781–791, doi:10.1007/s11661-003-0113-1.
72. Türkmen, M.; Gündüz, S. Bake-Hardening Response of High Martensite Dual-Phase Steel with Different Morphologies and Volume Fractions. *Acta Metall. Sin. (Engl. Lett.)* **2014**, *27*, 279–289, doi:10.1007/s40195-014-0043-5.
73. Ramazani, A.; Bruehl, S.; Abbasi, M.; Bleck, W.; Prahl, U. The Effect of Bake-Hardening Parameters on the Mechanical Properties of Dual-Phase Steels. *steel research int.* **2016**, *87*, 1559–1565, doi:10.1002/srin.201600060.
74. Ramazani, A.; Bruehl, S.; Gerber, T.; Bleck, W.; Prahl, U. Quantification of bake hardening effect in DP600 and TRIP700 steels. *Materials & Design* **2014**, *57*, 479–486, doi:10.1016/j.matdes.2014.01.001.
75. Institut für seltene Erden Elemente und strategische Metalle. Available online: https://ise-metal-quotes.com/ (accessed on 26 September 2021).
76. Metalary. Available online: https://www.metalary.com/ (accessed on 26 September 2022).
77. Heo, Y.-U.; Song, Y.-Y.; Park, S.-J.; Bhadeshia, H. K. D. H.; Suh, D.-W. Influence of Silicon in Low Density Fe-C-Mn-Al Steel. *Metall and Mat Trans A* **2012**, *43*, 1731–1735, doi:10.1007/s11661-012-1149-x.
78. Chen, S.; Rana, R.; Haldar, A.; Ray, R.K. Current state of Fe-Mn-Al-C low density steels. *Prog. Mater Sci.* **2017**, *89*, 345–391, doi:10.1016/j.pmatsci.2017.05.002.
79. Lee, K.; Park, S.-J.; Choi, Y.S.; Kim, S.-J.; Lee, T.-H.; Oh, K.H.; Han, H.N. Dual-scale correlation of mechanical behavior in duplex low-density steel. *Scr. Mater.* **2013**, *69*, 618–621, doi:10.1016/j.scriptamat.2013.07.015.
80. ThermoCalc. Available online: https://thermocalc.com/about-us/methodology/the-calphad-methodology/ (accessed on 12 July 2019).

81. Huang, H.; Sherif, M.Y.; Rivera-Díaz-del-Castillo, P. Combinatorial optimization of carbide-free bainitic nanostructures. *Acta Mater.* **2013**, *61*, 1639–1647, doi:10.1016/j.actamat.2012.11.040.
82. Garcia-Mateo, C.; Paul, G.; Somani, M.; Porter, D.; Bracke, L.; Latz, A.; Garcia De Andres, C.; Caballero, F. Transferring Nanoscale Bainite Concept to Lower C Contents: A Perspective. *Metals* **2017**, *7*, 159, doi:10.3390/met7050159.
83. TA Instruments. Available online: https://www.tainstruments.com/dil-805adt-quenching-dilatomers/ (accessed on 19 July 2019).
84. LVDT. Available online: https://www.te.com/usa-en/industries/sensor-solutions/insights/lvdt-tutorial.html (accessed on 19 July 2019).
85. Goulas, C.; Mecozzi, M.G.; Sietsma, J. Bainite Formation in Medium-Carbon Low-Silicon Spring Steels Accounting for Chemical Segregation. *Metall and Mat Trans A* **2016**, *47*, 3077–3087, doi:10.1007/s11661-016-3418-6.
86. Peet, M.J.; Hasan, H.S.; Avettand-Fènoël, M.-N.; Raubye, S.H.A.; Bhadeshia, H.K.D.H. Low-temperature transformation to bainite in a medium-carbon steel. *Int. J. Mater. Res.* **2017**, *108*, 89–98, doi:10.3139/146.111461.
87. Koo, M.; Xu, P.; Tomota, Y.; Suzuki, H. Bainitic transformation behavior studied by simultaneous neutron diffraction and dilatometric measurement. *Scripta Materialia* **2009**, *61*, 797–800, doi:10.1016/j.scriptamat.2009.06.032.
88. Xu, Y.; Xu, G.; Mao, X.; Zhao, G.; Bao, S. Method to Evaluate the Kinetics of Bainite Transformation in Low-Temperature Nanobainitic Steel Using Thermal Dilatation Curve Analysis. *Metals* **2017**, *7*, 330, doi:10.3390/met7090330.
89. Soliman, M.; Palkowski, H. Influence of hot working parameters on microstructure evolution, tensile behavior and strain aging potential of bainitic pipeline steel. *Materials & Design* **2015**, *88*, 759–773, doi:10.1016/j.matdes.2015.09.040.
90. S Bechet, L.B. New reagent for the micrographical demonstration of the austenite grain of hardened or hardened-tempered steels. *Rev. Met.* **1955**, *52*, 830–836.
91. DESY. Available online: http://photon-science.desy.de/research/students__teaching/primers/synchrotron_radiation/index_eng.html (accessed on 23 July 2019).
92. Cullity, B.D.; Stock, S.R. *Elements of X-Ray diffraction*, 3rd ed.; Prentice Hall: Upper Saddle River, NJ, 2001, ISBN 9780131788183.

93. Mohamed Soliman. Phase Transformation and Mechanical Properties of New Austenite-Stabilised Bainite Steels. Dissertation; Clausthal University of Technology, Clausthal-Zellerfeld, 2007.
94. D.J. Dyson and B. Holmes. Effect of Alloying Additions on the Lattice Parameter of Austenite. *J Iron Steel Inst* **1970**, *208*, 469–474.
95. Garcia-Mateo, C.; Jimenez, J.A.; Yen, H.-W.; Miller, M.K.; Morales-Rivas, L.; Kuntz, M.; Ringer, S.P.; Yang, J.-R.; Caballero, F.G. Low temperature bainitic ferrite: Evidence of carbon super-saturation and tetragonality. *Acta Materialia* **2015**, *91*, 162–173, doi:10.1016/j.actamat.2015.03.018.
96. Soiński, M.S.; Jakubus, A.; Kordas, P.; Skurka, K. The Effect of Aluminium on Graphitization of Cast Iron Treated with Cerium Mixture. *Arch. Foundry Eng.* **2014**, *14*, 95–100, doi:10.2478/afe-2014-0044.
97. Shayesteh-Zeraati, A.; Naser-Zoshki, H.; Kiani-Rashid, A.R.; Yousef-Sani, M.R. The effect of aluminium content on morphology, size, volume fraction, and number of graphite nodules in ductile cast iron. *Proceedings of the IMechE* **2010**, *224*, 117–122, doi:10.1243/14644207JMDA302.
98. Sidjanin, L.; Smallman, R.E.; Young, J.M. Electron microstructure and mechanical properties of silicon and aluminium ductile irons. *Acta Metall. Mater.* **1994**, *42*, 3149–3156, doi:10.1016/0956-7151(94)90412-X.
99. Garcia-Mateo, C.; Jimenez, J.A.; Lopez-Ezquerra, B.; Rementeria, R.; Morales-Rivas, L.; Kuntz, M.; Caballero, F.G. Analyzing the scale of the bainitic ferrite plates by XRD, SEM and TEM. *Materials Characterization* **2016**, *122*, 83–89, doi:10.1016/j.matchar.2016.10.023.
100. Akram, M.; Soliman, M.; Palkowski, H. Nano-Bainitic Steels: Acceleration of Transformation by High Aluminum Addition and Its Effect on Their Mechanical Properties. *Metals* **2021**, *11*, 1210, doi:10.3390/met11081210.
101. Bhadeshia, H. K. D. H.; Edmonds, D.V. Bainite in silicon steels: new composition–property approach Part 2. *Met. Sci.* **1983**, *17*, 420–425, doi:10.1179/030634583790420646.
102. Lee, S.; Lee, S.-J.; Cooman, B.C. de. Austenite stability of ultrafine-grained transformation-induced plasticity steel with Mn partitioning. *Scr. Mater.* **2011**, *65*, 225–228, doi:10.1016/j.scriptamat.2011.04.010.
103. Raghavan, V.; Cohen, M. Measurement and interpretation of isothermal martensitic kinetics. *Metallurgical Transaction* **1971**, *2*, 2409–2418, doi:10.1007/BF02814878.
104. Das Gupta, S.C.; Lement, B.S. Isothermal Formation of Martensite at Subzero. *JOM* **1951**, *3*, 727–731, doi:10.1007/BF03397383.

105. Liu, W.; Zhang, B.; Zhao, A.; Guo, H.; Sun, S. Control of morphology and dimension of blocky retained austenite in medium-carbon steel. *Mater. Res. Express* **2019**, *6*, 16526, doi:10.1088/2053-1591/aae561.
106. Kim, M.T.; Park, T.M.; Baik, K.-H.; Choi, W.S.; Choi, P.-P.; Han, J. Crucial microstructural feature to determine the impact toughness of intercritically annealed medium-Mn steel with triplex-phase microstructure. *Acta Materialia* **2019**, *164*, 122–134, doi:10.1016/j.actamat.2018.10.043.
107. Li, J.; Cheng, L.; Zhang, P.; Wang, L.; Li, H. Effect of delta ferrites on the anisotropy of impact toughness in martensitic heat-resistant steel. *J. Mater. Res. Technol.* **2019**, *8*, 1781–1788, doi:10.1016/j.jmrt.2018.12.008.
108. Kim, M.T.; Park, T.M.; Baik, K.-H.; Choi, W.S.; Choi, P.-P.; Han, J. Crucial microstructural feature to determine the impact toughness of intercritically annealed medium-Mn steel with triplex-phase microstructure. *Acta Materialia* **2019**, *164*, 122–134, doi:10.1016/j.actamat.2018.10.043.
109. Pickering, F.B. *Physical metallurgy and the design of steels*, Repr; Applied Science Publ: London, 1983, ISBN 0853347522.
110. Isasti, N.; Jorge-Badiola, D.; Taheri, M.L.; Uranga, P. Microstructural Features Controlling Mechanical Properties in Nb-Mo Microalloyed Steels. Part II: Impact Toughness. *Metall and Mat Trans A* **2014**, *45*, 4972–4982, doi:10.1007/s11661-014-2451-6.
111. Gutiérrez, I. Effect of microstructure on the impact toughness of Nb-microalloyed steel: Generalisation of existing relations from ferrite–pearlite to high strength microstructures. *Materials Science and Engineering: A* **2013**, *571*, 57–67, doi:10.1016/j.msea.2013.02.006.
112. Sandvik, B.P.J.; Nevalainen, H.P. Structu re-property relationships in commercial low-alloy bainitic-austenitic steel with high strength, ductility, and toughness. *Metals Technology* **1981**, *8*, 213–220, doi:10.1179/030716981803275992.
113. Jirková, H.; Mašek, B.; Wagner, M.F.-X.; Langmajerová, D.; Kučerová, L.; Treml, R.; Kiener, D. Influence of metastable retained austenite on macro and micromechanical properties of steel processed by the Q&P process. *J. Alloys Compd.* **2014**, *615*, S163-S168, doi:10.1016/j.jallcom.2013.12.028.
114. Mintz, B.; Lewis, J.; Jonas, J.J. Importance of deformation induced ferrite and factors which control its formation. *Materials Science and Technology* **1997**, *13*, 379–388, doi:10.1179/mst.1997.13.5.379.
115. Weng, Y. *Ultra-fine grained steels*, [Nachdr. - print on demand]; Metallurgical Industry Press: Beijing, 2010, ISBN 978-3-540-77230-9.

116. De, A.K.; Vandeputte, S.; Soenen, B.; Cooman, B.C. de. Effect of grain size on the static strain aging of a ULC-bake hardening steel. *MEKU* **2004**, *95*, 713–717, doi:10.3139/146.018008.
117. Ormsuptave, N.; Uthaisangsuk, V. Effect of Fine Grained Dual Phase Steel on Bake Hardening Properties. *Steel Res. Int.* **2017**, *88*, 1600150, doi:10.1002/srin.201600150.
118. Soliman, M.; Palkowski, H. Tensile properties and bake hardening response of dual phase steels with varied martensite volume fraction. *Materials Science and Engineering: A* **2020**, *777*, 139044, doi:10.1016/j.msea.2020.139044.
119. Shan, Y.V.; Soliman, M.; Palkowski, H.; Kozeschnik, E. Modeling of Bake Hardening Kinetics and Carbon Redistribution in Dual-Phase Steels. *Steel Res. Int.* **2020**, *93*, 2000307, doi:10.1002/srin.202000307.
120. Svoboda, J.; Zickler, G.A.; Kozeschnik, E.; Fischer, F.D. Kinetics of interstitial segregation in Cottrell atmospheres and grain boundaries. *Philos. Mag. Lett.* **2015**, *95*, 458–465, doi:10.1080/09500839.2015.1087652.
121. K.C. Russell. The theory of void nucleation in metals. *Acta Metall.* **1978**, *26*, 1615–1630.
122. Kozeschnik, E.; Svoboda, J.; Fratzl, P.; Fischer, F.D. Modelling of kinetics in multi-component multi-phase systems with spherical precipitates. *Materials Science and Engineering: A* **2004**, *385*, 157–165, doi:10.1016/j.msea.2004.06.016.
123. Takahashi, M.; Bhadeshia, H. K. D. H. Model for transition from upper to lower bainite. *Materials Science and Technology* **1990**, *6*, 592–603, doi:10.1179/mst.1990.6.7.592.
124. He, S.H.; He, B.B.; Zhu, K.Y.; Huang, M.X. Evolution of dislocation density in bainitic steel: Modeling and experiments. *Acta Materialia* **2018**, *149*, 46–56, doi:10.1016/j.actamat.2018.02.023.
125. Bhadeshia, H. K. D. H.; Edmonds, D.V. The bainite transformation in a silicon steel. *Metall and Mat Trans A* **1979**, *10*, 895–907, doi:10.1007/BF02658309.
126. *Low-Temperature Diffusion of Carbon in Iron Measured by SIMS Technique;* J. ČERMÁK, L.K., Ed. Metal, Roznov pod Radhostem, Czech Republic, 18. - 20.5, 2010.
127. Morales-Rivas, L.; Garcia-Mateo, C.; Sourmail, T.; Kuntz, M.; Rementeria, R.; Caballero, F. Ductility of Nanostructured Bainite. *Metals* **2016**, *6*, 302, doi:10.3390/met6120302.

List of figures

List of tables